

Cellular Morphogenic Processes under Geometric Constraints

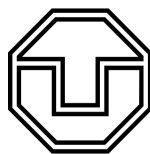
Hydrodynamic Modeling and Simulations, Exploring the Coupling
of Active Mechanics and Geometry in the *C. elegans* Embryo.

by

Michael Nestler

born 11. December 1981
Dresden, Germany

A dissertation presented for the degree of
Doctor rerum naturalium (Dr. rer. nat.)



**TECHNISCHE
UNIVERSITÄT
DRESDEN**

School of Science, Faculty of Mathematics

This dissertation was created from October 2013 through April 2019
at the Institute of Scientific Computing at TU Dresden.

Submitted at: 16. April 2019
Disputation at:

Reviewer 1:

Reviewer 2:

Cellular Morphogenic Processes under Geometric Constraints

Hydrodynamic Modeling and Simulations, Exploring the Coupling of Active Mechanics and Geometry in the *C. elegans* Embryo.

Michael Nestler

Abstract

This dissertation considers physical processes such as active mechanics which are subject to geometric constraints. It investigates the impact of boundary conditions, topological properties of the domain and local curvature on the dynamics, as well as the stability of equilibrium states in the concerned physical system. As *in-vivo* reference system the embryo of the nematode worm *Caenorhabditis elegans* in its single cell state is considered. Here, the focus lies on the morphogenic processes leading to the initial cell division. Analytical model derivations, systematic model studies and validation along experimental data are the central tools in these investigations.

A hydrodynamic description of active matter is used to describe three developmental processes observed in two major entities, the cytoplasm and cortex of the cell. Here the cytoplasm is considered as a highly heterogeneous mixture occupying the bulk of the cell. This mixture is encased by a thin shell of filamentous meshwork-like structure called cortex. The whole system is then encompassed in a plasma membrane and separated from the surroundings by the rigid eggshell. In such a geometric set-up of a volume domain bounded by an effectively surface-like domain, fields of particle numbers, velocities and stresses are considered. These fields prototypically represent scalar, vector and tensorial valued fields and are subject to parabolic PDEs.

For the cytoplasmic bulk a coarse-grained, parameter-free model, describing the developmental feature of cytoplasmic streaming, is derived and verified by comparison to experimental data. An active matter model is formulated on the confined geometry of a thin shell. Focusing on the vector/tensor valued components of such models, the impact of the inherently curved nature of such domains, as well as the topological constraints imposed by the boundary conditions, are systematically investigated. It is observed that these geometric properties of the domain pose strict constraints on the considered physical system, depending on the tensorial degree of the considered field. Furthermore, the domain-related constraints remove symmetry properties of equilibrium states but also enable additional equilibrium states not present in equivalent systems for volume like domains. Finally we consider a process of cellular self organization, emerging through the coupling of dynamics in cortex and cytoplasm. Including the sperm donated male pronucleus, as carrier of the central cell organizing entity called the centrosome, enables to define a mechanical feedback loop supporting the proper positioning of PAR domains and male nucleus right before the onset of cell division. Here the geometry provides an essential cue for steering the feedback loop as well as a decisive effect driving the overall system towards the desired spatial configuration. A parameter study reveals that only models including these geometric effects are capable of reproducing the experimental observation of this remarkable process of self organization.

Therefore, this dissertation combines results of physical modeling, differential geometry, numeric simulations and experimental observations to identify relevant coupling mechanisms. It demonstrates the close interdependence between dynamics of active matter systems at the cellular scale and the geometry of their domain.

CONTENTS

1	Introduction	1
1.1	Life Means Broken Symmetries	1
1.2	Notation	8
2	Cytoplasmic Streaming as Stokes Flow	11
2.1	Cytoplasmic Streaming and Intra Cellular Transport	11
2.1.1	Mechanical Properties of the Cytoplasm	12
2.2	A Coarse Grained Model for Cytoplasmic Streaming	13
2.2.1	Hydrodynamic Variables of Cytoplasmic Streaming	13
2.2.2	Experimental Data Set and Comparison to Model	15
2.2.3	Mechanical Properties of the Model	17
2.3	Thermoviscous Pumping of the Cytoplasm	18
2.3.1	Introduction	18
2.3.2	Continuous Model at Instantaneous and Average Time Scale	20
2.3.3	Comparison Model Prediction to Experiments in <i>C. elegans</i> Embryo	25
2.3.4	Capacities and Limits of Modeling for FLUCS	26
2.4	Transport by Cytoplasmic Streaming in the <i>C. elegans</i> Embryo	26
2.4.1	Mechanical Perturbation Experiments	26
2.4.2	Conclusion	28
3	The Cortex as an Active Polar Gel Confined to a Thin Shell	31
3.1	Introduction	31
3.1.1	Properties of the Cell Cortex	32
3.1.2	Active Polar Gels	33
3.1.3	A Brief Detour to Topology	36
3.1.4	Notions of Differential Geometry	38
3.2	Intrinsic and Extrinsic Contributions on Equilibrium States of Polar Ordering	41
3.2.1	Frank Oseen Model and its Thin Shell Limit	42
3.2.2	Comparison of Intrinsic and Thin Shell Model	43

3.2.3	Curvature of Geometry Influences Stability of Defect Configurations	46
3.2.4	Impact of System Size	48
3.3	Q tensors in Thin Shells	48
3.3.1	The Landau - de Gennes Model in Volume and on Surfaces	48
3.3.2	Generalized Thin Shell Limit	52
3.3.3	Coupling Mechanisms of Geometry and Ordering in the Effective Surface Q Tensor Model	56
3.3.4	Impact of System Size	58
3.4	Active Polar Gels in Thin Shells	59
3.4.1	Conclusion	61
4	Alignment of a Developmental Axis by a Mechanical Feedback Loop	65
4.1	Establishment of a Developmental Axis in the <i>C. elegans</i> Embryo	65
4.1.1	Active Mechanics of Cortical Streaming	68
4.1.2	Mechanical Feedback System Promotes Alignment of Nucleus	70
4.2	Principal Properties of the Alignment Mechanism	72
4.2.1	Coupling Mechanisms in the Feedback Loop	72
4.2.2	A Qualitative Model for the Feedback Loop	76
4.2.3	Systematic Considerations	79
4.3	A Thin Shell Model for Cortical Activity	80
4.3.1	Derivation of an Effective Surface Model	80
4.3.2	Line Tension Induced by Myosin Gradients	85
4.4	Geometric Effects Drive and Control the Mechanical Feedback Loop	89
5	Conclusion	91

CHAPTER 1

INTRODUCTION

1.1 Life Means Broken Symmetries

Only broken symmetries allow a differentiation in function, complexity of interactions and variations in shape. Therefore broken symmetries can be found in every organism and at every scale. Examples in the human body include the up-down alignment of digestive organs, on a tissue scale the wrinkling of the brain, polarized cell bodies and sub cellular structures.

The question of the origin of this plethora of structures and shapes and the mechanisms of their creation are part of the fundamental questions of biology. These questions of morphogenesis inspired many investigations and remarkable results. In the field of biological physics a seminal concept was proposed by Alan Turing in 1953 [78].

The Turing patterns are a set of spatial structures emerging from the interaction of chemical reactions and mechanics. While chemistry itself can form patterns by diffusion and reaction, Turing realized the importance and capabilities of flows, stress and elasticity to contribute in pattern formation. Such mechanical couplings do not only enable spatial inhomogeneities but also provide an approach to describe processes of compartmentalization. For example, a separation of two previously mixed substances by interfacial tension.

Once separated domains enable differential development, e.g. growth, which allows buckling phenomena at the interface, possibly leading to almost arbitrary complex shapes. In such situations it comes as no surprise that the geometry of these shapes, their restriction by boundaries or confinement to thin shells, feed back into the dynamics of the original pattern formation processes.

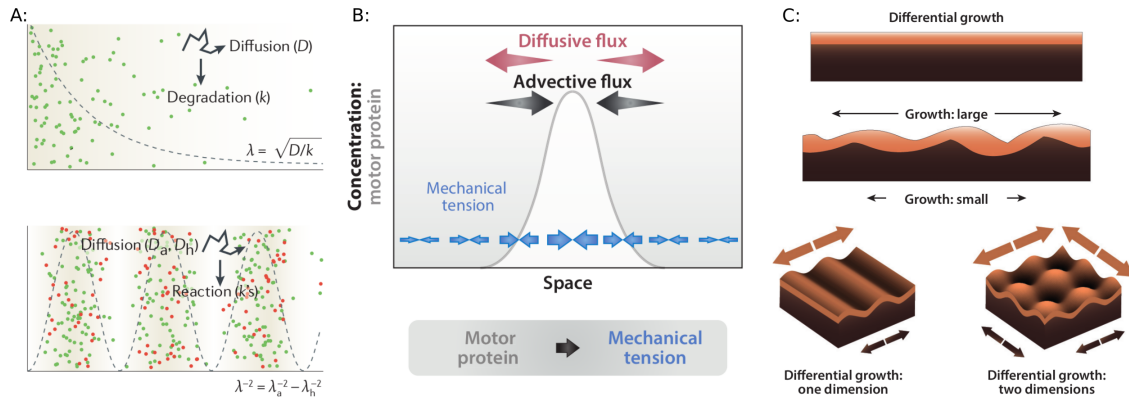


Figure 1.1: **Types of pattern forming mechanisms:** [A]: Pattern forming by diffusion reaction systems. (top) Localized concentration of morphogens (green dots) close to a source. Diffusion of morphogens is limited by degradation. (bottom) "Classic" Turing pattern consisting of inhibitor (red) and activator (green) creating stripe like configurations. [B]: Mechanochemical feedback system driven by gradients in motor proteins creating advective fluxes compensating diffusive fluxes. [C]: Differential growth of tissues enables folded structures, ridge-like and hill like depending on the growth direction. Plots have been adapted from (A)-[30] and (B),(C)-[22].

Given these fundamental considerations, the driving question of this dissertation is:

How do the three concepts of chemistry-mechanics-geometry interact and contribute to the process of morphogenesis?

To discuss this question, we will use a single cell biological reference system, the nematode worm *Caenorhabditis elegans* in its single cell embryo state, see figure 1.2-A. There, at the onset of initial cell division a distinct mechanical feature called cytoplasmic streaming is observed. Such streaming can be traced by long range transport of cellular material which is observed in a wide array of organisms, e. g. plant cells [19]. Recalling the highly delicate nature of a process like cell division where topological change and differential distribution of cell organelles have to be coordinated in a robust way, it is highly unlikely that such a large effect appears at random. Also, the directed nature of these flows suggests a coupling to the polarized cell body axis, possibly providing a stabilizing mechanism supporting the asymmetric distribution of cellular material.

Reviewing the very basic elements at this stage of cell division, we observe the cytoplasm as a highly heterogeneous matrix in which the cell organelles float. This matrix is encased by a thin fluid layer called cortex or cortical layer. Finally the whole cellular system is encompassed in a plasma membrane and separated from the surroundings by a rigid eggshell.

In this situation we observe motor proteins (Myosin) redistributing in the cortex and creating two domains of low and high Myosin concentration. Such gradients in the motor proteins generate stresses on the cellular scale and induce flow in the cortex, see figure 1.2-C,E. Parallel cytoplasmic streaming is observed such that a coupling by drag seems plausible.

At the same time that these flows exist, chemical cue proteins form two domains on the membrane. These so-called PAR polarity proteins come in two families, the aPAR and pPAR proteins.

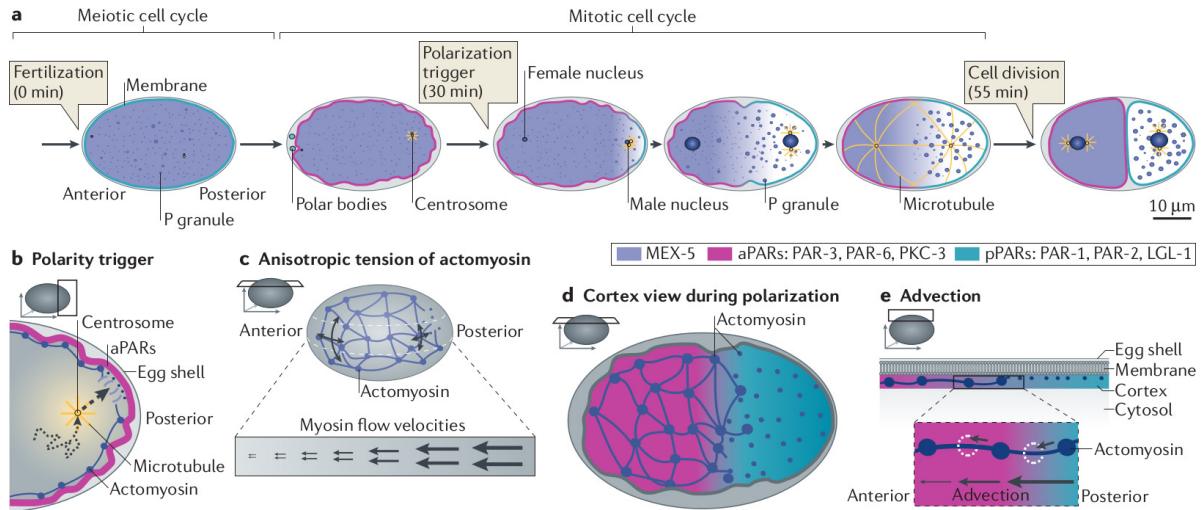


Figure 1.2: **Pattern forming mechanisms in *C. elegans* single cell embryo enabling asymmetric cell division:** [A]: Schematic of temporal stages of asymmetric cell division. After extrusion of polar bodies at anterior pole in Meiotic cell cycle polarization is established in Mitotic cell cycle. Polarization is marked by MEX-5 gradient in cytoplasm and by PAR domain formation in Cortex. [B]: Depletion of aPAR and Myosin in cortical layer is triggered by signals of centrosom. [C]: Cortex is active meshwork of Actin filaments and Myosin motors. Anisotropies in active stress generation, induced by local Myosin depletion from Cortex, induces Myosin flow in cortcial layer. [D]: Snapshot of Actin-Myosin meshwork and PAR distribution in the process of polarization. Depletion of Myosin induces flows of meshwork towards anterior flow. Depletion of aPARs at posterior pole enables binding of pPAR at posterior Pole region. [E]: Cross section of cell cortex demonstrating how flow of Myosin induces passive transport of aPAR towards anterior pole, facilitating the pPAR binding at posterior Pole. Figure taken from [27].

During the phase of cortical flows, they redistribute due to binding kinetics and advective transport via these cortical flows. Before the polarity pattern forms, the aPAR proteins are homogeneously distributed in the cortex, while the pPAR proteins reside in the cytoplasm. In the process of domain formation pPAR accumulates at the posterior pole and thereby enforces a redistribution of aPAR concentrating at the anterior pole. The emerging cortical domains, specified by mutually exclusive concentrations of aPAR and pPAR, mark the separation line in the upcoming cell division.

In this highly selective and simplified description of the process of polarity domain formation we recognize the three major ingredients. First, the chemical dynamics in the cortex, creating mechanical stresses. Second, the induced flow phenomena in the cortex and cytoplasm. Third, the distinct geometric properties of their domains restricting these flows.

Related work In a typical succession of qualitative description of the overall phenomena via the breakdown of involved effects and quantitative estimations of their impact, to a theoretical modeling with predictive capacities, a huge array of investigation in experiment and theory has been performed and is still necessary.

For example, the findings regarding the overall processes in cell division discussed in [18, 20, 52]

have contributed with experiments to a better understanding of the mechanical properties of the cytoplasm and cortex which are reviewed in [69] and [45]. From the field of soft active matter, the work of [40, 39, 69] provides fundamental concepts for modeling the stress generation in active materials. For a comprehensive review see [33].

Also, with computational approaches [60, 67, 58, 55], the flow phenomena in thin shells of fluid, their coupling to neighboring fluids[3] and impact of the thin shell's curvature[65] have been investigated [42]. For example, [62] used a particle based method to approach the cytoplasmic streaming, and [66] used a continuous model to simulate the transduction of stresses generated by a shear flow in a surrounding fluid via a fluid interface to flows inside a vesicle as described in [28].

The theoretical investigations of the coupling of dynamic systems confined to a curved surface have gained a lot of attention. The phenomena of geometric frustration, labeling situation where a preferred order can not propagate throughout the whole domain due to geometrical constraints, has been observed in many physical systems as reviewed in [10]. Furthermore, recent work proposes an analytical framework [57] to describe the transition of bounded domains with no geometric frustration to thin shells with geometric frustration and strong interplay [54, 57, 59] of curvature and dynamics.

Research questions and approach Given these results we aim in this work for an effective theoretical description on a hydrodynamic scale of the dynamics in cortex and cytoplasm confined to the *C. elegans* embryos geometry.

To do so we want to derive and validate a model capturing the observed flows of cytoplasmic streaming in chapter 2. With this model we will address the question of driving forces and discuss the coupling between cortical and cytoplasmic streaming. Furthermore, we extend the model to provide an effective description of the novel technique of thermo viscous pumping inside living cells [48].

We will transfer a generic model of active matter to the confined geometry of a thin shell and investigate how the curvature interacts with physical dynamics in chapter 3. In this framework we discuss how and why curvature acts differently on the quantities of chemical concentrations, velocities or stresses.

With these two building blocks we turn in chapter 4 to the coupled dynamics of chemical activity in the cortex, streaming in cytoplasm and cortical layer and then assess the impact of geometry in these phenomena.

Throughout our work we apply a top down approach for modeling. We neglect microscopic effects and coarse grain on a spatial and temporal scale where an effective description with continuous variables is applicable. In this sense we define the hydrodynamic scale by the sole occurrence of slow and large fluctuations. Typical variables in this context are concentrations, velocities or stresses distributed in space and evolving in time. For these hydrodynamic variables we use first

principles to derive governing equations and identify phenomenological constants. While those constants might be unknown or hard to determine we will rescale the models to the typical scales of the *C. elegans* embryo and work with characteristic numbers like the Reynolds number or Péclet number given by the ratio of phenomenological constants and typical scales. To verify the proposed model and their computational predictions we will use available *in-vivo* measurements.

Collaborators The experimental data used is provided by the partners Peter Gross, Grill lab at BIOTEC, and Matthäus Mittasch, from Kreysing lab of MPI-CBG. Without the productive discussions on physical modeling and evaluation of predicted dynamics this work is not conceivable. Furthermore, this work benefits from the close collaborations with Ingo Nitschke, Simon Praetorius and Axel Voigt from the IWR at TU Dresden. This cooperation developed the essential analytical and numerical tools to derive and solve models in thin shells.

This wide array of collaborators enables a close integration of theory and experiment, underscoring the value of interdisciplinary approaches to tackle complex problems, such as understanding the processes involved in cell division. Given this wide range of contributors, the author uses the pronoun "we" throughout the text.

Parts of the results and discussion presented here have already been published in peer referred journals. These are

- M. Nestler, I. Nitschke, S. Praetorius, A. Voigt:
Orientalional order on surfaces - the coupling of topology, geometry and dynamics.
2018, Journal of Nonlinear Science
- I. Nitschke, M. Nestler, S. Praetorius, H. Löwen, A. Voigt:
Nematic liquid crystals on curved surfaces - a thin film limit.
2018, Proc. Roy. Soc. London
- M. Mittasch, P. Gross, M. Nestler, A. W. Fritsch, C. Iserman, M. Kar, M. Munder, A. Voigt, S. Alberti, S. W. Grill, M. Kreysing.
Non-invasive perturbations of intracellular flow reveal physical principles of cell organization.
2018, Nature Cell Biology

Thanks The author of this dissertation thanks the many collaborators and partners enabling the results presented here.

First of all I would like to thank all the people involved direct or indirect in this dissertation project. I thank my supervisor Axel Voigt for his constant support and patience, as well as pointing me to the intriguing field of biophysics and establishing contact to inspiring project partners. Furthermore, my scientific collaborators Peter Groß and Matthäus Mittasch, who paved me a path into this field of research. I would like to thank all the people at the institute of scientific computation at the TU-Dresden for a relaxed atmosphere and openness. Particularly, I want to thank Ingo Nitschke - to whom I owe my knowledge on differential geometry, Simon Praetorius and Andreas Naumann for enduring my buggy C++ code and their help in straightening it up, Sebastian Reuther and Rainer Backofen for providing fresh views on cumbersome questions - even on lunch time, Christian Köhler and Werner Koch for putting some physical reason in my arguments. I'm grateful for the support I received from Gudrun Heinisch and Cindy Röhling significantly lighten the burden of administrative regulations and procedures.

And of course, I thank all the friends and family, who accompanied me in the ups and downs of this research journey, endured the occasional grumpiness and passed a beer in the right moment.

Finally, I thank the institutions providing a constant financial support (IWR - TU Dresden), valuable experimental data (Grill lab-BIOTEC and Kreysing lab-MPI-CBG) and powerful computational resources (ZIH-TU Dresden and SCJ-Jülich Forschungszentrum).

Without this support and collaboration this work is not conceivable, thank you.

1.2 Notation

This work combines the scientific approaches of differential geometry and contemporary physics. Each approach comes with a specific style of notation which do collide in some situations. In this section we will provide an overview of the used notation.

Domains In general we will consider two domain types. On the one hand side are volumes as subsets of \mathbb{R}^n which are denoted by capital uppercase letters e. g. V . Their boundary is denoted by ∂V with a outward pointing normal $\boldsymbol{\nu}$. On the other hand side we consider manifolds or surfaces embedded in \mathbb{R}^n . These a will be denoted by calligraphic capital letters like \mathcal{M} , where \mathcal{S} is reserved for denoting surfaces. Their normals are denoted by $\boldsymbol{\nu}$ as well and \boldsymbol{n} is used for the conormal in case of bounded manifolds where $\partial\mathcal{M} \neq \emptyset$. In this context a surface can be considered as boundary of a bounded connected volume $\mathcal{S} = \partial V$ with matching normals. Further we will use a hybrid of these two domain types called thin shells. They can be considered as volume like, tubular extension of e. g. a surface with thickness h . We denote them by \mathcal{S}_h with $\mathcal{S}_h \subset V$ and $\lim_{h \rightarrow 0} \mathcal{S}_h = \mathcal{S}$.

Hydrodynamic variables In the context of denoting hydrodynamic variables of physical quantities we apply a notion reflecting on the tensorial degree of the variable. Scalar valued variables are denoted by lowercase Latin letters like concentrations c or reaction rates r . For vector valued qualities like velocities \mathbf{V} we use bold capital Latin letters. Finally variables with tensorial degree two and higher are denoted by bold Greek letters, e. g. the $\boldsymbol{\sigma}$ for the stress tensor. An exception is the nematic order Q-tensor which is denoted, as prevalent in the literature, by \mathbf{Q} . From the school of physic we also adopt the notation of differential quantities like $\Delta\mu$, the chemical potential, or ΔT denoting a difference in temperature.

In the case of variables defined on manifolds or surfaces we define specific names for the tangential parts of the variables, a precise definition is given in section 3.1.4. In the case of vector valued variables we use lower case bold letters, e. g. \mathbf{v} for tangential part of \mathbf{V} on \mathcal{S} . Tangential parts of tensor valued variables are denoted by a subscript, e. g. $\boldsymbol{\sigma}_{\mathcal{S}}$ for the stress acting tangential directions of \mathcal{S} . For \mathbf{Q} the tangential part is denoted by \mathbf{q} .

Furthermore, we will occasionally approximate hydrodynamic variables by a mode decomposition e. g.

$$V(\mathbf{x}, t) \approx \sum_i k_i(t) \mathbb{Z}_i(\mathbf{x}) \quad (1.1)$$

where bold blackboard letters $\mathbb{F}, \mathbb{X}, \dots$ denote temporal invariant specific spatial shapes or profiles. We use small Latin letters to denote the mode coefficient functions.

Basis and coordinates In the course of our argumentation we will make use of operator and coordinate wise description of differential operators or tensor contractions. Here we will rely on the Einstein sum convention and distinguish between contra and covariant formulations as used in standard text books [1, 34]. Further to distinguish between description along a local basis and the

basis of the embedding space for manifold bound tensors we introduce two set of indices.

We will use capital letters like I, J, K, \dots as indices for coordinates w.r.t. to a flat, e.g. Euclidean, basis of the embedding space. For the description along the local basis of the manifold we will use lower case letters i, j, k, \dots . To complement this local basis we denote the normal components by ξ . With \mathbf{e} reserved for basis vectors we can write the coordinates of a vector, on a two dimensional manifold, in the Darboux frame $[\mathbf{e}_i, \mathbf{e}_j, \boldsymbol{\nu}]$ by $[V_i, V_j, V_\xi]$.

Parameters, constants and units Due to the combination of chemical and mechanical balance laws as well as models of orientational order we are confronted with quiet an array of phenomenological constants and parameters. Here we try to use the classical physical notation of lower case Greek letters for phenomenological constants like η viscosity or ρ density. In the context of orientational order of Landau-de Gennes and Frank-Oseen model we will stick with the usual notation of capital letters like K, L denoting prefactors in the free energy contributions. Finally we reserve ω as special symbol for denoting scaling factors of penalty terms.

The derived models are in general unit free. For considerations of scaling behavior or denoting experimental parameters we will use units if necessary. $\mathcal{O}()$ denotes the Landau symbol for describing behavior on orders of magnitude. Since we we are concerned with systems of cellular size we suggest to review the presented models under a length scale of $[\mu\text{m}]$ an $[\text{s}]$ as temporal scale.

Derivatives In the subsequent derivations we will use several notions of derivatives. While these all share the fundamental concept of a local linear approximation for the function, the notation includes some subtleties.

For covariant spatial derivatives we will use ∇ for functions or fields regardless their tensorial degree. To highlight the restricted nature of surfaces, compared to the embedding volume, we denote the spatial derivatives in this case by ∇_S . As laid out in section 3.1.4 we can express the covariant derivatives along the partial derivatives $\partial/\partial\mathbf{x}_i$ w.r.t. coordinates i . This concept of partial derivatives can also be applied to the temporal domain where $\partial/\partial t$ is abbreviated by ∂_t .

In the context of energy functionals $\mathcal{F}(\mathbf{P})$ we use the notation of a variation by $\delta\mathcal{F}(\mathbf{P})$ w.r.t. state variable \mathbf{P} . Furthermore, we also use the partial derivatives of associated energy density $\partial f/\partial\mathbf{P}$ in the sense of a linear functional canonically defined by the L^2 scalar product of the state space. Temporal derivatives of a functional, including explicit and implicit dependencies, are called total derivatives and are denoted by $d\mathcal{F}/dt$

Finally, we use two specific notions for second order differential operators of Laplacian type. These are Δ^{dR} . and Δ^{dG} . denoting the deRham and Bochner Laplacians. This symbols should not be confused with Δ used in the variable names of e.g. chemical potential $\Delta\mu$.

CHAPTER 2

CYTOPLASMIC STREAMING AS STOKES FLOW

2.1 Cytoplasmic Streaming and Intra Cellular Transport

In the framework of pattern formation, as described by Turing, transport is a key contribution. Such effects can be classified by two mayor driving mechanisms. On the one hand side, we consider diffusion as a transport phenomena originating from undirected motion of particles. Such movement are observed as effect induced by thermal gradients, so called Brownian motion. In the context of active matter another origin of undirected motion is present.

Consider a gel consisting non-isotropic shaped (e. g. rod like) filaments and motor proteins moving along these filaments. Here, a typical combination of filaments and motors is a Actin-Myosin suspension where Myosin uses hydrolysis of Adenosine triphosphate (ATP) to crawl along the Actin filaments [29, 32]. If the motor proteins then randomly switch between the filaments [6] and the filament network exhibit no specific direction, an undirected movement occurs, leading to an effect labeled, active diffusion.

On the other hand, transport induced by a directed motion is called advection. Here the typical phenomena can observed by the bulk flows of the solvent and the induced transport of the solute substance (e. g. ink drops in water). Again in active matter, the presence of motors can induce directed motion, e. g. the long range transport induced by Kinesin moving along macro molecules [74].

To characterize a systems prevalent mode of transportation the dimensionless Péclet number is defined

$$\text{Pe} = \frac{|\mathbf{V}|l}{D} \quad (2.1)$$

where $|\mathbf{V}|$ denotes the characteristic magnitude of flow velocity, l the typical length scale in the

domain (or observed patterns) and D the diffusivity of the substance. In the case of $Pe \gg 1$ advection dominates, while $Pe \ll 1$ indicates prevalent diffusive transport.

In the case of cytoplasmic streaming in the *C.elegans* embryo, we observe diffusivity, depending on the considered molecule, $D \approx 1.5-5 [\mu\text{m}^2/\text{s}]$ [64, 43], flows at typical velocity of $|\mathbf{V}| = 0.1 [\mu\text{m}/\text{s}]$ at a range of $l = 25 [\mu\text{m}]$. This implies a indefinite Péclet number $Pe \approx 1$ such that transport phenomenas can not be characterized ad hoc. For comparison, the transport in plants at cellular level occurs at $Pe \approx 50$ [19] and we observe advection to clearly outpace diffusion.

Furthermore, the cytoplasm exhibits a complex mechanical behavior, see section 2.1.1, such that the characterization along diffusion and advection might not be sufficient.

In the overall context of establishment of cell polarity along the formation of cortical domains by PAR proteins we want to discuss in this chapter following question:

Do flows observed in cytoplasmic streaming induce relevant transport processes?

To address this questions we will proceed in two steps. As initial step we want to derive a basic mechanical description of the flow phenomena of cytoplasmic streaming. More precisely we establish an effective hydrodynamic description by a Newtonian fluid governed by viscous stresses and drag. We follow the notion that cytoplasmic flows are driven by activity at the Acto-Myosin cortex [11, 46, 61] and discuss whether active contributions in the cytoplasm can be neglected. Furthermore, we will highlight the essential impact of system dimensionality.

In the second step, we turn to the experimental method of *Focused-light-induced cytoplasmic streaming* (FLUCS). This method bases on the effect of thermo-viscous pumping described by Weinert and Braun [80, 81] and is an all optical, contact free method for in-vivo perturbations in the cytoplasmic streaming [48]. It has proven as a novel method enabling perturbation experiments to probe the role of advective transport in in-vivo organisms. Here we will derive and discuss an analytical description of the flows observed in experiments. We extend the previous model of cytoplasmic streaming to include the effects of thermoviscous pumping and to discuss general properties of the FLUCS method.

The chapter is therefore structured as follows, in section 2.2 we derive and validate an effective mechanical model for cytoplasmic streaming. Section 2.3 discusses the FLUCS method under analytical aspects such that we can review in section 2.4 the experimental findings of [48] in the context of advective transport by cytoplasmic streaming. We conclude the Chapter by reviewing the derived model and discussing its scope of validity.

2.1.1 Mechanical Properties of the Cytoplasm

Here we use the notion of cytoplasm to summarize the main bulk of cell material including cytoskeleton structures or granules. This bulk is enclosed by the cortical layer and restricted to a prescribed shape by cell membrane and eggshell.

Furthermore, the cytoplasm consists of many different kind molecules each with its own size and elastic behavior. Such that it comes to no surprise that the mechanical properties of the cytoplasm strongly vary on spatial and temporal scales. For example, while the cytoplasm can be considered in general as a viscoelastic fluid, [45] highlights two scale dependent features. The first feature refers to meshwork structures like the cytoskeleton in the cytoplasm, leading to a dependence on probe size of rheology experiments, e. g. [24], as well as to the frequency of the applied forcing [2]. On the other hand side, the mechanical properties depend on the region of the cell, such that the cytoplasm in the cell periphery is usually more flexible than in the region close to the nucleus [44].

Another strain of research identifies such spatial and temporal scale dependency as a signature of active non-equilibrium processes, see e. g. [49]. The constant consumption of energy, for example in the form of ATP, leads to thermal background noise as well as active noise generated by the molecular motors in the cytoplasm.

Finally we remark that cytoplasm has been observed to undergo solid-gel phase transitions in several organisms [76, 63, 4]. Clearly, such phase transition would imply a fundamental change in material parameters observable at hydrodynamic scale. But, since such behavior has not been investigated in the *C. elegans* embryo we will stick with the most basic assumption and consider hydrodynamic material parameters of the cytoplasm as constant.

2.2 A Coarse Grained Model for Cytoplasmic Streaming

In this section we derive a mechanical model reproducing the cytoplasmic flow fields on hydrodynamic scale. We review a particle based method, described in [62], its modeling assumptions and used phenomenological parameters. Subsequent we derive an analogous model along hydrodynamic variables. Focusing on the velocity fields we arrive at a parameter free, Stokes model for the cytoplasmic streaming.

We validate the proposed model by comparison to *in-vivo* observed velocity fields. To conclude this section we review the model and summarize its key features w.r.t. the made assumptions regarding the mechanical properties of the cytoplasm.

2.2.1 Hydrodynamic Variables of Cytoplasmic Streaming

As we have discussed in section 2.1.1 the cytoplasm is a highly heterogeneous material exhibiting complex behavior in *in-vivo* experiments. We now aim for an effective model on a coarse grained scale focusing on a minimal set of state variables while retaining the essential features observed in the experiments.

In [62, 36] a particle based description of the cytoplasmic streaming has been proposed. [62] approximated cytoplasmic streaming by a set of ≈ 40.000 spherical particles and their dynamics along a discrete momentum balance and particle number conservation. This setting matches the general assumptions of the Navier Stokes equations, which are the starting point of our proposed

coarse grained modeling. Furthermore, [62] suggests a set of phenomenological parameters of dynamical viscosity $\eta = 1 \text{ [Ns/m}^2\text{]}$ [13], water like mass density $\rho = 1 \cdot 10^3 \text{ [kg/m}^3\text{]}$, $l = 60 \text{ [\mu m]}$ and a relative compression rate $\alpha = 10^{-7}$.

For the description in hydrodynamic variables we perform a spatial and temporal coarse graining. The temporal coarse graining across tens of seconds allows us to neglect the elastic effects in the cytoplasm [69]. On spatial scale we assume the cytoplasm as a continuous Newtonian fluid with constant viscosity, describing the ratio of shear to deviatoric stress in the fluid. In this framework the relevant hydrodynamic variables are velocity \mathbf{V} , as displacement and deformation of a volume element per time, external force density \mathbf{F} and pressure P , as an isotropic force resisting volume change.

Reviewing the phenomenological parameters suggested by [62] we assume the fluid as incompressible and use the Reynoldsnumber Re to characterize the ratio of drag to viscous forces.

$$\text{Re} = \frac{\rho |\mathbf{V}| l}{\eta} \quad (2.2)$$

Within the phenomenological parameter suggested by [62], we obtain $\text{Re} \approx 10^{-9}$ and therefore a clear dominance of viscous forces, such that inertia effects can be neglected. By rescaling the well known Stokes system.

$$-\eta \nabla \cdot (\nabla \mathbf{V} + \nabla \mathbf{V}^T) + \nabla P = \mathbf{F} \quad \text{on } V \quad (2.3)$$

$$\nabla \cdot \mathbf{V} = 0 \quad \text{on } V \quad (2.4)$$

The domain V of the cytoplasmic streaming is bounded by the cellular membrane and the rigid eggshell. Furthermore, the cortical mesh work close to the cell membrane with a average thickness of $50 - 100 \text{ [nm]}$ is not explicitly included in this model. A discussion of possible models of this highly active thin shell is presented in chapter 3.

Due to the bounded nature of V we are required to specify boundary conditions. Typical boundary conditions are $\boldsymbol{\sigma} \cdot \boldsymbol{\nu} = \mathbf{F}_{BC}$, prescribing a specific boundary force in normal direction, and $\mathbf{V} = \mathbf{V}_{BC}$, which prescribes a specific velocity. While the first one ensures general solvability of (2.3), in general, it permits flows across the boundary. The second one leaves the pressure undefined up to a constant such that we have to fix the pressure at a singular point to obtain well posed problem. Further, by Gauss's theorem, the prescribed velocity has to satisfy $\int_{\partial V} \mathbf{V}_{BC} \cdot \boldsymbol{\nu} \text{ d}V = 0$ to ensure compatibility with incompressible mass conservation.

Effective model On the basis of this continuous modeling and due to the passive nature [62] of the Newtonian fluids we conclude the system to be driven out of ground state $\mathbf{V} \equiv 0$ solely by external forces in the volume by \mathbf{F} or at the boundary. As mechanistic volume forces gravitation is usually considered, but at height differences of 30 [\mu m] , typical at cellular scales, its impact can be neglected. Therefore the boundary conditions are identified as driving effects and we choose the Dirichlet type, prescribing the velocity \mathbf{V}_{BC} .

Two remarks regarding this modeling decision. On the one hand side, such modeling implies a force at the boundary sufficiently strong to enforce the prescribed velocity regardless of the dynamics inside the domain, a typical example of an one way coupling. Furthermore velocities can be observed consistently, quit contrary to forces, at high spatial and temporal resolution. In the set up of absent external forcing we can factor the viscosity into the pressure and yield a parameter free model for cytoplasmic velocities.

In [62] the cell shape and its evolution have been approximated by a cylinder combined with semispheres at the long axis. Here we will incorporate the observable irregular shapes of the cell. The evolution in the cell shape can be decomposed into tangential and normal deformations, where the tangential contributions are contained in the observed \mathbf{V}_{BC} . The normal contributions can be estimated by the fluctuations of magnitude $\approx 1 [\mu\text{m}]$ at a frequency $\approx 1 [1/\text{min}]$. We therefore neglect those normal contributions to the boundary velocities and include only instantaneous shapes and tangential velocities in our model. This assumption also ensures compatibility with mass conservation.

To ensure a feasible numerical scheme, we incorporate the irregular shapes of V via a diffuse domain approach as described in [41, 15]. The basic idea of this approach is to embed the irregular shapes V into a domain with simple, e.g. box-like, geometry $V \subset V_\phi$ and multiply the state equations (2.3) with a characteristic function of V . To preserve the well posedness of the PDE also in the embedding domain the characteristic function is approximated by a smooth function ϕ , called the phase field function

$$\phi(\mathbf{x}) = \frac{1}{2} \left[1 - \tanh \left(\frac{3d(\mathbf{x})}{\epsilon} \right) \right] \quad (2.5)$$

where $d(\mathbf{x})$ denotes the signed distance of the domain V and ϵ describes the width of the smooth transition. It has been established [15] that for $\epsilon \rightarrow 0$ the solutions (for $\phi > 1/2$) of this approximated problem in V_ϕ converge to solutions of the problem in V . Boundary conditions of Dirichlet type are included in this diffuse domain model by a penalty term, with prefactor β . The diffuse Stokes system reads

$$-\nabla \cdot \left[\tilde{\phi} (\nabla \mathbf{V} + \nabla \mathbf{V}^T) \right] + \nabla(\phi P) = \frac{\beta}{\epsilon^3} (1 - \phi) (\mathbf{V} - \mathbf{V}_{BC}) \quad \text{on } V_\phi \quad (2.6)$$

$$\nabla \cdot (\phi \mathbf{V}) = 0 \quad \text{on } V_\phi \quad (2.7)$$

For numerical stability we have regularized the the equation on V_ϕ/V by using $\tilde{\phi} = \max(\phi, 1e-6)$.

2.2.2 Experimental Data Set and Comparison to Model

To validate the model we use *in-vivo* observations of an individual *C.elegans* embryo. By spinning disc microscopy a 2D slice at the center of cell body is observed. Genetic alteration in the cells enable the tracking of Myosin molecules in the cortical layer. Together with particle image

velocimetry, see e.g. [82, 83], a dataset consisting of velocities in the cytoplasmic bulk \mathbf{V}_V and cortical layer \mathbf{V}_C as well as the cell outline Γ_C across the complete time domain of cytoplasmic streaming is obtained. To limit data noise, measurement errors and to integrate out elastic effects we average the velocities point wise across time frames of 20 [s]. We yield a dataset containing an evolution of 20 snapshots with cytoplasmic velocities on evenly spaced grid with 2000 points, and 250 points along the outline for cortical velocities. The outline itself is discretized as polygon with 250 nodes.

For validation we use the *in-vivo* outlines to define the domain by $\partial V = \Gamma_C$. The observed cortical velocities are assumed as key driver of the cytoplasmic streaming [11, 46, 61] and used therefore as values for the Dirichlet boundary condition $\mathbf{V}_{BC} = \mathbf{V}_C$. We evaluate the cytoplasmic velocities by solving the diffuse domain model (2.6) with a standard FEM method using Taylor-Hood Elements on an adaptively refined mesh. As validation measure we compare the evaluated and observed velocities in the cytoplasm across the set of available data snapshots.

As shown in figure 2.1-A, the proposed Stokes model yields velocity fields very similar to the experimentally observed flows. The *in-vivo* flows fields can be characterized by three major contributions. Two large vortices located at the posterior side, driven by the cortical flows originating at the posterior pole. These vortices form a stream roughly aligned with the anterior posterior axis pointing towards the posterior pole. As third feature we observe low magnitude flows at the anterior pole. Comparing to the modeled flows we observe the first two features to be reproduced qualitatively in the sense that major vortices and jet alignment are reproduced. Remarkably the predicted velocities of the jet differ up to a factor of 2, figure 2.1-C. This mismatch becomes evident in considering the distribution function of the velocity magnitudes of the *in-vivo* data set and model predictions, see figure 2.1-B. Here the modeled flows exhibit a lower fraction in the mid magnitude velocities.

Impact of spatial dimensionality To address this mismatch in the jet velocities we recall the three dimensional nature of the embryo. Assuming a rotational symmetric cell shape as in [62] we observe the driving cortical domain to form a ring around the cytoplasm such that the induced counter flows are focused in the central stream.

To include such rotation extension to the volume we assume an symmetry of flows along the anterior posterior axis. Given this we can reformulate the model in (2.6) to cylinder coordinates $[r, z]$, see e.g. [8], and yield

$$-\left[\frac{1}{r}\partial_r\left(\tilde{\phi}r\partial_r V_r\right) - \frac{1}{r^2}\tilde{\phi}V_r + \partial_z\left(\tilde{\phi}V_r\right)\right] + \partial_r(\phi P) = \frac{\beta}{\epsilon^3}(1-\phi)(V_r - V_{BC,r}) \quad \text{on } V_\phi \quad (2.8)$$

$$-\left[\frac{1}{r}\partial_r\left(\tilde{\phi}r\partial_r V_z\right) + \partial_z\left(\tilde{\phi}V_z\right)\right] + \partial_z(\phi P) = \frac{\beta}{\epsilon^3}(1-\phi)(V_z - V_{BC,z}) \quad \text{on } V_\phi \quad (2.9)$$

$$\frac{1}{r}\partial_r(rV_r) + \partial_z V_z = 0 \quad \text{on } V_\phi \quad (2.10)$$

To obtain compatible axis symmetric *in-vivo* data from the observed slice we use a polar coor-

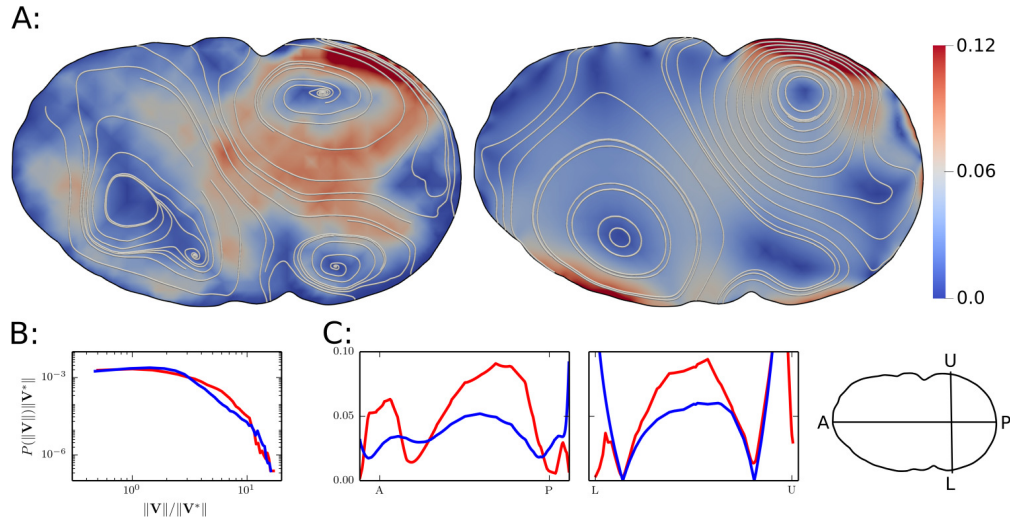


Figure 2.1: **Top down model captures qualitative and quantitative features of cytoplasmic streaming:** [A]: Snapshot of velocity magnitude (color scale) and streamlines of *in-vivo* measurement data (left) and model (right). [B]: Probability distribution for velocity magnitudes for data (red line) and model (blue line) rescaled by most likely velocity of data $\|V^*\| = 0.01$. Distribution function approximated by binning with 35 bins. [C]: Velocity magnitudes along cross section AP (left) and LU (mid) of data and model fields in [A]. AP is defined by anterior-posterior body axis of embryo, LU via centers of major vortices in posterior half, see schematic (right)

dinate description of the data and average the velocities along the polar angle. As shown in figure 2.2 we yield significant better reproduction of the velocity magnitudes in the central stream.

2.2.3 Mechanical Properties of the Model

Reviewing the presented results we conclude that the proposed modeling along hydrodynamic variables suffices to reproduce the qualitative and quantitative features of the observed *in-vivo* cytoplasmic streaming. Most remarkably, by rescaling the pressure with viscosity η , the modeled flow fields are independent of any phenomenological constant, highlighting the fundamental character of the proposed model.

Furthermore, the predictive capacities of Stokes flow model emphasizes the passive nature of the cytoplasm, at viscous time scales, such that conservation of fundamental quantities of mass and linear momentum suffice to describe the dynamics. On the spatial scale we have neglected the heterogeneous nature of the cytoplasm and assumed a Newtonian fluid.

In the proposed model the cytoplasm is one way coupled to the cortex and its dynamics. Furthermore, the model is linear w.r.t. the prescribed boundary velocities and enables a mode decomposition of cytoplasmic flows. Such basic, yet robust, model will provide a useful building block in subsequent modeling.

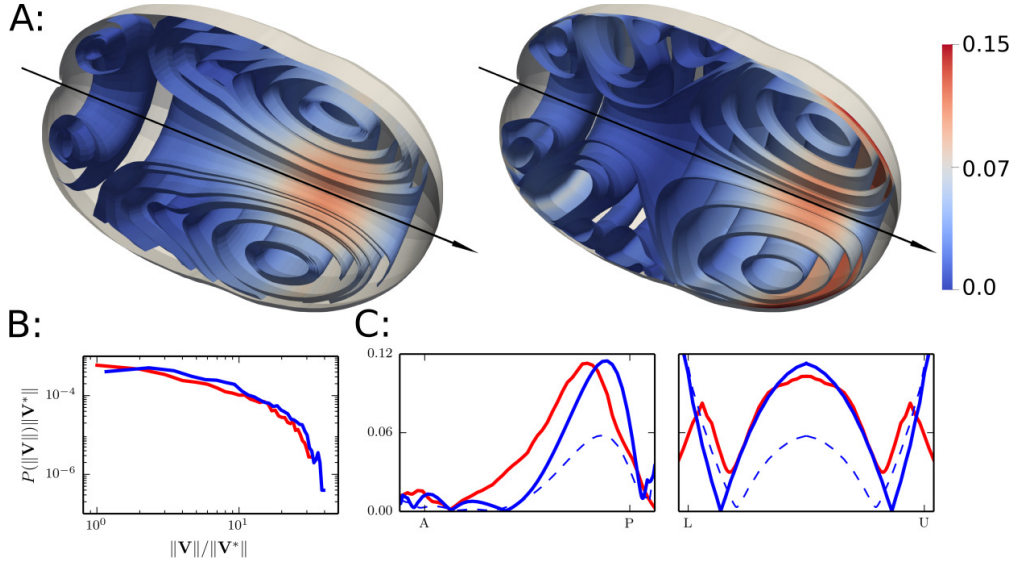


Figure 2.2: **Dimensionality of system play key role in reproducing the peak velocity of central stream:** [A]: Snapshot of velocity magnitude (color scale) and rotational extruded streamlines of *in-vivo* measurement data (left) and model (right). Black arrow indicates rotational axis coinciding with AP. [B]: Probability distribution for velocity magnitudes for data (red line) and model (blue line) rescaled by most likely velocity of data $\|\mathbf{V}^*\| = 0.003$. Distribution function approximated by binning with 35 bins. [C]: Velocity magnitudes along cross section AP (left) and LU (right) of data (red) and model (blue) fields in [A]. Velocities of 2D model are plotted for comparison by blue dashed line. UL axis is defined as perpendicular to AP via center of major vortex in posterior half.

2.3 Thermoviscous Pumping of the Cytoplasm

2.3.1 Introduction

After establishing a fundamental description of cytoplasmic streaming on coarse grained scale we will use it to model the effects of thermoviscous pumping in *in-vivo* *C. elegans* embryos.

The effect of thermoviscous pumping was described by F.M. Weinert and D. Braun in [80, 81] and bases on a highly localized heating of a fluid by a laser oscillating in space. The resulting method allows to induce almost arbitrary flow pattern in thin films of fluids on a contact free and non invasive basis. In [48], we transferred this method to living cellular systems. Through experiments in the *C. elegans* embryo this method has proven as an excellent tool for investigating the coupling of cytoplasm and cortex thereby enabling impressive experimental results.

In this section we will present the associated modeling used in [48] in detail and compare model predictions to experimental results.

Results of F.M. Weinert and D. Braun The core physical mechanism of thermoviscous pumping can be described on the hydrodynamic scale by the response of density and viscosity to local changes in temperature. Considering a localized heating at a fixed position we observe a localized decrease of density and viscosity with symmetric gradients. For a moving heat source

this symmetry is broken and we observe an expansion of the fluid in the front of the heat source and compression in the wake. Furthermore, the locally decreased viscosity breaks the symmetry in the compensating flows and creates a net flow in opposite direction to the heatspot movement, see figure 2.3-A.

To model this effect [80] used the compressible Navier Stokes system of mass and linear momentum balance for a Newtonian fluid. Assuming a sufficient small magnitude of temperature changes the variations in density and viscosity are approximated by a linear response function. This model is applied to a fluid between two plates in an otherwise effectively unbounded domain. Furthermore, assuming an parabolic flow profile between the plates and a Gaussian shaped heatspot, the following estimation of the peak velocity of net flows was established

$$\mathbf{V}_{\text{flow}} = -C\mathbf{U}_S\alpha\beta\Delta T^2 \quad (2.11)$$

Where \mathbf{U}_S denotes the heatspot velocity, α , β are the response rates of density and viscosity to change of temperature ΔT . The constant C depends on the length of the heatspot trajectory L and the heatspot shape. For oscillatory movement of the laser we can also define a frequency $f = \mathbf{U}_S/L$. Using this estimation for pumping in a water like ($\alpha = 3.3 \cdot 10^{-4} [1/\text{K}]$, $\beta = 0.021 [1/\text{K}]$) fluid thin film (thickness $6.5 [\mu\text{m}]$) with $f = 5000 [1/\text{s}]$ and $\Delta T = 9 [\text{K}]$, [80] yielded an theoretical peak velocity of $\mathbf{V} = 100 [\mu\text{m}/\text{s}]$, which is in good agreement with the observed $\mathbf{V} = 95 [\mu\text{m}/\text{s}]$. The associated Navier Stokes equations can also be solved numerically. See figure 2.3-B for qualitative flows, in comoving frame, induced by a traveling heatspot.

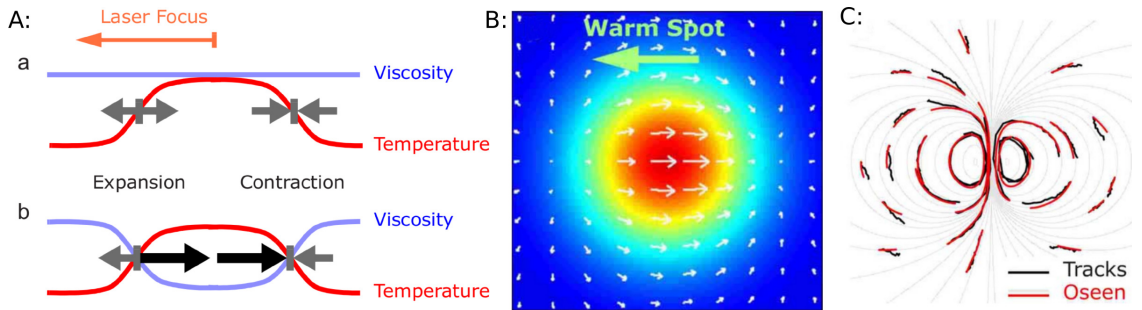


Figure 2.3: **Thermoviscous pumping of homogeneous media in theory and experiment:** [A]: Basic mechanism highlighting the necessity of density and viscosity fluctuations. As shown in [A]-a an absence of viscosity fluctuations does not break symmetry in flow patterns and yields no net flow. [B]: Numerical simulation of qualitative instantaneous flow fields (white arrows, comoving frame) induced by locally increased temperature (color coded). [C]: Flow field inferred from particle tracing (black lines) of pumping with heating laser moving short path and subsequent flyback. For comparison particle trajectories (red lines) resulting from an Stokes flow generated by a superposition of Oseen tensors, continuous streamlines (grey) indicate Stokes flow pattern. Results and figures adapted from [80].

Challenges for application to cytoplasm To transfer the modeling of Weinert and Braun to the pumping of cytoplasm we will focus on three issues.

Our previous modeling has established the Stokes flow model for a homogeneous Newtonian fluid as description of the flows in the cytoplasm on the timescale of tens of seconds. On the other hand side the existing model of thermoviscous pumping bases on the fluctuations in the viscosity and density at an oscillation period of milliseconds.

This raises also the question of the predominate flow type. Here the FEM simulations of [80], see figure 2.3-B, suggest a compressible flow type at the instantaneous timescale (milliseconds) while the observed flow patterns at a timescale of 7[s] exhibit an incompressible flow type (see figure 2.3-C).

Furthermore, we apply thermoviscous pumping to confined geometry where boundaries can no longer be neglected. As known from the solution theory of Navier Stokes equations, compatibility conditions have to be satisfied, possibly limiting the validity of the model. Also close similarities of pumping induced flow patterns to superposition of Stokeslets, see figure 2.3-C, suggests the existence of an overall force. Such force would induce in a bounded domain, like a cell, a compensating force acting on the domain as whole. Therefore one would expect the cell to start moving, which was not observed in the experiments of [48].

Outline of the section This section is split into three parts. In the rather theoretical part we will briefly reproduce the derivations of the governing equations on instantaneous time scale and discuss the source terms driving this system in detail. In a second step we will derive an effective model on the mean timescale (several thousand oscillation cycles). The theoretical part is concluded by discussing the impact of boundaries and suitable modeling. After establishing the theoretical background, in the second part we will validate the proposed model against the *in-vivo* measurements and discuss an experiment presented in [48]. This section is concluded by a brief review of the proposed model, its features and limitations.

2.3.2 Continuous Model at Instantaneous and Average Time Scale

In order to model the described physical effect we follow the approach of [80, 81] and consider the cytoplasm as a compressible isotropic Newtonian fluid with temperature dependent viscosity η and density ρ . The momentum and mass balance in a domain V yields therefore the compressible Navier Stokes equations

$$\rho \frac{\partial \mathbf{V}}{\partial t} + \rho (\mathbf{V} \cdot \nabla) \mathbf{V} - \nabla \cdot (\eta (\nabla \mathbf{V} + \nabla \mathbf{V}^T)) + \nabla P = 0 \text{ in } V \quad (2.12)$$

$$\frac{\partial \rho}{\partial t} + \nabla \cdot (\rho \mathbf{V}) = 0 \text{ in } V \quad (2.13)$$

The temperature dependance of viscosity and density is described, analogous to the Bossinesq assumption, by an linear expansion around their values at ambient temperature T_0 with linear response rates $\alpha = \rho_0^{-1} (\partial \rho / \partial T)$ and $\beta = \eta_0^{-1} (\partial \eta / \partial T)$. Assuming further a sufficient strong thermal diffusivity such that the temperature distribution is not influenced by flows we can express

density and viscosity in relation to an externally prescribed local temperature change ΔT by

$$\rho = \rho_0 (1 - \alpha \Delta T) \quad \text{and} \quad \eta = \eta_0 (1 - \beta \Delta T). \quad (2.14)$$

Following the previous results, we assume predominately viscous effects in the cytoplasmic streaming, leaving the contribution of inertia as neglectable. Inserting the temperature dependent parameters into the compressible Stokes equation we yield

$$-\nabla \cdot ((1 - \beta \Delta T) (\nabla \mathbf{V} + \nabla \mathbf{V}^T)) + \nabla \tilde{P} = 0 \quad \text{in } V \quad (2.15)$$

$$(1 - \alpha \Delta T) \nabla \cdot \mathbf{V} - \alpha \nabla \Delta T \cdot \mathbf{V} = \alpha \frac{\partial \Delta T}{\partial t} \quad \text{in } V \quad (2.16)$$

where the constants ρ_0 and η_0 have been canceled out or factored into the pressure \tilde{P} . As laid out in [80] this model can be adjusted to an effective 2D model for domains V_h with constant small height h by assuming no slip conditions on the upper and lower boundary as well as a parabolic velocity profile in normal direction.

$$-\nabla \cdot ((1 - \beta \Delta T) (\nabla \mathbf{V} + \nabla \mathbf{V}^T)) + 12 \frac{(1 - \beta \Delta T)}{h^2} \mathbf{V} + \nabla \tilde{P} = 0 \quad \text{in } V_h \quad (2.17)$$

$$(1 - \alpha \Delta T) \nabla \cdot \mathbf{V} - \alpha \nabla \Delta T \cdot \mathbf{V} = \alpha \frac{\partial \Delta T}{\partial t} \quad \text{in } V_h \quad (2.18)$$

For the remaining boundaries of V and V_h we prescribe no slip conditions $\mathbf{V} = 0$. To ensure uniqueness of pressure we fix $\tilde{P} = 0$ at a single point e.g. $\mathbf{x} = 0$. For the heatspot we assume an invariant spatial profile $\mathbb{X}(\mathbf{x})$ moving unaccelerated with \mathbf{U}_S . The magnitude of temperature change variates in time $t \in [0, \mathcal{T}]$ and is denoted by $A(t)$ such that

$$\Delta T(\mathbf{x}, t) = A(t) \mathbb{X}(\mathbf{x} - \mathbf{U}_S t). \quad (2.19)$$

Since the heatspot movement is periodic, including a fly back without heating at $t = \mathcal{T}$, we assume $A(0) = A(\mathcal{T}) = 0$.

Flow is driven by monopole and dipole source terms To investigate the discrepancy of flow types present in figure 2.3-B and C we turn to the driving source term $\alpha \frac{\partial \Delta T}{\partial t}$ in the 3D and effective 2D model in (2.15) and (2.17). In the considered case of a non-accelerated movement \mathbf{U}_S , enveloped by a time dependent magnitude we yield two source contributions

$$\frac{\partial \Delta T}{\partial t} = \underbrace{\dot{A}(t) \mathbb{X}(\mathbf{x} - \mathbf{U}_S t)}_{=f_A} - \underbrace{A(t) \mathbf{U}_S \cdot \nabla \mathbb{X}(\mathbf{x} - \mathbf{U}_S t)}_{=f_B} \quad (2.20)$$

Due to linearity of the models, w.r.t. to the source terms, we use the effective 2D model to evaluate the flow fields \mathbf{V}_A and \mathbf{V}_B associated with the sources separately. As shown in figure 2.4 we observe f_b inducing instantaneous flow fields consisting of an area of expansion (in the front of the heatspot) and compression (in the wake of the heatspot). Ignoring the scaling by $A(t)$, this flows can be related to the results of a traveling heat wave in figure 2.3-B. Contrary to this dipole type flow field \mathbf{V}_B the instantaneous flow fields \mathbf{V}_A exhibit a monopole type. Here, depending on

the sign of $\dot{A}(t)$ the velocity points towards or away from the heatspot location where by source (expansion) or sink (compression) defines the flow.

Reviewing now the structure of the source terms, where f_A correlates to $\dot{A}(t)$ and f_B to \mathbf{U}_S we can identify these contributions with the effects of temperature changes induced by on-off switching the heatspot (\mathbf{V}_A) and the movement of the heatspot (\mathbf{V}_B).

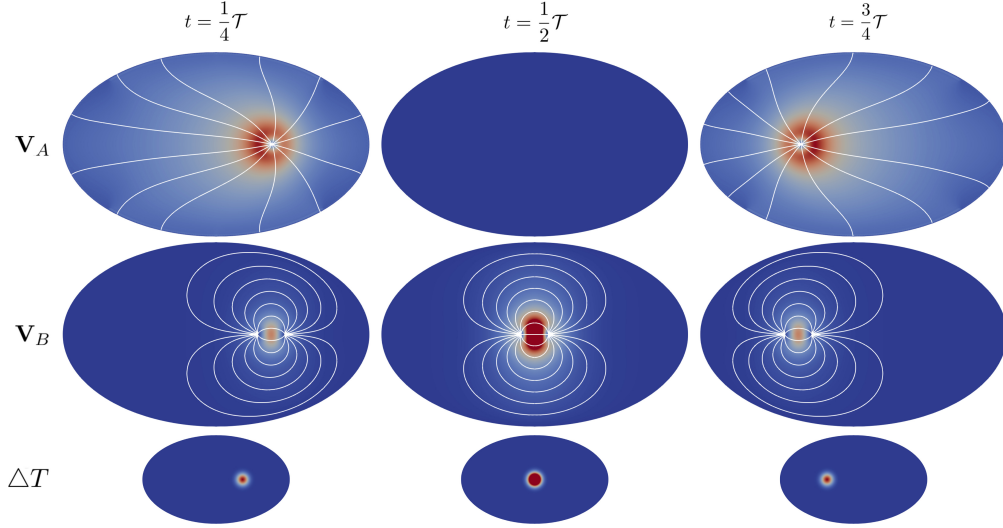


Figure 2.4: **Qualitative instantaneous flow fields induced by source contributions:** numeric simulation of flow fields generated by f_A (top), f_B (mid) and position of heatspot (bottom) at several instants $\in [0, \mathcal{T}]$. Heatspot properties $A(t) = T_{max} \sin^2(\pi/\mathcal{T} t)$ and $\mathbb{X}(\mathbf{x}) = \exp(-\|\mathbf{x} - \mathbf{x}_0\|^2/c^2)$ for water like material parameters $\alpha = 3.3 \cdot 10^{-4}$, $\beta = 0.021$. Other parameters $T_{max} = 8$, $c = 2$, $\mathbf{U}_S = 6 \cdot 10^4$ and $\mathcal{T} = 5 \cdot 10^{-4}$.

The model on temporal average timescale Since in the experiments an effective flow is observed for high frequent repetition of heatspot movement and flyback, we are interested in the effective flow created by a single cycle. To do so we use the linearity of the model, w.r.t. to time, and calculate a mean flow field by

$$\langle \mathbf{V} \rangle = \frac{1}{\mathcal{T}} \int_0^{\mathcal{T}} \mathbf{V} dt. \quad (2.21)$$

As shown in figure 2.5, we yield for both $\langle \mathbf{V}_A \rangle$ and $\langle \mathbf{V}_B \rangle$ a compressible type flow responding to a source-sink combination. Despite these similarities the mean flows have an opposing direction and differ in the modulation of the central part such that a superimposition of $\langle \mathbf{V}_A \rangle$ and $\langle \mathbf{V}_B \rangle$ does yield a nonzero flow field. This netflow can clearly be associated to the thermal response rate of the viscosity β since it vanishes for $\beta = 0$.

Here we point out, that the superposition of $\langle \mathbf{V}_A \rangle$ and $\langle \mathbf{V}_B \rangle$ changes the characteristic of the flow such $\langle \mathbf{V}_A \rangle + \langle \mathbf{V}_B \rangle$ is of incompressible type. To obtain a qualitative understanding of this fundamental change we consider the temporal average of the model (2.15). Using the linearity of

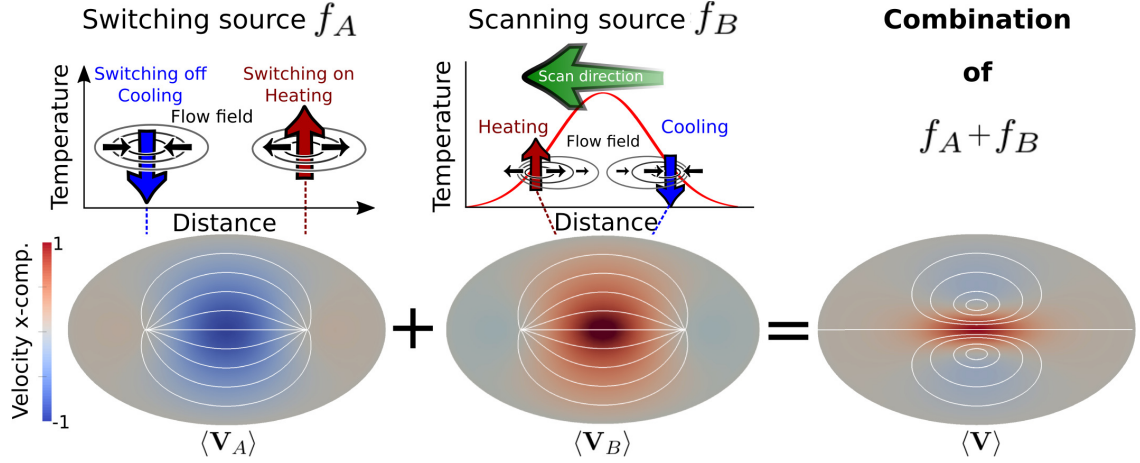


Figure 2.5: **Mean flow fields induced by source contributions:** [left] On-Off switching of heatspot induces compressible type mean flows in direction of laser trajectory. [middle] Movement of heatspot induces compressible type mean flows in opposite direction to heatspot movement as described by [81, 80]. See also figure 2.3-B [right] Superposition of both flows yields incompressible mean flow as observed in experiments, see figures 2.3-C and 2.7. All shown flow magnitudes are qualitative. Figure adapted from [48]

∇ such that

$$\langle \nabla \mathbf{V} \rangle = \nabla \langle \mathbf{V} \rangle \quad (2.22)$$

and fundamental lemma of analysis we yield for any time periodic field quantity f

$$f(0) = f(\mathcal{T}) \Leftrightarrow \left\langle \frac{\partial f}{\partial t} \right\rangle = 0 \quad (2.23)$$

we obtain as temporal averaged model

$$-\langle \nabla \cdot (\nabla \mathbf{V} + \nabla \mathbf{V}^T) \rangle + \beta \langle \nabla \cdot (\Delta T (\nabla \mathbf{V} + \nabla \mathbf{V}^T)) \rangle + \nabla \langle \tilde{P} \rangle = 0 \quad (2.24)$$

$$\nabla \cdot \langle \mathbf{V} \rangle - \alpha \langle \Delta T \nabla \cdot \mathbf{V} \rangle - \alpha \langle \nabla \Delta T \cdot \mathbf{V} \rangle = \alpha \left\langle \frac{\partial \Delta T}{\partial t} \right\rangle. \quad (2.25)$$

Or separating into spatial modulation of the mean flow variables $\langle \mathbf{V} \rangle$ and $\langle \tilde{P} \rangle$, we arrive at a Stokes like system

$$-\nabla \cdot (\nabla \langle \mathbf{V} \rangle + \nabla \langle \mathbf{V} \rangle^T) + \nabla \langle \tilde{P} \rangle = -\beta \nabla \cdot \langle \Delta T (\nabla \mathbf{V} + \nabla \mathbf{V}^T) \rangle \quad (2.26)$$

$$\nabla \cdot \langle \mathbf{V} \rangle = \alpha \left\langle \frac{\partial \Delta T}{\partial t} \right\rangle + \alpha \nabla \cdot \langle \Delta T \mathbf{V} \rangle, \quad (2.27)$$

with three source terms scaling by α or β . We already know that $\alpha \left\langle \frac{\partial \Delta T}{\partial t} \right\rangle = 0$ but we emphasize that this implies $\langle f_A \rangle = -\langle f_B \rangle$ which requires the source-sink configurations of these source terms to cancel on mean flow time scale.

The remaining terms are evaluated numerically for a modified parameter set with water like $\alpha = 3.3 \cdot 10^{-4}$ and to magnify the mean flow effect with $\beta = 0.1$, see figure 2.6. Since both source

terms $\nabla \cdot \langle \Delta T \mathbf{V} \rangle$ and $\nabla \cdot \langle \Delta T (\nabla \mathbf{V} + \nabla \mathbf{V}^T) \rangle$ are of magnitude $\mathcal{O}(1)$, but are rescaled by α and β we conclude that for $\alpha \ll \beta$ the mean flow $\langle \mathbf{V} \rangle$ indeed can be considered as incompressible.

Therefore, the mean flow can be recovered by a superposition of flows generated by force monopoles, as done in figure 2.3-C. In this context we point out that

$$\int_V \nabla \cdot \langle \Delta T (\nabla \mathbf{V} + \nabla \mathbf{V}^T) \rangle dV \approx 0 \quad (2.28)$$

such that the effect of thermoviscous pumping does not exert an overall force on the system.

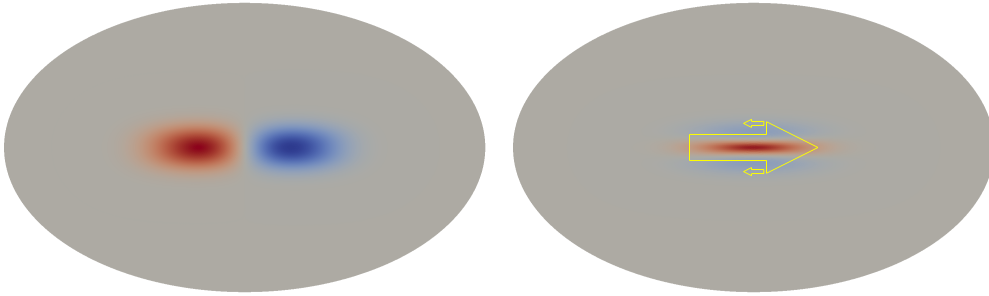


Figure 2.6: **Magnitude and spatial modulation of mean source terms:** Source terms w.r.t. to mean flow model as described in equation (2.26). [left] Distribution of $\nabla \cdot \langle \Delta T \mathbf{V} \rangle \in [-2.4, 2.4]$ indicating a limited compression at end point of heatspot trajectory and expansion at start point. [right] X component of term $-\nabla \cdot \langle \Delta T (\nabla \mathbf{V} + \nabla \mathbf{V}^T) \rangle \in [-5, 16]$, indicating a strong force with opposite direction of heatspot trajectory. While off the heatspot trajectory weak forces in direction of heatspot movement (yellow arrows indicating direction of force scaled by magnitude). Both source contributions even out in the spatial integral such that the mean flow is overall mass conserving and force free.

Boundary conditions restrict admissible heatspot trajectories in the model Before concluding this section we will turn to the boundary conditions. By choosing no slip conditions on ∂V we implicitly required, by Gauss theorem,

$$\int_V \nabla \cdot \mathbf{V} dV = 0 \quad (2.29)$$

which does not coincide with the mass conservation for a compressible flow type and causes ill posed problems for

$$\int_V \Delta T \nabla \cdot \mathbf{V} + \nabla \Delta T \cdot \mathbf{V} + \frac{\partial \Delta T}{\partial t} dV \neq 0. \quad (2.30)$$

An example for such situations is given for heatspot trajectories crossing the boundary ∂V .

2.3.3 Comparison Model Prediction to Experiments in *C. elegans* Embryo

For validation we reproduce an experimental setting of thermoviscous pumping inside the *C. elegans* embryo at the onset of maintenance phase immediately following the cytoplasmic streaming phase, as given in [48]. In figure 2.7 we compare the experimental flow field with the model on average time scale and observe very good agreement. Both data sets exhibit a typical incompressible flow consisting of two vortices shaped by the domain geometry. Remarkably, for choosing water like material parameters ($\alpha = 3.3 \cdot 10^{-4}$ [1/K] and $\beta = 0.021$ [1/K]), the peak velocity is reproduced within 5 percent difference w.r.t. the experimental observations.

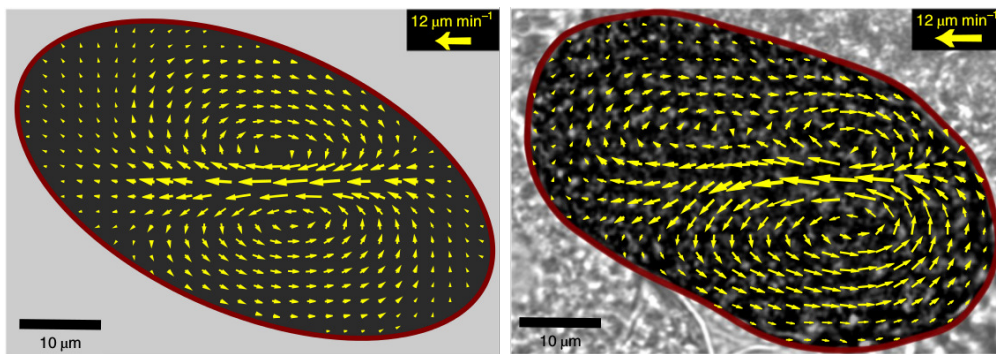


Figure 2.7: **Model predicted flows match FLUCS induced flows:** Snapshot of induced flow fields in embryo on average time scale for thermoviscous pumping a from left to right. [Left] Stokes like flow pattern obtained by 3D model with water like material parameters ($\alpha = 3.3 \cdot 10^{-4}$ [1/K] and $\beta = 0.021$ [1/K]). Cell shape approximated by an ellipsoid with major axis [$25 \mu\text{m}$], [$15 \mu\text{m}$], [$15 \mu\text{m}$]]. [Right] Flow pattern induced by $f = 2$ [kHz] temperature oscillations of $\Delta T = 3$ [K]. Figure adapted from [48].

Furthermore, we use the model to elude the observed effect where thermoviscous pumping induces circular streaming inside the *C. elegans* embryo to transport the PAR distribution, see figure 2.9. The model is used to investigate the principal feature of suppressing a flow vortex by choosing a heatspot trajectory sufficient close to the domain boundary. As shown in figure 2.8, we observe that, by shifting the trajectory towards the boundary, the trapped vortex is compressed and slowed down up to a complete dissolution.

As typical for flows of Stokes type, where momentum influx is immediately compensated by dissipation due to shear stress, we observe a redistribution of shear stress for replaced heatspot trajectories. The stresses previously stored in two vortices are now distributed in a single vortex requiring amplified gradients in the flow field to compensate the unchanged momentum influx. This effect yields an increased velocity close to the heatspot trajectory. The full circular pumping trajectory, as used in experiments shown figure 2.9, can be obtained through a piece-wise superposition of flow field generated by rotated heatspot trajectories.

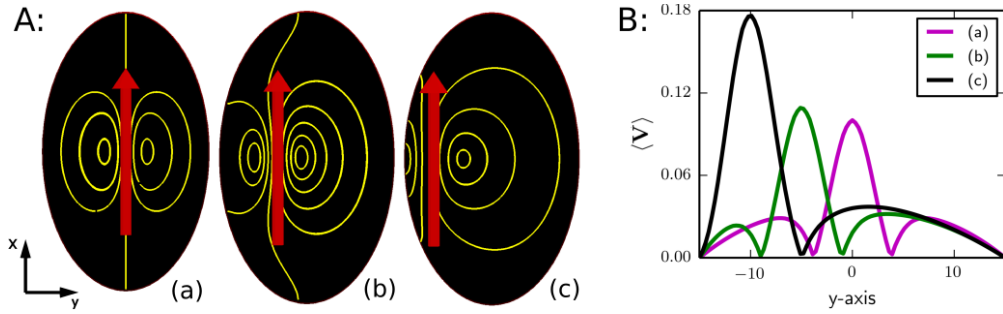


Figure 2.8: **Boundary near scan trajectories induce vortex annihilation and strong flows parallel to cortex:** [A]: Vortex trapped between scan trajectory and cortex is slowed compressed and finally dissolved. Three scan trajectories (red arrow, parameters as in figure 2.7) and induced mean flows (yellow stream lines) in ellipsoid $[27 [\mu\text{m}], 15 [\mu\text{m}], 15 [\mu\text{m}]]$ with distances (a) $5 [\mu\text{m}]$, (b) $10 [\mu\text{m}]$, (c) $15 [\mu\text{m}]$ to cortical layer. [B]: Velocity magnitudes of flows at scan trajectory increase with reduced distance to cortex. Geometric restriction of flows induces up to factor 2 faster peak velocities. Figure adapted from [48].

2.3.4 Capacities and Limits of Modeling for FLUCS

In this section we have extended the model of F.M. Weinert and D. Braun by providing a detailed discussion of source terms and deriving an effective mean flow model. These two extensions enabled us to pin down the origin of the compressible and incompressible flow types in [80]. Furthermore, the mean flow model allowed us to evaluate the effective force field created by a prescribed heatspot trajectory. In this context we could also establish by numerical experiment that flows induced by thermoviscous pumping do not induce an overall force on the system. Considering the bounded nature of a cellular system we highlighted the incompatibility of the proposed model to describe the effect of heatspot trajectories crossing the domain boundaries.

The comparison to experimental measurements on hydrodynamic scale assured that cytoplasmic streaming induced by thermoviscous pumping can be described by the mean flow model and assuming water like parameters. Overall we conclude that the mean flow model is suitable to describe the flows on hydrodynamics scale induced by thermoviscous pumping of *in-vivo* cytoplasm. The experimental method and its analytical modes are versatile and open up a wide array of possible application in mechanical experiments with living cellular organisms [38].

2.4 Transport by Cytoplasmic Streaming in the *C. elegans* Embryo

2.4.1 Mechanical Perturbation Experiments

After establishing a robust notion for cytoplasmic streaming, as Stokes flow on hydrodynamic scales, and deriving an effective description for the effects of thermoviscous pumping in the *C. elegans* embryo, we will review the experimental results presented in [48]. These experiments provide decisive insights how cytoplasmic flows can contribute to the process of PAR domain formation.

In this context, FLUCS is used to induce flow perturbation inside the living embryo. Experiments are performed immediately after the cytoplasmic streaming has ceased at the onset of maintenance phase. This allows fully controlled flows in the cytoplasm. The FLUCS parameters are chosen such that flows are at a similar magnitude, as observed in the previous cytoplasmic streaming phase, and a limited local heating, within the bounds of typical ambient temperature variations.

PAR concentrations are susceptible to advective transport We now discuss a set of experiments concerned with the balance of diffusion to advection in cytoplasm and cortical layer. As shown in figure 2.9-A, B, C, induced flows are capable of altering the local distribution of PAR-2 proteins. Here an induced stagnation flow at the cortical layer increases the concentration up to factor 3. Whether this increase in the cytoplasm does also imply an increase in the cortex remains open but the change of local gradients is highly likely to impact the binding dynamics between those two domains.

Figure 2.9-D, E, F illustrates the second experiment, where induced flows are used to rotate overall PAR-2 distribution in cortex and cytoplasm. Most remarkably the rotation of cortical domain was possible by inducing a rotational cytoplasmic flow. Further, no temporal delay is observed between the application of flows in the cytoplasm and the onset of displacement in the cortex. Also a strong coupling efficiency between the cortical and cytoplasmic velocities ($\mathbf{V}_{cortex} \approx \mathbf{V}/2$) is observed, underlining the strength of the mechanical coupling of these two domains.

Combining these two results we have strong experimental indications that advection, by flows at typical magnitudes, outpaces diffusion for the PAR-2 concentrations. Further we observe the hydrodynamic coupling between cortex and cytoplasm to be double sided, such that flows in one domain will induce flows in the other by interfacial drag.

Large scale transport has qualitative impact on asymmetric cell division Basing on the concept that cortical PAR domains are primary markers for cell division [27, 18, 17] artificial flows were used to dislocate these domains, see [70] for related experiments. As in the previous experiment, rotational flows are excited by FLUCS to induce a rotational displacement of PAR domains. After applying such distortion the response of the living system is monitored, see figure 2.10. In systematic tests it was observed that for rotation less than 90° , PAR domains realign with original anterior-posterior axis figure 2.10-A, while for displacements across $> 90^\circ$ PAR domains align with the inverted anterior-posterior axis, figure 2.10-B. As suspected, the subsequent cell division follows the alignment of the PAR domains and an inverted cell asymmetry is observed for alignment along the inverted anterior-posterior axis, figure 2.10-C.

This striking experiment demonstrates the fundamental bistable character of the alignment of the PAR domains which admits only stable PAR domains centered either at the anterior or posterior pole. How this bistability can emerge and which role the shape of the embryo plays will be discussed in chapter 4. Finally, the observation, that cytoplasmic flows are sufficient to cross the threshold between the stable configurations, underlines their role in the establishment of cell

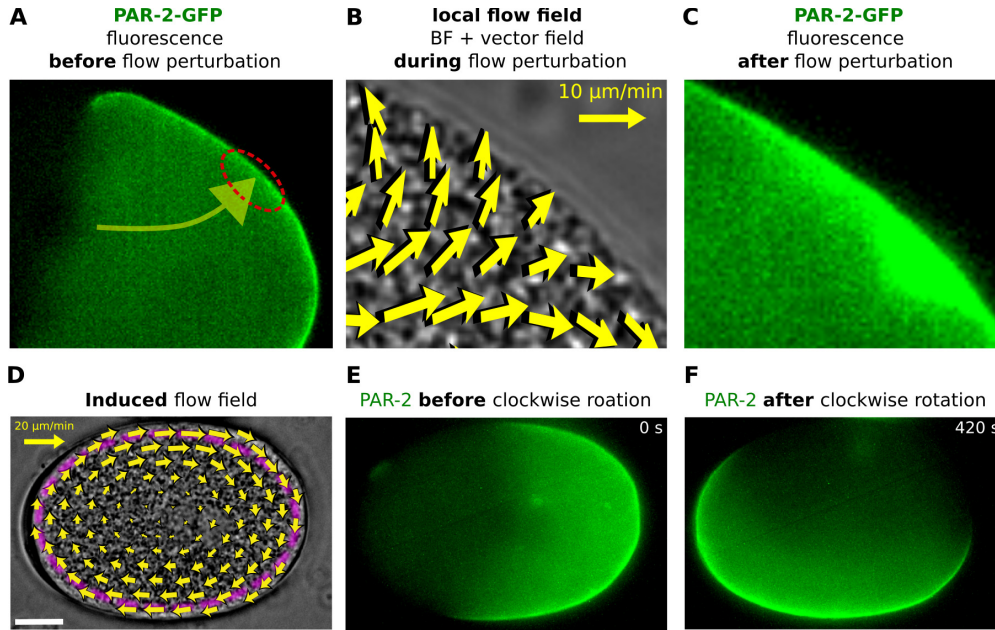


Figure 2.9: **Induced cytoplasmic streaming transport of PAR-2 distribution:** [Top] Induced cytoplasmic streaming facilitating local increase of PAR-2 concentration in cortical region by transport. [A]: Initial distribution of PAR-2 with arrow indicating overall direction of FLUCS induced flows. [B]: Detail of stagnation point for flows close to the cortex. Flow separation at stagnation point induces increased depositing of advected PAR-2. [C]: Up to three times local increase of PAR-2 at stagnation point. [Bottom] Cytoplasmic flows induce large scale transport. [D]: FLUCS induced flow field consisting of strong single vortex encircling complete cytoplasmic domain. Scan path close to the cortex. [E]: Initial distribution of PAR-2. [F]: Consistently transported PAR-2 distribution. Figure adapted from [48].

polarity.

2.4.2 Conclusion

To conclude this chapter we briefly summarize the results. In the context of modeling, we established an effective description for the cytoplasmic streaming, on scale of tens of seconds, along a Stokes flow model for a passive Newtonian fluid. This flow model is linear and parameter free underlining it's basal nature, but also enabling useful analysis techniques like mode decomposition of cytoplasmic flows. Further the modeling of Weiner and Braun for thermoviscous pumping effects could be integrated in this effective model by deriving an effective force field induced by pumping. At this, observable, time scale we could numerically demonstrate the absence of overall forces exerted by thermoviscous pumping. Again by linearity of the flow model we are able to predict and design a wide array of flow patterns induced by FLUCS.

Finally the mechanical perturbation experiments performed with FLUCS highlighted the relevance of transport processes in the process of cortical PAR domain formation, confirmed a double sided mechanical coupling of cortex and cytoplasm as well as revealed the fundamentally bistable character PAR-domain alignment.

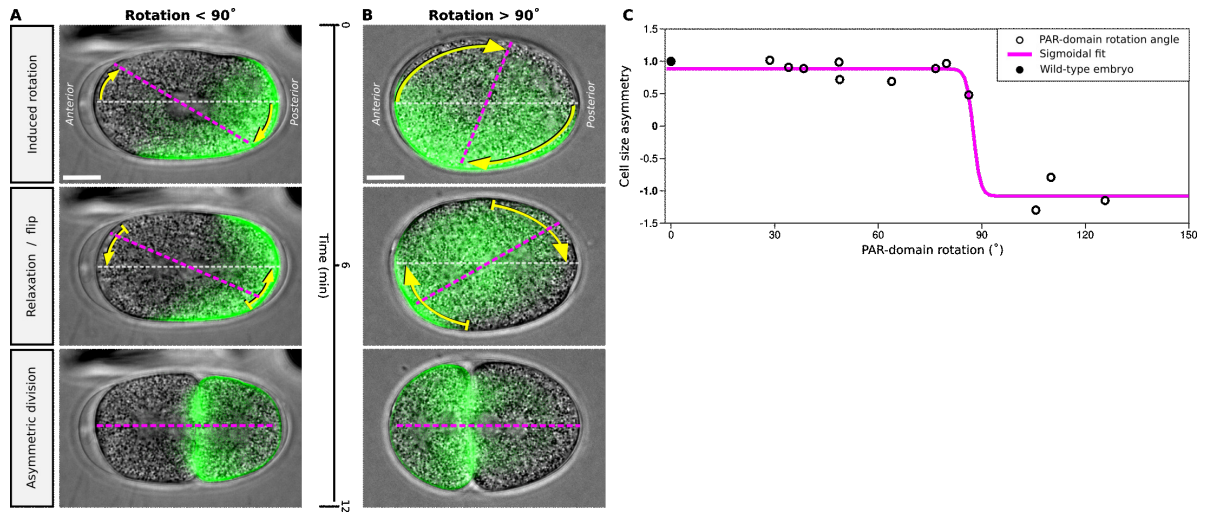


Figure 2.10: **Axis misalignment recovery *in-vivo* and inverted cell division for induced misalignment:**[left] Sequence of instants of cell [right] Induced shift of chemical body axis by rotation A:< 90° and B:> 90°. For case A the chemical axis returns to anterior posterior axis and natural cell division occurs. B: rotation of chemical axis across threshold results in relaxation with inversed chemical axis and inverted cell division. Figure adapted from [48].

We conclude, while the cytoplasm can be considered as a linear, passive system determined by viscous stresses, it contributes to nonlinear effects of morphogenesis by its streaming and mechanical coupling to the cortical layer.

CHAPTER 3

THE CORTEX AS AN ACTIVE POLAR GEL CONFINED TO A THIN SHELL

3.1 Introduction

We will now turn to the cortex of *C. elegans* embryo and discuss the impact of its thin shell like geometry onto the biophysical dynamics there.

These dynamics include the intriguing process of PAR domain formation [27, 18, 17], a typical example of morphogenesis on basis of mechanochemical pattern formation. Also, the material of the cortical layer itself is of high interest, since it is highly heterogeneous consisting of anisotropic constituents (see section 3.1.1). It has been shown that these anisotropies are essential in modeling stress generation by molecular motor [32]. These microscopic effects can give rise to active stresses on hydrodynamic scale. On such coarse grained scale the anisotropies may persist and give the material an effective orientation. This orientation is an essential variable in the models of active polar or nematic gels, which we will discuss in section 3.1.2.

Further we recall the cortex as confined between, on the outer side, the cell membrane-rigid eggshell and, on the inside, by the incompressible cytoplasm, prescribing its thin shell geometry. Such geometry is a highly interesting hybrid of a two dimensional surface and a three dimensional volume. We will take a brief detour into topology, in section 3.1.3, to elude the fundamental effects arising from this specific geometry.

With this background we can address the central question of this chapter:

How do active mechanochemical processes couple to the geometric features of a thin shell geometry?

Here we observe three fundamental principles. The tensorial degree of the considered physical variable determines the possible types of coupling. Further the boundary conditions, in normal direction, off the thin shells boundary specify the coupling, while curvature provides the local strength of these coupling. Overall we will see how thin shell geometries with non constant curvature will induce additional stresses in systems of active polar and nematic fluids. But, to keep the argumentation as plain as possible, we will discuss the coupling mechanisms at example systems of exclusive orientational order. These fundamental systems can be considered as a typical realization of the famous Poincaré-Hopf theorem [47].

In this chapter we discuss the problems of polar order on a surface as an approximate description of a thin shell system. In the case of nematic ordering we refine the approach by using the analytical method of thin shell limit [57, 56], highlighting the importance of boundary conditions in the transition from thin shell to surface. With this framework we can obtain an effective model for active polar fluids in thin shells and discuss possible effects, originating in its specific geometry, on cellular scale.

Complementary, we provide an overview of the notions of differential geometry necessary for the treatment of problems of orientational order on surfaces in section 3.1.4.

3.1.1 Properties of the Cell Cortex

The cellular cortex can be considered as a layer of Actin filaments, Myosin motors and proteins lying next to the plasma membrane [69]. It is a dynamical structure undergoing constant remodeling and turnover, allowing the cell to move, change shape and exert forces. It's microscopic dynamics gives rise to macroscopic properties like viscoelasticity [14] or localized cortical tension [40]. Namely the constant turnover of the cortex constituents enables the cortex to act as a viscous fluid on long timescales (tens of seconds [23]) while on short scales the elastic behavior dominates.

As a coarse grain model for these dynamics the active gel theory has been suggested [40, 69]. There, the cortex is described as a continuous gel subject to internal stresses generated by chemical processes combined with an average alignment of the non-isotropic constituents. Such models have been used to describe cortical flows involved in processes of cell migration [25] or polarization [46] of *C. elegans* in its single cell state.

Reviewing the geometry of the cortex we observe it uniformly covering the complete cell with an very small thickness 50 – 100 [nm] compared to the cell size of of 150 [μm], such that a description as a thin shell seems applicable. Furthermore, in [50] is stated that the Actin filaments are predominantly aligned parallel to the cortex, which will turn out to be a decisive feature for the dynamics in thin shells.

3.1.2 Active Polar Gels

Conservation laws and rate of dissipation We present a generic model analogue to [40], describing the dynamics for a coupled system of motor proteins, chemical energy and polar filaments close to equilibrium in a volume like domain $V \subset \mathbb{R}^3$. Here we use a coarse grained description with continuous fields, valid on a large length scale compared to microscopic volume elements. These fields obey several conservation laws. Mass conservation can be expressed by

$$\partial_t \rho + \nabla \cdot (\rho \mathbf{V}) = 0. \quad (3.1)$$

Here, ρ denotes the mass density, \mathbf{V} the velocity and momentum is defined by $\mathbf{M} = \rho \mathbf{V}$. Further we describe the chemical processes along a set of particle number densities $n_{\mathcal{M}}$, $\mathcal{M} \in \{0, \dots, M\}$, which obey

$$\partial_t n_{\mathcal{M}} + \nabla \cdot (n_{\mathcal{M}} \mathbf{V} + \mathbf{J}_{\mathcal{M}}) = r_{\mathcal{M}} \quad (3.2)$$

where $r_{\mathcal{M}}$ denotes the reaction rates and $\mathbf{J}_{\mathcal{M}}$ relative fluxes. With a mass density of the molecules $m_{\mathcal{M}}$ we have $\rho = \sum_{\mathcal{M}} m_{\mathcal{M}} n_{\mathcal{M}}$. Anyhow, for the sake of simplicity we will restrict our further derivation to a single particle type n and drop the index \mathcal{M} .

Further we express the momentum conservation by a combination of transport and forces exerted by internal stresses $\boldsymbol{\sigma}^{tot}$

$$\partial_t \mathbf{M} + \nabla \cdot (\mathbf{M} \mathbf{V}) - \nabla \cdot \boldsymbol{\sigma}^{tot} = 0 \quad (3.3)$$

For the sake of simplicity we follow [40] and do not discuss conservation of angular momentum, related details can be found at [33].

We define an orientation \mathbf{P} by a local average of microscopic molecule orientation. Following the Frank-Oseen approach [73] we use a free energy to model the director dynamics towards a ground state. Here, we are not concerned with the details of such free energy and summarize possible formulations for directors by $f_0(\mathbf{P}, \nabla \mathbf{P}, n)$. Further f denotes the overall energy density. The free energy of the system is then defined by

$$\mathcal{F}^V(\mathbf{V}, \mathbf{P}, \nabla \mathbf{P}, n) = \int_V \frac{|\mathbf{M}|^2}{2\rho} + f_0(\mathbf{P}, \nabla \mathbf{P}, n) dV = \int_V f dV \quad (3.4)$$

The conjugate fields can then be derived by variation of the free energy and are the molecular field $\mathbf{H} = -\partial f / \partial \mathbf{P}$ and the chemical potentials $\Delta \mu^{tot} = \partial f / \partial n$, $\Delta \mu = \partial f_0 / \partial n$ with

$$\Delta \mu^{tot} = -\frac{1}{2} m \Delta \mu \quad (3.5)$$

Using the material derivative, e.g. for the director field $D\mathbf{P}/Dt = \partial_t \mathbf{P} + (\mathbf{V} \cdot \nabla) \mathbf{P}$, the rate of

dissipation of the overall system is given by the derivative in time and reads then

$$\begin{aligned} \frac{d\mathcal{F}^V}{dt} = & \int_V -(\nabla\mathbf{V}) : \boldsymbol{\sigma}^{tot} + \Delta\mu r + \mathbf{J} \cdot \nabla\Delta\mu - \mathbf{H} \cdot \frac{D\mathbf{P}}{Dt} dV \\ & + \int_{\partial V} \left[\mathbf{V} \cdot \boldsymbol{\sigma}^{tot} \cdot \boldsymbol{\nu} - \boldsymbol{\nu} \cdot \mathbf{V} \left(\frac{|\mathbf{M}|^2}{2\rho} + f_0 \right) - \Delta\mu \boldsymbol{\nu} \cdot \mathbf{J} + \boldsymbol{\nu} \cdot \frac{\partial f_0}{\partial(\nabla\mathbf{P})} \cdot \frac{D\mathbf{P}}{Dt} \right] d\partial V \end{aligned} \quad (3.6)$$

For details of the derivation we refer to [40]. To obtain a description in rotational and translational invariant variables we separate stress and rate of deformation tensors in symmetric and antisymmetric parts

$$\boldsymbol{\sigma}^{tot} = \boldsymbol{\sigma} + \frac{1}{2}(\mathbf{P}\mathbf{H} - \mathbf{H}\mathbf{P}) \quad (3.7)$$

$$\nabla\mathbf{V} = \boldsymbol{\Upsilon} + \boldsymbol{\Omega} \quad (3.8)$$

Where $\boldsymbol{\Upsilon} = 1/2(\nabla\mathbf{V} + \nabla\mathbf{V}^T)$ and $\boldsymbol{\Omega} = 1/2(\nabla\mathbf{V} - \nabla\mathbf{V}^T)$. Assuming a sufficiently extended domain such that we can neglect the boundary contribution, we rewrite the rate of dissipation such that

$$\frac{d\mathcal{F}^V}{dt} = \int_V -\boldsymbol{\Upsilon} : \boldsymbol{\sigma} + \Delta\mu r + \mathbf{J} \cdot \nabla\Delta\mu - \mathbf{H} \cdot \frac{D^c\mathbf{P}}{Dt} dV \quad (3.9)$$

where $D^c\mathbf{P}/Dt = \partial_t\mathbf{P} + (\mathbf{V} \cdot \nabla)\mathbf{P} + \boldsymbol{\Omega} \cdot \mathbf{P}$ denotes the corotational derivative. Finally separating deviatoric $\boldsymbol{\sigma}^d$ and isotropic stresses $P\mathbb{I}_3$ we can identify the flux-force pairs from (3.9)

$$\boldsymbol{\sigma}^d \leftrightarrow \boldsymbol{\Upsilon}, \quad \frac{D^c\mathbf{P}}{Dt} \leftrightarrow \mathbf{H}, \quad r \leftrightarrow \Delta\mu, \quad \mathbf{J} \leftrightarrow \nabla\Delta\mu, \quad (3.10)$$

Onsager relations After establishing this framework, we use the Onsager relations to identify linear reactive and dissipative couplings bewteen fluxes and forces, in situations close to the equilibrium. In the case of hydrodynamic limit, where we consider all elastic stresses as relaxed, we introduce phenomenological coefficients for coupling terms obeying symmetry relations. For the symmetric and trace-free deviatoric stress $\boldsymbol{\sigma}^d = \boldsymbol{\sigma} - P\mathbb{I}_3$, with pressure P and \mathbb{I}_3 the \mathbb{R}^3 identity matrix, we yield

$$\boldsymbol{\sigma}^d = 2\eta\boldsymbol{\Upsilon} + \frac{\nu_1}{2} \left(\mathbf{P}\mathbf{H} + \mathbf{H}\mathbf{P} - \frac{2}{3}(\mathbf{P} \cdot \mathbf{H})\mathbb{I}_3 \right) + \zeta\Delta\mu \left(\mathbf{P}\mathbf{P} - \frac{\mathbf{P} \cdot \mathbf{P}}{3}\mathbb{I}_3 \right), \quad (3.11)$$

with viscosity η and the reactive polarity-flow coupling ν_1 . The coupling by ζ , also reactive, describing the generation of stresses by chemical reaction. For the orientational order the flux-force variable pair we yield

$$\frac{D^c\mathbf{P}}{Dt} = -\nu_1\mathbf{P} \cdot \boldsymbol{\Upsilon} + \frac{1}{\gamma}\mathbf{H} + \lambda_1\mathbf{P}\Delta\mu, \quad (3.12)$$

with additional reactive coupling for deformations-polar ordering, $-\nu_1$, and dissipative coupling to the chemical reaction λ_1 . For the reaction rate we find an expression

$$r = -\zeta \left(\mathbf{P}\mathbf{P} - \frac{\mathbf{P} \cdot \mathbf{P}}{3} \mathbb{I}_3 \right) : \boldsymbol{\Upsilon} + \lambda_1 \mathbf{P} \cdot \mathbf{H} + \Lambda \Delta \mu, \quad (3.13)$$

coupling reaction rate to the alignment of polar fields in a dissipative manner, λ_1 , while the coupling to flow induced deformations is reactive ($-\zeta$). Finally we consider the couplings of relative fluxes as relaxed in the hydrodynamic limit and have a only diffusive D and directed fluxes λ_2

$$\mathbf{J} = -D \nabla \Delta \mu + \lambda_2 \mathbf{P} \Delta \mu. \quad (3.14)$$

Inserting these relations into the conservation laws, allows us to obtain the dynamic equations governing the active polar gels. Using a shorthand definition $\mathbf{Q} = (\mathbf{P}\mathbf{P} - \mathbf{P} \cdot \mathbf{P}/3 \mathbb{I}_3)$, the scalar valued dynamic equations read

$$\frac{D\rho}{Dt} = 0 \quad (3.15)$$

$$\frac{Dn}{Dt} + \nabla \cdot (D \nabla \Delta \mu + \lambda_2 \mathbf{P} \Delta \mu) = -\zeta \mathbf{Q} : \boldsymbol{\Upsilon} + \lambda_1 \mathbf{P} \cdot \mathbf{H} + \Lambda \Delta \mu \quad (3.16)$$

For the director field we have (3.12), while the momentum balance can be rearranged to a Navier-Stokes like form

$$\begin{aligned} \frac{D\mathbf{M}}{Dt} - 2\eta \nabla \cdot \boldsymbol{\Upsilon} + \nabla P &= \frac{1}{2} (\mathbf{P}\mathbf{H} - \mathbf{H}\mathbf{P}) \\ &+ \frac{\nu_1}{2} \left(\mathbf{P}\mathbf{H} + \mathbf{H}\mathbf{P} - \frac{2}{3} (\mathbf{P} \cdot \mathbf{H}) \mathbb{I}_3 \right) \\ &+ \zeta \nabla \cdot (\Delta \mu \mathbf{Q}) \end{aligned} \quad (3.17)$$

where we have additional stress by the rotation of \mathbf{P} towards \mathbf{H} , stresses due to the anisotropy of the material and active stress.

Impact of thin shell geometry To shed a light on the specific nature of the additional constraints imposed by thin shell geometries, we imagine the previous model on a two dimensional surface \mathcal{S} , topological equivalent to a sphere. As [50] states the Actin molecules are aligned parallel to the surface and therefore \mathbf{P} is restricted to the tangential space \mathcal{TS} of \mathcal{S} as well. Assuming the deformations \mathbf{V} to be also tangential, we end up with a set of coupled tangential tensor fields with degree zero (scalars n), one (vectors \mathbf{P} , \mathbf{V}) and two (tensors $\boldsymbol{\sigma}^d$).

Such restricted state spaces require a specific notion of derivatives $\nabla_{\mathcal{S}}$, since we expect the gradients of those fields to be tangential as well. Combined with the premise of invariance under coordinate transformation only a limited set of derivative notions is admissible. Here we use the Levi-Civita connection, defined by a compatibility condition of metric \mathbf{g} and the Christoffel symbols Γ . Generally speaking \mathbf{g} describes the local tangential space of \mathcal{S} while Γ covers the spatial modulations of \mathbf{g} . Denoting by i, j, \dots coordinates along tangential directions we can define

the surface bound derivative along directional derivatives

$$d = 0, n : \mathcal{S} \mapsto \mathbb{T}^0 \mathcal{S} \quad [\nabla_{\mathcal{S}} n]_i = \partial_i n \quad (3.18)$$

$$d = 1, \mathbf{V} : \mathcal{S} \mapsto \mathbb{T}^1 \mathcal{S} \quad [\nabla_{\mathcal{S}} \mathbf{V}]_{ij} = \partial_j V_i - \Gamma_{ij}^k V_k \quad (3.19)$$

$$d = 2, \boldsymbol{\sigma} : \mathcal{S} \mapsto \mathbb{T}^2 \mathcal{S} \quad [\nabla_{\mathcal{S}} \boldsymbol{\sigma}]_{ijk} = \partial_k \sigma_{ij} - \Gamma_{ki}^l \sigma_{lj} - \Gamma_{kj}^l \sigma_{il} \quad (3.20)$$

By these definition, we observe the derivatives of tensor fields to include a number of Christoffel symbols matching the tensorial degree of the considered field. A first hint that dynamical equations of non-scalar fields will couple to the geometric properties of the surface. A more detailed introduction to the notions of differential geometry is given in section 3.1.4.

3.1.3 A Brief Detour to Topology

A widely observed physical effect, see [10] for a review, is closely related to topology and is called geometric frustration. This denotes the situation where a physically favorable ordering, e. g. energetically minimal, can not propagate throughout the whole domain due to geometric properties of the domain. In such situations localized areas of broken order, so called defects, emerge and break symmetries in the system states. Furthermore, these defects turned out to be pivotal entities in the dynamics of various physical systems [31, 85, 35].

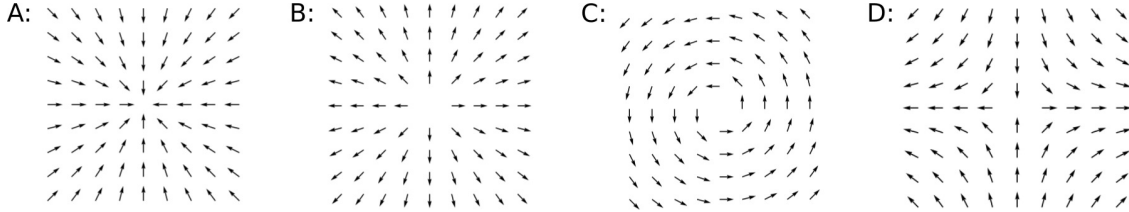


Figure 3.1: **Topological defect types of vector fields:** Defect types with topological charge +1 [A]: sink, [B]: source, [C]: vortex. [D]: saddle point defect with charge -1 . Figure adapted from [10].

The effect of geometric frustration can be described in terms of topology by Euler Characteristic χ of a domain and the so called isolated zeros \mathbf{x}_i . The Euler Characteristic χ is a number describing the topological structure of the domain regardless of its specific shape, e. g. any two dimensional surface without a “hole” is topological equivalent to a sphere with $\chi(\mathcal{S}) = 2$. Considering a normalized vector field \mathbf{P} defined on this domain and aligned tangential to the boundary we can define isolated zeros as localized discontinuities in the vector field. Further these discontinuities can be characterized by the index or topological charge of the discontinuity $\text{index}(\mathbf{x}_i)$, see figure 3.1 for examples. A central concept in this topic is formulated by the Poincaré Hopf theorem [47].

$$\sum_i \text{index}(\mathbf{x}_i) = \chi(\mathcal{S}) \quad (3.21)$$

It establishes that, regardless of the chosen normalized vector field \mathbf{P} on domain \mathcal{S} , the topological charges of the isolated zeros of \mathbf{P} will sum up to the Euler Characteristic $\chi(\mathcal{S})$. Also, with the

notion of a topological charge we can think of defects in an analogy to electric charged particles. Defects, as charged particles, repel each other for topological charges of matching sign while opposing charges attract each other and annihilate on contact.

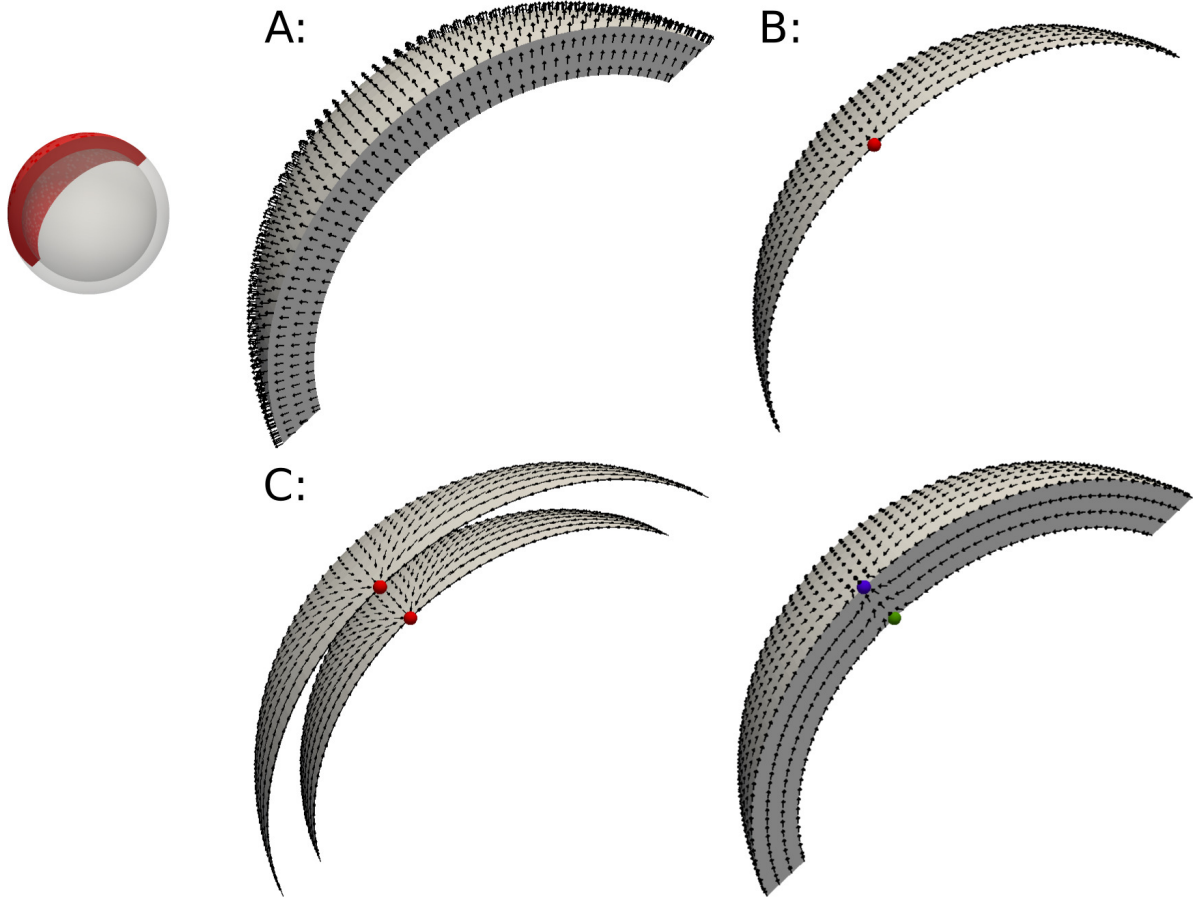


Figure 3.2: **Topological constraints for vector fields in thin shells and surfaces:** Plots show piece, marked in red, of spherical thin shell. [A]: Defect free vector field defined on thin shell \mathcal{S}_h with $\chi(\mathcal{S}_h) = 0$. [B]: Spherical surface $\chi\mathcal{S} = 2$ with tangential vector field requires defects, red dot marks sink defect. [C]:(left) Boundary of \mathcal{S}_h consists of two concentric spheres with nonzero Euler characteristic $\chi(\partial\mathcal{S}_h) = 4$. Here a configuration of tangential vector field with two sink (red dots) $\text{index}_{\partial\mathcal{S}_h} = +1$ defects. (right) A vector field in \mathcal{S}_h conforming with tangential vector fields at $\partial\mathcal{S}_h$. Two defects are induced but, due to changed dimension, topological charge differs. Sink defect (blue dot) with $\text{index}_{\mathcal{S}_h} = +1$ and saddle point defect (green dot) with $\text{index}_{\mathcal{S}_h} = -1$. Thin shell limit for $h \rightarrow 0$ yields transition from volume to surface and changing Euler characteristic. Limiting vector field, as shown in [B], can be considered as average (point wise along normal direction) of vector fields on $\partial\mathcal{S}_h$.

Considering a gel consisting of elongated particles, with a distinguished head, which tend to align parallel. If this gel is restricted to a two dimensional sphere like surface \mathcal{S} and the particles are forced to align tangential than, due to $\chi(\mathcal{S}) = 2$, no defect free states are possible and at least one defect has to occur. On the other hand side, if we consider the associated thin shell \mathcal{S}_h domain, e. g. a tubular extension of \mathcal{S} with thickness h , we have a three dimensional domain with $\chi(\mathcal{S}_h) = 0$. For such geometries one would expect the existence of a defect free configuration, e. g. figure 3.2-A.

Therefore, the question arises what happens in process in the transition between the topological different spaces of a thin shell and a surface for $h \rightarrow 0$.

The answer lies in the boundary conditions chosen on $\partial\mathcal{S}_h$. The boundary of the thin shell consists of two sphere like surfaces such that $\chi(\partial\mathcal{S}_h) = 4$. Requiring a tangential alignment of the particles on this boundary implies the existence of at least two defects, see figure 3.2-B. These defects on the boundary induce the existence of defects in the thin shell. But since topological charges differ depending on the dimensionality of the domain, some defects in the thin shell change the sign of their charge and thereby the defect configurations conforms the Poincaré Hopf theorem, see figure 3.2-B. In such set up, it is plausible that for vanishing thickness of the thin shell, the defects merge to a surface defect as shown in figure 3.2-C.

This illustrative examples highlights the fundamental impact of boundary conditions in the process of thin shell limit $h \rightarrow 0$ and motivates the description of thin shell dynamics by effective surface models.

3.1.4 Notions of Differential Geometry

Tensor fields in flat and curved spaces For notational compactness we make two general prerequisites. First, we adopt the Ricci calculus convention where repeated indices in a term imply summation over this index. Second, most of the tensor formulations presented here are invariant w.r.t. coordinate transformations, thus a co- and contravariant distinction in the object representation is not necessary.

We consider a connected subset $V \subset \mathbb{R}^n$ with a parametrization $\mathcal{X} : \mathcal{U} \mapsto V$ by coordinates u_i . With directional derivatives of \mathcal{X} along the coordinates we define the associated basis $\mathbf{e}_i = \partial_i \mathcal{X}$. With the full contraction "·" of \mathbb{R}^n we obtain the metric by

$$g_{ij} = \partial_i \mathcal{X} \cdot \partial_j \mathcal{X}. \quad (3.22)$$

A scalar product for vector fields on V is then given by $\langle \mathbf{t}, \mathbf{v} \rangle_V = t_i g^{ij} v_j$. The Christoffel symbols of second kind are defined by

$$\Gamma_{ij}^k = \frac{1}{2} g^{kl} (\partial_i g_{jl} + \partial_j g_{il} - \partial_l g_{ij}). \quad (3.23)$$

If for V a metric exists such that \mathbf{g} does not depend on the elements $\mathbf{x} \in V$, e.g. the metric is equivalent to the Kronecker delta $g_{ij}(\mathbf{x}) = \delta_{ij}$, and the parametrization \mathcal{X} is smooth on the periodically extended coordinate space \mathcal{U} we call V a flat space, otherwise V is called curved.

In this framework the tensor field \mathbf{t} defined on V of degree d is a set of pointwise linear forms which can be expressed along the coordinates of an associated product basis, namely

$$\mathbf{t} : V \mapsto L(\underbrace{V \times V \times \dots \times V}_{d \text{ times}}; \mathbb{R}), \quad \mathbf{t} = t_{i_1 \dots i_d} \mathbf{e}^{i_1} \dots \mathbf{e}^{i_d} \quad (3.24)$$

To switch between components and object representation brackets $[]$ and $\{\}$ are used, i. e., for a 2-tensor \mathbf{t} we write $[t]_{ij} = t_{ij}$ for the components and $\{t_{ij}\} = \mathbf{t}$ for the object. The notions of full contraction and scalar product are adopted to tensor fields by a contraction/summation over all components

$$\mathbf{t} : \mathbf{v} = t_{i_1 \dots i_d} v^{i_1 \dots i_d}, \quad \langle \mathbf{t}, \mathbf{v} \rangle_V = t_{i_1 \dots i_d} g^{i_1 j_1} \dots g^{i_d j_d} v_{j_1 \dots j_d} \quad (3.25)$$

Reviewing this tensor field definitions, we point out the invariance under coordinate change complying the covariance principle of physics. To preserve this covariance also for gradients of tensor fields we use the metric preserving Levi-Civita connection. This notion of derivative is defined by

$$[\nabla \mathbf{t}]_{i_1 \dots i_d k} = \partial_k t_{i_1 \dots i_d} - \left(\Gamma_{k i_1}^l t_{l i_2 \dots i_d} + \dots + \Gamma_{k i_d}^l t_{i_1 \dots i_{d-1} l} \right) \quad (3.26)$$

In component wise description of $\nabla \mathbf{t}$ we use ; to separate the component denoting with the derivative, e. g. the derivative of a vector \mathbf{v} can be expressed by the components of the two tensor or along the derivative $[\nabla \mathbf{v}]_{ik} = v_{i;k}$

Surfaces and thin shells These general definitions apply canonical to an oriented two dimensional surface $\mathcal{S} \subset \mathbb{R}^3$ where $\boldsymbol{\nu}$ denotes the outward pointing surface normals. Along the parametrization $\mathcal{X}_{\mathcal{S}}(u, v) \mapsto \mathbb{R}^3$ a coordinate basis pair is defined, which will be indexed by lower case letters i, j, k, \dots . We point out that for Euler characteristic $\chi(\mathcal{S}) \neq 0$ the surface \mathcal{S} is a curved space. Denoting the surface metric by \mathbf{g} and surface Christoffel symbols γ , covariant derivative $\nabla_{\mathcal{S}}$, we can define the curvature terms of the surface. The shape operator $[\mathcal{B}]_{ij} = \partial_i \mathcal{X}_{\mathcal{S}} : \partial_j \boldsymbol{\nu}$ with Gaussian $\mathcal{K} = \det\{\mathcal{B}^{ij}\}$ and mean curvature $\mathcal{H} = \mathcal{B}^i_i$. Further we can define the tangent space \mathcal{TS} pointwise by $\mathcal{TS} : \cup_{\mathbf{x} \in \mathcal{S}} \mathcal{T}_{\mathbf{x}} \mathcal{S}$ such that $\mathcal{T}_{\mathbf{x}} \mathcal{S} \times \boldsymbol{\nu} = \mathbb{R}^3$. A tangential tensor field of degree d is then defined by

$$\mathbf{t} : \mathcal{S} \mapsto L(\underbrace{\mathcal{TS} \times \mathcal{TS} \times \dots \times \mathcal{TS}}_{d \text{ times}}; \mathbb{R}), \quad \mathbf{t} = t_{i_1 \dots i_d} \mathbf{e}^{i_1} \dots \mathbf{e}^{i_d}. \quad (3.27)$$

As notational convention we use lower case letters to denote tangential tensor fields defined on a surface, e. g. \mathbf{p} or \mathbf{q} .

The thin shell \mathcal{S}_h is then defined as a tubular extension of \mathcal{S} with constant thickness h by an augmented parametrization

$$\mathcal{X}_{\mathcal{S}_h} : \mathcal{U} \times [-h/2, h/2] \mapsto \mathcal{S}_h, \quad \mathcal{X}_{\mathcal{S}_h}(u, v, \xi) = \mathcal{X}_{\mathcal{S}}(u, v) + \xi \boldsymbol{\nu} \quad (3.28)$$

For a sufficient small h , such that $h\|\mathcal{B}\| < 1$, this description is unique[57]. Despite that \mathcal{S} is a curved space and the thin shell coordinates (u, v, ξ) and metric \mathbf{G} are spatial dependent, the thin shell is a flat space and a description along the Euclidean coordinates exists. Nonetheless, those two descriptions are equivalent and both indexed by capital letters I, J, K, \dots .

Tensorfields defined on \mathcal{S}_h are denoted by capital letters, e. g. \mathbf{P} or \mathbf{Q} . The metric and Christoffel

symbols of the thin shell are again defined canonical. But expressed in thin shell coordinates these can be related to the surface quantities. For the metric, details see [57],

$$G_{ij} = g_{ij} - 2\xi\mathcal{B}_{ij} + \xi^2\mathcal{B}_i^k\mathcal{B}_{kj} \quad (3.29)$$

$$G_{i\xi} = G_{\xi i} = 0 \quad (3.30)$$

$$G_{\xi\xi} = 1 \quad (3.31)$$

while the Christoffels symbols relate by

$$\Gamma_{ij}^k = \gamma^k_{ij} + \mathcal{O}(\xi) \quad \Gamma_{\xi\xi}^K = \Gamma_{K\xi}^\xi = \Gamma_{\xi K}^\xi = 0 \quad (3.32)$$

$$\Gamma_{ij}^\xi = \mathcal{B}_{ij} + \mathcal{O}(\xi) \quad \Gamma_{\xi i}^k = \Gamma_{\xi i}^k = -\mathcal{B}_i^k + \mathcal{O}(\xi) \quad (3.33)$$

As further tool we define restrictions operators. the operator $\cdot|_{\mathcal{S}}$ yields the restriction of a thin shell tensor field to the surface domain while $\Pi_{\mathcal{S}}[\cdot]$ is the restriction to a tangential surface tensor field. Later Operator can be described in thin shell and Euclidean coordinates by

$$\Pi_{\mathcal{S}}[\mathbf{Q}]_{ij} = [\mathbf{Q}|_{\mathcal{S}}]_{ij} \quad \text{or} \quad \Pi_{\mathcal{S}}[\mathbf{Q}]_{IJ} = \Pi_I^L[\mathbf{Q}|_{\mathcal{S}}]_{LK}\Pi_J^K \quad (3.34)$$

where Π is the projection matrix defined by $\Pi_{IJ} = 1/2(\nu_I\nu_J - \delta_{IJ}) = g_{IJ}$.

It comes as no surprise that under such close relation of the geometric properties also the covariant derivatives of surface and thin shells can be related. Consider a thin shell tensor field \mathbf{T} such that $\Pi_{\mathcal{S}}[\mathbf{T}] = \mathbf{t}$ it has been derived in [55] that

$$[\nabla_{\mathcal{S}}\mathbf{t}]_{i_1\dots i_d k} = ([\nabla\mathbf{T}]_{i_1\dots i_d k} + [\mathcal{B}_{ki_1}T_{\xi i_2\dots i_d} + \dots + \mathcal{B}_{ki_d}T_{i_1\dots i_{d-1}\xi}])|_{\mathcal{S}} \quad (3.35)$$

Function spaces and differential operators With this definitions we can turn now to suitable function norms and spaces. We define L^2 scalar products by

$$\langle \mathbf{t}, \mathbf{u} \rangle_{L^2(\mathcal{S})} = \int_{\mathcal{S}} \langle \mathbf{t}, \mathbf{u} \rangle_{\mathcal{S}} d\mathcal{S} \quad (3.36)$$

$$\langle \mathbf{T}, \mathbf{U} \rangle_{L^2(\mathcal{S}_h)} = \frac{1}{h} \int_{\mathcal{S}_h} \mathbf{T} : \mathbf{U} d\mathcal{S}_h \quad (3.37)$$

For $\Pi_{\mathcal{S}}[\mathbf{T}] = \mathbf{t}$ and $\Pi_{\mathcal{S}}[\mathbf{U}] = \mathbf{u}$ we yield $\langle \mathbf{t}, \mathbf{u} \rangle_{L^2(\mathcal{S})} = \langle \mathbf{T}, \mathbf{U} \rangle_{L^2(\mathcal{S}_h)} + \mathcal{O}(h^2)$. With the induced norms $\|\cdot\|_{\mathcal{S}}$ and $\|\cdot\|_{\mathcal{S}_h}$ we define function spaces of tensor fields with degree d

$$L^2(\mathcal{S}, d) = \{ \mathbf{t} : \mathcal{S} \mapsto L(\underbrace{\mathcal{T}\mathcal{S} \times \dots \times \mathcal{T}\mathcal{S}}_{d \text{ times}}; \mathbb{R}), \|\mathbf{t}\|_{\mathcal{S}} < \infty \} \text{ and} \quad (3.38)$$

$$L^2(\mathcal{S}_h, d) = \{ \mathbf{T} : \mathcal{S} \mapsto L(\underbrace{\mathcal{S}_h \times \dots \times \mathcal{S}_h}_{d \text{ times}}; \mathbb{R}), \|\mathbf{T}\|_{\mathcal{S}_h} < \infty \}. \quad (3.39)$$

Starting at these spaces a tensor valued weak derivative and associated solution theory can be established. Nonetheless we will not discuss matters of regularity or smoothness. Therefore we assume throughout the argumentation, sufficient properties to ensure existence and uniqueness of

solutions of the related state equations.

Given these assumptions we can define the well known differential operators gradient, divergence and rotation in a consistent way on surfaces and in thin shells for any tensorfield with degree d by

$$\begin{array}{ccc} \mathcal{S} & & \mathcal{S}_h \\ \text{Gradient:} & [\text{grad}_{\mathcal{S}} \mathbf{t}]_{i_1 \dots i_d k} = [\nabla_{\mathcal{S}} \mathbf{t}]_{i_1 \dots i_d k} & [\text{grad} \mathbf{T}]_{I_1 \dots I_d K} = [\nabla \mathbf{T}]_{I_1 \dots I_d K} \end{array} \quad (3.40)$$

$$\text{Divergence:} \quad [\text{div}_{\mathcal{S}} \mathbf{t}]_{i_1 \dots i_{d-1}} = g_{i_d i_k} [\nabla_{\mathcal{S}} \mathbf{t}]_{i_1 \dots i_d k} \quad [\text{div} \mathbf{T}]_{I_1 \dots I_{d-1}} = G_{I_d K} [\nabla \mathbf{T}]_{I_1 \dots I_d K} \quad (3.41)$$

Further to define the rotation of a tensor field we use the Levi-Civita tensors \mathbf{E} and \mathbf{e} of associated dimension. For the volume we define the rotation by

$$\text{Rot} \mathbf{T}_{I_1 \dots I_{d-1} J} = -E_J^{I_d K} [\nabla \mathbf{T}]_{I_1 \dots I_d K} \quad (3.42)$$

For the thin shell we have a compatible notion of rotation by using $E_{\xi i j} = -E_{i \xi j} = E_{i j \xi} = e_{ij} + \mathcal{O}(h^2)$. In this sense we obtain on the two dimensional surface a rotation $[\text{rot}_{\mathcal{S}} \mathbf{t}]_{i_1 \dots i_{d-1}} = -e_{i_d k} [\nabla_{\mathcal{S}} \mathbf{t}]_{i_1 \dots i_d k}$ reducing the tensorial degree. A dual or adjoint rotation $\text{Rot}_{\mathcal{S}}$ increases the tensorial degree and can be derived along the w.r.t. $L^2(\mathcal{S}_h)$, see [54].

For the specific cases of directors and Q tensors we define the admissible state spaces by

$$\mathcal{P}_{\mathcal{S}} = \{\mathbf{p} \in L^2(\mathcal{S}, 1), \text{ twice differentiable, } \nabla_{\mathcal{S}} \mathbf{p} \in L^2(\mathcal{S}, 2), \nabla_{\mathcal{S}}(\nabla_{\mathcal{S}} \mathbf{p}) \in L^2(\mathcal{S}, 3)\} \quad (3.43)$$

$$\begin{aligned} \mathcal{Q}_{\mathcal{S}} = \{\mathbf{q} \in L^2(\mathcal{S}, 2), \text{ symmetric and, } \text{tr}_{\mathcal{S}}(\mathbf{q}) = \mathbf{g} : \mathbf{q} = 0, \text{ twice differentiable,} \\ \nabla_{\mathcal{S}} \mathbf{q} \in L^2(\mathcal{S}, 3), \nabla_{\mathcal{S}}(\nabla_{\mathcal{S}} \mathbf{q}) \in L^2(\mathcal{S}, 4)\} \end{aligned} \quad (3.44)$$

The thin shell definitions of state spaces are analogous, except for the volume trace $\text{tr}(\mathbf{Q}) = \mathbf{G} : \mathbf{Q}$. Please note, this notion does not conform with the surface trace in a sense $\text{tr}_{\mathcal{S}}(\Pi_{\mathcal{S}}[\mathbf{Q}]) \neq \text{tr}(\mathbf{Q})$, and requires extra considerations in the modelling discussed in section 3.3.1.

3.2 Intrinsic and Extrinsic Contributions on Equilibrium States of Polar Ordering

In this section we consider the Frank Oseen model, describing equilibria for fields of polar order in volume $V \subset \mathbb{R}^3$. For this basic model we will derive the thin shell limit to obtain a formulation suitable for two dimensional surface \mathcal{S} embedded in \mathbb{R}^3 .

By comparing the thin shell limit model with a Frank Oseen model derived directly on a two dimensional curved space we discuss coupling mechanisms between surface curvature and order variable. After considering the impact of system size we investigate by geometrical variation how curvature influences the stability of defect configurations. We conclude the section by evaluating the applied methods and discussion of the results in the context of cellular length scales.

3.2.1 Frank Oseen Model and its Thin Shell Limit

The unit free Frank Oseen model considers a field of unit sized vectors \mathbf{P} , which we call director. As ground state a homogeneous configuration of parallel directors is defined and any deviations from this ground state are penalized by a free energy.

$$\mathcal{F}_{FO}^V(\mathbf{P}) = \frac{1}{2} \int_V K_1 (\nabla \cdot \mathbf{P})^2 + K_2 (\mathbf{P} \cdot (\nabla \times \mathbf{P}))^2 + K_3 \|\mathbf{P} \times (\nabla \times \mathbf{P})\|^2 dV \quad (3.45)$$

Here K_1 , K_2 , and K_3 are the Frank phenomenological constants defining the elastic response to spatial variations of \mathbf{P} , namely (from left to right) for splay, twist, and bend.

For our discussion of fundamental properties, we consider the one-constant approximation $K := K_1 = K_2 = K_3$. Using further $\|\mathbf{P}\| = 1$, the elastic energy (3.45) thus reads

$$\mathcal{F}_{el}^V(V) = \frac{K}{2} \int_V (\nabla \cdot \mathbf{P})^2 + \|\nabla \times \mathbf{P}\|^2 dV \quad (3.46)$$

In this model, any defects are modeled as discontinuities of measure zero. Since we are interested in a global smooth variable \mathbf{P} , we adjust the model by dropping the unit length prerequisite for \mathbf{P} . Analogous to other models, e. g. the Landau-de Gennes model, we consider \mathbf{P} as a macroscopic variable describing the average orientation of microscopic particles and $\|\mathbf{P}\|$ as order parameter describing the variance in the microscopic orientation. In this sense we consider $\|\mathbf{P}\| = 0$ as isotropic distribution and $\|\mathbf{P}\| = 1$ the perfectly aligned (also called nematic) distribution. Enabling localized defects we use an even potential with parameter ω_n . In analogy to Landau-de Gennes this energy is labeled “thermotropic”.

$$\mathcal{F}_{th}^V(\mathbf{P}) = \frac{\omega_n}{4} \int_V (\|\mathbf{P}\|^2 - 1)^2 dV \quad (3.47)$$

Thin shell limit We consider thin shell geometries as tubular extensions \mathcal{S}_h of a surface \mathcal{S} with characteristic length (e. g. maximum edge length of bounding box) l with constant thickness h where $h \ll l$. Since we are interested in spatial configurations of \mathbf{P} in tangential direction of \mathcal{S} we assume a tangential alignment of \mathbf{P} throughout \mathcal{S}_h and \mathbf{P} to be constant along the direction of surfaces normal $\boldsymbol{\nu}$.

$$\mathbf{P}|_{\mathcal{S}} = \mathbf{p} \in T\mathcal{S} \text{ and } P_{;\xi}^I = 0 \quad (3.48)$$

Defining the thin shell energy as average in $\boldsymbol{\nu}$ direction

$$\mathcal{F}^{\mathcal{S}_h}(\mathbf{P}, h) = \frac{1}{h} \left[\mathcal{F}_{el}^{\mathcal{S}_h}(\mathbf{P}) + \mathcal{F}_{th}^{\mathcal{S}_h}(\mathbf{P}) \right] \quad (3.49)$$

we can perform the limit $h \rightarrow 0$ to obtain a surface bound energy

$$\begin{aligned}\mathcal{F}^{\mathcal{S}}(\mathbf{p}) &= \frac{K}{2} \int_{\mathcal{S}} (\operatorname{div}_{\mathcal{S}} \mathbf{p})^2 + (\operatorname{rot}_{\mathcal{S}} \mathbf{p})^2 + \|\mathcal{B} \cdot \mathbf{p}\|^2 \, d\mathcal{S} \\ &\quad + \frac{\omega_n}{4} \int_{\mathcal{S}} (\|\mathbf{p}\|^2 - 1)^2 \, d\mathcal{S} \\ &= \mathcal{F}_{el}^{\mathcal{S}}(\mathbf{p}) + \mathcal{F}_{th}^{\mathcal{S}}(\mathbf{p})\end{aligned}\tag{3.50}$$

In the thin shell limit, we observe the interplay of curved space and the vector valued field \mathbf{P} in the sense that normal components change along tangential directions, $P_{;i}^{\xi} \neq 0$. Therefore, the associated components of the thin shell Christoffel symbols do not vanish regardless of thickness h , namely $P_{;i}^{\xi} = \underline{\Gamma}_{jK}^{\xi} P^K = \mathcal{B}_{jk} P^k + \mathcal{O}(\xi)$. For complete derivation of the thin shell limit we refer to [54].

Dynamic equations We obtain dynamic equations for minimizing $\mathcal{F}^{\mathcal{S}}(\mathbf{p})$ by a L^2 -gradient flow approach,

$$\partial_t \mathbf{p} = -\delta \mathcal{F}^{\mathcal{S}}(\mathbf{p})\tag{3.51}$$

where the variation of $\mathcal{F}^{\mathcal{S}}$ can be interpreted w.r.t. the $L^2(\mathcal{S})$ scalar product. For $\mathbf{q} \in \mathcal{P}_{\mathcal{S}}$ this reads

$$\begin{aligned}\delta \mathcal{F}^{\mathcal{S}}(\mathbf{p}) &= \int_{\mathcal{S}} \left\langle \frac{\partial \mathcal{F}^{\mathcal{S}}(\mathbf{p})}{\partial \mathbf{p}}, \mathbf{q} \right\rangle_{\mathcal{S}} \, d\mathcal{S} \\ &= \int_{\mathcal{S}} K (\operatorname{div}_{\mathcal{S}} \mathbf{p} \operatorname{div}_{\mathcal{S}} \mathbf{q} + \operatorname{rot}_{\mathcal{S}} \mathbf{p} \operatorname{rot}_{\mathcal{S}} \mathbf{q}) + K \langle \mathcal{B} \cdot \mathbf{p}, \mathcal{B} \cdot \mathbf{q} \rangle_{\mathcal{S}} + \omega_n (\|\mathbf{p}\|^2 - 1) \langle \mathbf{p}, \mathbf{q} \rangle_{\mathcal{S}} \, d\mathcal{S} \\ &= \int_{\mathcal{S}} K \langle \Delta_{\mathcal{S}}^{\text{dR}} \mathbf{p}, \mathbf{q} \rangle + K \langle \mathcal{B}^2 \cdot \mathbf{p}, \mathbf{q} \rangle_{\mathcal{S}} + \omega_n (\|\mathbf{p}\|^2 - 1) \langle \mathbf{p}, \mathbf{q} \rangle_{\mathcal{S}} \, d\mathcal{S}\end{aligned}\tag{3.52}$$

with $\Delta_{\mathcal{S}}^{\text{dR}}(\cdot) := -(\operatorname{grad}_{\mathcal{S}} \operatorname{div}_{\mathcal{S}}(\cdot) + \operatorname{Rot}_{\mathcal{S}} \operatorname{rot}_{\mathcal{S}}(\cdot))$ the Laplace-deRham operator. This leads to the evolution equation

$$\partial_t \mathbf{p} + K \Delta_{\mathcal{S}}^{\text{dR}} \mathbf{p} + K \mathcal{B}^2 \mathbf{p} + \omega_n (\|\mathbf{p}\|^2 - 1) \mathbf{p} = 0\tag{3.53}$$

in $\mathcal{S} \times (0, \infty)$ with the initial condition $\mathbf{p}(t=0) = \mathbf{p}_0 \in \mathcal{TS}$. The gradient flow approach guarantees dissipative dynamics and stationary solutions of (3.53) as local minima of $\mathcal{F}^{\mathcal{S}}$.

3.2.2 Comparison of Intrinsic and Thin Shell Model

Alternatively to deriving the surface model via a thin shell limit one could also define the elastic energy by formulating the Frank-Oseen energy immediately on a two dimensional surface. So ignoring the embedding space, by just replacing the covariant derivatives in (3.46) and using \mathbf{p} instead of \mathbf{P} , we yield following "intrinsic" surface energy, discussed in [10].

$$\mathcal{F}_{el}^{\mathcal{S}, IN}(\mathbf{p}) = \frac{K}{2} \int_{\mathcal{S}} (\operatorname{div}_{\mathcal{S}} \mathbf{p})^2 + (\operatorname{rot}_{\mathcal{S}} \mathbf{p})^2 \, d\mathcal{S}\tag{3.54}$$

Inserting consistently rotated vector field $R(\mathbf{p}, \Delta\theta) = \cos(\Delta\theta)\mathbf{p} + \sin(\Delta\theta)(\boldsymbol{\nu} \times \mathbf{p})$ we find this energy to be invariant under such rotations. Further, as discussed in [10], this energy and its associated dynamic equation are sensitive to curvature of \mathcal{S} in the sense that defects are attracted to areas of curvature with matching sign of their topological charge. Therefore in such systems an interplay of Coloumb like defect-defect interaction and a geometric forcing acting on the individual defect positions exists.

The previously derived thin shell limit energy, see elastic contribution $\mathcal{F}_{el}^S(\mathbf{p})$ in (3.51), extends this intrinsic model by an extrinsic contribution term $\|\mathcal{B} \cdot \mathbf{p}\|^2$, which can be split into two parts

$$\frac{K}{2} \int_{\mathcal{S}} \|\mathcal{B} \cdot \mathbf{p}\|^2 d\mathcal{S} = \frac{K}{2} \int_{\mathcal{S}} \mathcal{H} \langle \mathcal{B} \cdot \mathbf{p}, \mathbf{p} \rangle - \mathcal{K} \|\mathbf{p}\|^2 d\mathcal{S} \quad (3.55)$$

$\langle \mathcal{B} \cdot \mathbf{p}, \mathbf{p} \rangle$ can be considered as an anisotropic scalar product w.r.t. to the local curvature. Such that, minimizing this energy contribution implies aligning \mathbf{p} along lines of minimal curvature. In consequence, see figure 3.3, the energetic invariance under consistent rotation observed in the intrinsic surface model is not present in the thin shell limit model. The prefactor of mean curvature \mathcal{H} rescales the contribution and might change the preferred alignment w.r.t. lines of minimal curvature for complex geometries where $\text{sgn}(\mathcal{H}) \neq \text{sgn}(\mathcal{K})$.

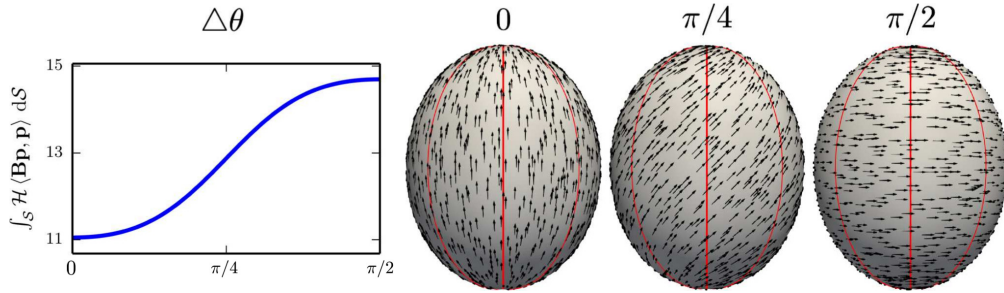


Figure 3.3: **Extrinsic curvature contributions eliminate rotational invariance:** Energy contribution of $\int_{\mathcal{S}} \mathcal{H} \langle \mathcal{B}\mathbf{p}, \mathbf{p} \rangle d\mathcal{S}$ under rotation $\Delta\theta$ of director field \mathbf{p} on an ellipsoid with major axis $[1, 1, 1.25]$. Energetic minimum at $\Delta\theta = 0$ with director parallel to lines of minimal curvature (marked in red), increased energy at intermediate state at $\Delta\theta = \pi/4$ and maximal energy for director orthogonal to lines of minimal curvature at $\Delta\theta = \pi/2$.

The contribution $-\mathcal{K}\|\mathbf{p}\|^2$ can be related to the thermotropic potential \mathcal{F}_{th}^S and introduces a cross coupling to the geometries curvature.

$$\int_{\mathcal{S}} -\frac{K}{2} \mathcal{K} \|\mathbf{p}\|^2 + \frac{\omega_n}{4} (\|\mathbf{p}\|^4 - 2\|\mathbf{p}\|^2 + 1) d\mathcal{S} \quad (3.56)$$

This can be interpreted as a superposition of a double well potential (scaled by $\omega_n/4$) and a geometric potential (scaled by $-K/2$). The energetic minima's of this energy can be determined pointwise and are given by

$$\|\mathbf{p}^*(\mathbf{x})\| = \sqrt{1 + \frac{K}{\omega_n} \mathcal{K}(\mathbf{x})} \quad (3.57)$$

Therefore, we observe an impact of the local curvature scaled by the ratio of constants K/ω_n . For areas with sufficient strong, negative Gaussian curvature, $\mathcal{K} \leq -K/\omega_n$, only the isotropic state is stable. Figure 3.4 exemplifies such situation for a sequence of Eneper disc pieces, scaled by factor s .

We define the sequence of such manifolds by

$$\mathcal{X}_{\mathcal{E}}(s) : (u, v) \in [-1/2, 1/2]^2 \mapsto \mathbf{x} = \frac{1}{3} \begin{bmatrix} 1/3u^3s^3 - u^2vs^3 - us \\ -1/3v^3s^3 + uv^2s^3 + vs \\ (u^2 - v^2)s^2 \end{bmatrix} \quad (3.58)$$

Further, the resulting manifolds \mathcal{E} are rescaled to have matching surface area of 1. As boundary condition we used homogeneous Neumann type, to enable a defect free minimal energy configuration. Starting from a defect free homogeneous director configuration we numerically evaluate the configurations of \mathbf{p} with minimal energy $\mathcal{F}^{\mathcal{E}}(\mathbf{p})$ for various values of s .

We observe for increasing s an overall increase in the magnitude of Gaussian curvature. Since the Eneper disc is a minimal surface the mean curvature remains unaffected $\mathcal{H} = 0$. For low values of $s \in [0, 2]$ we observe a continuous deformation of an uniform configurations. For higher values $s \in [2, 3]$, we observe an expanding area with reduced $\|\mathbf{p}\| < 1$, centered at the saddle, until for $s > 3$ only the isotropic phase exists.

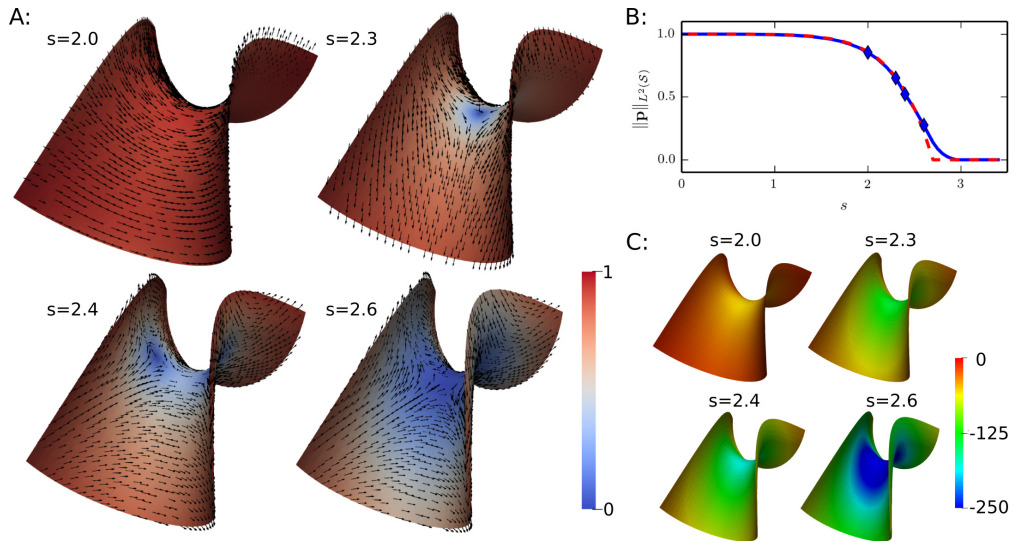


Figure 3.4: **Negative Gaussian curvature induces localized broken order:** [A]: minimal energy configurations for several values of s , glyphs indicate director, colors show magnitude [B]: $L^2(\mathcal{E})$ norm of minimal energy configuration (blue line, diamonds indicate values of states shown in [A]) and predicted value by $\|\mathbf{p}^*(\mathbf{x})\|_{L^2(\mathcal{E})}$ (red dashed line) [C]: Distribution of Gaussian curvature on the geometry. Energy parameters $K = 1$, $\omega_n = 200$

In the curvature induced transient between ordered and isotropic phase, we also observe a reordering of the director field. Starting at an uniform field a saddle point defect is inserted at $s \approx 2.3$. For high values a second saddle point defect occurs and enforces a symmetric out of

center position of both defects. Eventually the curvature has reached a critical value in the area close to the center and the intermediate defect structures are unified to a single area of isotropic ordering. Nonetheless, reviewing the very good agreement of theoretical prediction (3.57) with the simulated values of the transition, see figure 3.4-B, we assess these reordering effects as secondary to the ordered-isotropic transient.

3.2.3 Curvature of Geometry Influences Stability of Defect Configurations

To refine the understanding of the interplay of curvature and ordering, we consider a sequence of surfaces with non-constant curvature. The sequence starts with the unit sphere, which is deformed into a nonic shape for increasing form parameter C , for details of these transformation see [54]. These nonic shapes are characterized by three regions with high positive Gaussian curvature and a single saddle with negative \mathcal{K} , see figure 3.5 for examples. All surfaces have $\chi(\mathcal{S}) = 2$, thus inhibiting defect free states. To investigate the energy value $\mathcal{F}^{\mathcal{S}(C)}[\mathbf{p}^*]$ of a stationary solution \mathbf{p}^* and the

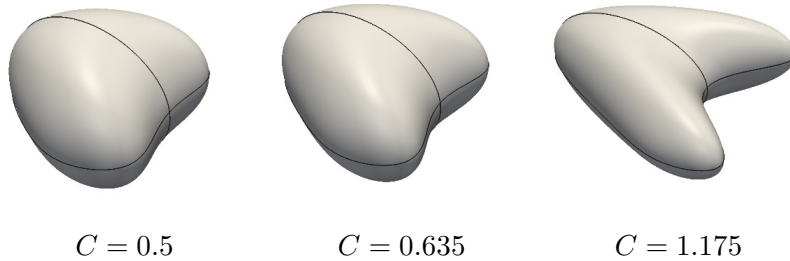


Figure 3.5: **Nonic surfaces corresponding to three different stretching parameters C :** Related to results shown in figure 3.7. [Left] Nonic surface with defect fusion-time > 0 , [Center] four-defect configuration gets stable, [Right] four-defect configuration is energetically equivalent to two-defect configuration.

stability of defect configurations we analyze the evolution of two different initial values $\mathbf{p}_{0,4}$ and $\mathbf{p}_{0,2}$. The first one $\mathbf{p}_{0,4}$ has four separated defects and is defined by projecting the cartesian basis vector \mathbf{e}_y into the tangent space of each point $\mathbf{x} \in \mathcal{S}$, while the second initial value has two defects, $\mathbf{p}_{0,2}$ analogous defined by the projecting \mathbf{e}_x . A survey of suitable numerical methods solving the dynamic equations is given in [54]. Within this setup we evaluate the energy for stationary solutions \mathbf{p}^* and the number of defects for both initial solutions $\mathbf{p}_{0,4/2}$ for a sequence of values $C \in [0, 1.5]$.

An example of the two different initial fields relaxed to equilibrium is shown in figure 3.6 for a nonic surface with $C = 1.175$. We find defects with topological charge $+1$ at maxima of the Gaussian curvature, while a defects with charge -1 may appear at the saddle point. This dependency is in agreement with results for the similar problem of flow on curved surfaces [65, 58]. For shapes with $C \in [0.5, 0.635]$, we observe that both initial solutions converge to a two-defect configuration. In figure 3.7-(right) we plot the fusion time for defect annihilation of initial condition $\mathbf{p}_{0,4}$. Notice the steep increase in this time for $C \uparrow 0.635$. For $C > 0.635$ a four-defect configuration becomes stable, thereby posing a local energetic minimum. Further increasing the parameter C , continuously amplifies the Gaussian curvature on the bulges and saddle. As shown in figure 3.7-(left),

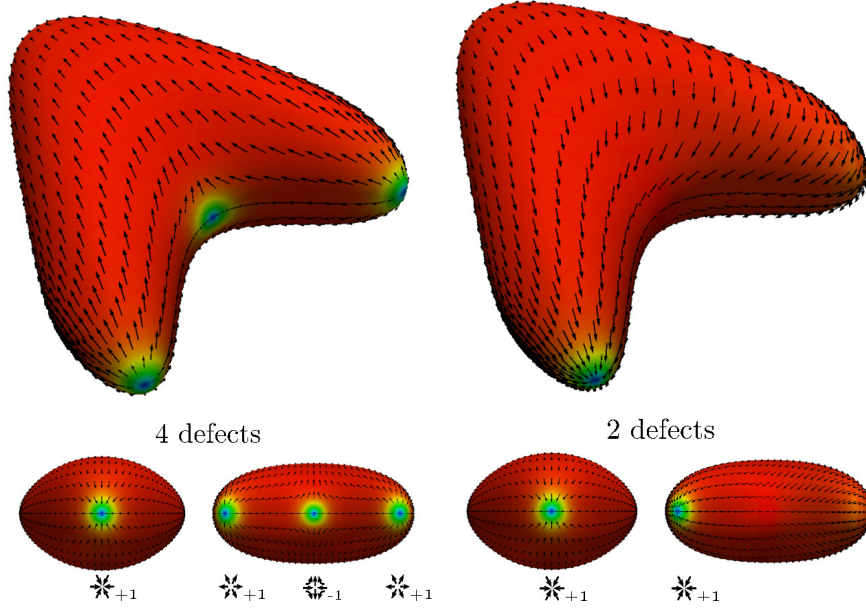


Figure 3.6: **Equilibrium states for surface with $C = 1.175$ with four and two defects:** norm defects (color gradient) and director (glyphs). Second row: back and front detail of configuration.

this leads to a decreasing energy cost for the four-defect stationary solution, while costs for the two-defect solution increase monotonically until the energies are equal at $C \approx 1.175$. For $C > 1.175$ the four-defect solution becomes energetically favorable.

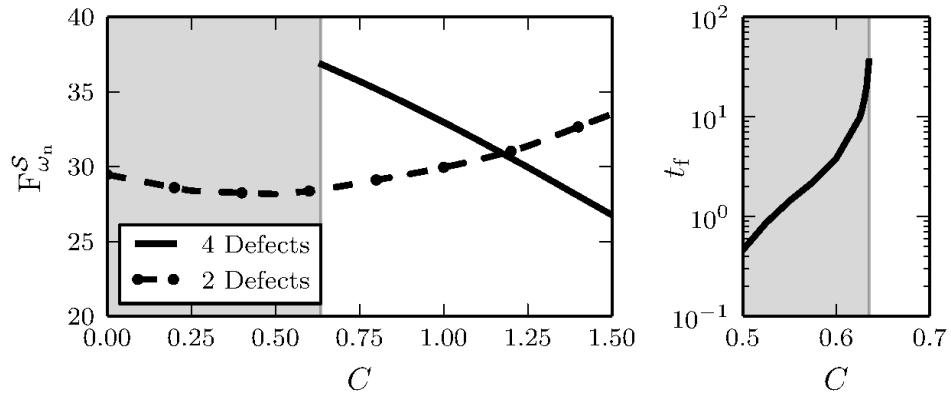


Figure 3.7: **Energy of equilibrium states for nonic shapes:** [left] energy $\mathcal{F}^S[\mathbf{p}^*]$ for solutions with four and two defects for nonic shapes with $C \in [0, 1.5]$ [right] and defect fusion time for the four-defect initial solution

These experiments emphasize the impact of curvature on the energetic cost of a defect configuration as well as their stability and proves the key role of domain geometry in existence of non-trivial realizations of the Poincaré-Hopf theorem.

3.2.4 Impact of System Size

To conclude our discussion of polar ordering in thin shells, we briefly review the thin shell limit surface energy under the aspect of domain size. For this purpose we use l as characteristic length scale given by the maximum edge length of a bounding box containing \mathcal{S} .

The curvature quantities \mathcal{H} , \mathcal{K} and \mathbf{B} scale by $\mathcal{O}(1/l^2)$ such that we yield for $\mathcal{F}_{el}^{\mathcal{S}}$

$$\mathcal{F}_{el}^{\mathcal{S}}(\mathbf{p}) = \frac{K}{2} \int_{\mathcal{S}} \underbrace{(\operatorname{div}_{\mathcal{S}} \mathbf{p})^2}_{\approx \mathcal{O}(1/l^2)} + \underbrace{(\operatorname{rot}_{\mathcal{S}} \mathbf{p})^2}_{\approx \mathcal{O}(1/l^2)} + \underbrace{\|\mathbf{B} \cdot \mathbf{p}\|^2}_{\approx \mathcal{O}(1/l^4)} \underbrace{d\mathcal{S}}_{\approx \mathcal{O}(l^2)} \approx K\mathcal{O}(1) + K\mathcal{O}(1/l^2) \quad (3.59)$$

For the thermotropic energy $\mathcal{F}_{th}^{\mathcal{S}}$ we observe

$$\mathcal{F}_{th}^{\mathcal{S}}(\mathbf{p}) = \frac{\omega_n}{4} \int_{\mathcal{S}} \underbrace{(\|\mathbf{p}\|^2 - 1)^2}_{\approx \mathcal{O}(1)} \underbrace{d\mathcal{S}}_{\approx \mathcal{O}(r_c^2)} \approx \omega_n \mathcal{O}(r_c^2) \quad (3.60)$$

where r_c denotes the radius of defect core. For numeric investigations concerning the relation of ω_n and r_c , we consider a flat disc with a single source type defect enforced by boundary conditions. Varying ω_n and defining regions with $\|\mathbf{p}\| < 0.9$ as defect core we obtain a relation of $r_c^2 = 1/\omega_n$. Assuming this holds also for curved space we yield for thermotropic energy $\mathcal{F}_{th}^{\mathcal{S}}(\mathbf{p}) \approx \mathcal{O}(1)$.

Therefore, we observe the intrinsic elastic energy and thermotropic potential are invariant under rescaling, relevant parameters determining the fundamental dynamics are K and the defect core radius r_c , defined by ω_n . Quite contrary the extrinsic energy contributions scale by $\mathcal{O}(1/l^2)$ and increase their impact for small systems $l \ll 1$.

3.3 Q tensors in Thin Shells

After considering equilibria of polar ordered systems we now turn to ordered systems with constituents exhibiting a head-tail symmetry. The most prominent modeling of such systems is the Landau-de Gennes model [79].

We will open this section by reviewing this model in the volume and discuss possible strategies for defining surface bound Q tensors. Subsequently, we will generalize our previous notion of thin shell limit and apply it to obtain a Landau-de Gennes model on surfaces, preserving the key features of the volume model. For this surface model we present results of numerical experiments eluding the interplay of curvature and nematic ordering. We conclude the section by discussing the scaling behavior of the surface model under change of system size.

3.3.1 The Landau - de Gennes Model in Volume and on Surfaces

The Landau-de Gennes model, also known as Q tensor model, considers aggregations of rod or disc like particles. These systems are described on an ensemble average level by using a vector valued principal director \mathbf{P} ($\|\mathbf{P}\| = 1$) and a scalar order parameter S . \mathbf{P} describes the average orientation

of the long body axis (rods) or the normal (discs) and S characterizes the deviation of individual molecules from \mathbf{P} . Generally speaking, the average ordering of such an ensemble can be classified in three phases: $S = 0$ isotropic, implying an uniform distribution of particle directions, $S > 0$ nematic phase where particles are aligned in direction of \mathbf{P} and $S < 0$ where particles are aligned orthogonal to \mathbf{P} . Due to this dual nature (ordered and isotropic) of this material these systems are often called liquid crystals.

Please note, the Q tensor model can also be used to describe systems consisting of many other types of particles. For example chiral particles (which can not be superimposed with their mirror image) or particles without any rotational symmetry, as present in rods or discs. Nonetheless we will focus on systems consisting of achiral particles with a rotational symmetry, such liquid crystals we will call uniaxial.

The Q tensor From the macroscopic state variables \mathbf{P} (the principal director, a normalized vector) and S (order parameter) we can define the Q tensor by

$$\mathbf{Q} = S \left(\mathbf{P}\mathbf{P} - \frac{1}{3}\mathbf{G} \right) \quad (3.61)$$

This second order tensor is symmetric and trace free, further it's eigenvalue spectrum is given by $[2/3S, -1/3S, -1/3S]$. The principal eigenvector \mathbf{P} corresponds to the dominant eigenvalue $2/3S$. Any vector \mathbf{V} orthogonal to \mathbf{P} is therefore an eigenvector corresponding to $-1/3S$, such that the rotational symmetry of the rod/disc-like particles is also represented in the Q tensor. We define square norm for second order tensors by

$$\|\mathbf{Q}\|^2 = Q_{IJ}Q^{IJ} = \text{tr}(\mathbf{Q}^2) = \frac{2}{3}S^2 \quad (3.62)$$

Elastic and thermotropic energy Given a field of Q tensors in a domain $V \subset \mathbb{R}^3$ with flat coordinates the Landau-de Gennes model uses an elastic and thermotropic energy to define a ground state with uniform parallel ordering and a preferred degree of ordering S^* . The elastic energy reads

$$\begin{aligned} \mathcal{F}_{el}^V(\mathbf{Q}) = & \frac{1}{2} \int_V L_1 \partial_K Q_{IJ} \partial^K Q^{IJ} + L_2 \partial_J Q_I^J \partial^K Q^I_K + L_3 \partial_J Q_I^K \partial_K Q^{IJ} \, dV \\ & + \frac{1}{2} \int_V L_4 E_{LIK} Q^{LJ} \partial^K Q^I_J + L_6 Q^{LK} \partial_L Q_{IJ} \partial_K Q^{IJ} \, dV \end{aligned} \quad (3.63)$$

This model can be understood as an approximation, of an actually unknown, energy functional by a first order expansion in \mathbf{Q} and $\nabla\mathbf{Q}$. In this setting the terms associated L_1 to L_6 represent the first order terms invariant under rotation, the elastic coefficients L_i are phenomenological and have to be determined by experiments. Using an one constant approximation for the elastic constants in the Frank-Oseen ($K = K_1 = K_2 = K_3$) and Landau-de Gennes energy ($L_1 = L, L_2 = L_3 = L_6 = 0$) the elastic energy functionals of both model coincide for defect free configurations and $K = 2L \text{tr}(\mathbf{Q}^2)$ [71].

In our further considerations we will neglect the L_4 term since it vanishes for achiral liquid

crystals. For the L_6 term it has been shown that \mathbf{Q} tensor fields \mathbf{Q} can be constructed such that $\mathcal{F}_{el}^V(\mathbf{Q}) \searrow -\infty$ leading to an ill posed problem [7]. For sake of readability, we avoid the proposed correction of this term and also ignore the L_6 term in further discussion.

For the thermotropic state potential a polynomial expansion with minimal degree is used to approximate the regime close to the isotropic-nematic phase transition. The coefficients of such expansion A, B and C are phenomenological [84].

$$\begin{aligned}\mathcal{F}_{th}^V(\mathbf{Q}) &= \int_V A \operatorname{tr}(\mathbf{Q}^2) + \frac{2B}{3} \operatorname{tr}(\mathbf{Q}^3) + \frac{C}{2} \operatorname{tr}(\mathbf{Q}^2)^2 dV \\ &= \omega_n \int_V a \operatorname{tr}(\mathbf{Q}^2) + \frac{2b}{3} \operatorname{tr}(\mathbf{Q}^3) + \frac{c}{2} \operatorname{tr}(\mathbf{Q}^2)^2 dV\end{aligned}\quad (3.64)$$

Further, A is usually considered a temperature depended coefficient to model the first order transition from pure isotropic phase, via coexistence, to pure nematic phase, see figure 3.8. Anyway, we will focus on isothermal systems and neglect this temperature dependence and consider only systems with A fixed.

To enable qualitative statements comparing the impact of elastic and thermotropic contributions we define rescaled coefficients by $a = A/\omega_n, b = B/\omega_n, c = C/\omega_n$ such that a, b, c match the order of magnitude of L_i .

The minima of the thermotropic energy can be expressed in terms of order parameter S for any given parameter set a, b, c , considering the thermotropic energy density

$$f_{th}^V(S) = \frac{2\omega_n}{27} (9aS^2 + 2bS^3 + 3cS^4) \quad (3.65)$$

$$\partial_S f_{th}^V(S^*) = 0 \Leftrightarrow S^* = 0 \text{ or } S^* = \frac{1}{4c} \left(-b \pm \sqrt{b^2 - 24ac} \right) \quad (3.66)$$

Reviewing $\partial_S^2 f_{th}^V(S^*)$ we obtain the phase portrait w.r.t. the choice of a, b, c , see figure 3.8.

Surface \mathbf{Q} tensor modeling by dimensional reduction The considered thin shells of uniaxial liquid crystals are usually combined with the assumption of tangential aligned particles. Also the thin shell models aim to derive an effective model with reduced dimensionality. Two models for tangential \mathbf{Q} tensors on surfaces are discussed in this section.

The first approach has been labeled as planar degenerate \mathbf{Q} tensors and is used e.g. in [37]. Such modeling starts with defining the \mathbf{Q} tensors in the vanishing thickness limit of a flat thin shell. In the resulting flat 2D geometry, with a metric equivalent to the 2D identity \mathbb{I}_2 , symmetric trace free tensors are described by

$$\mathbf{q} = S \left(\mathbf{P}\mathbf{P} - \frac{1}{2}\mathbb{I}_2 \right) \text{ where } \mathbf{P} \cdot \boldsymbol{\nu} = 0, \quad (3.67)$$

where we have required the principal director to be in plane. This model is then transferred straight

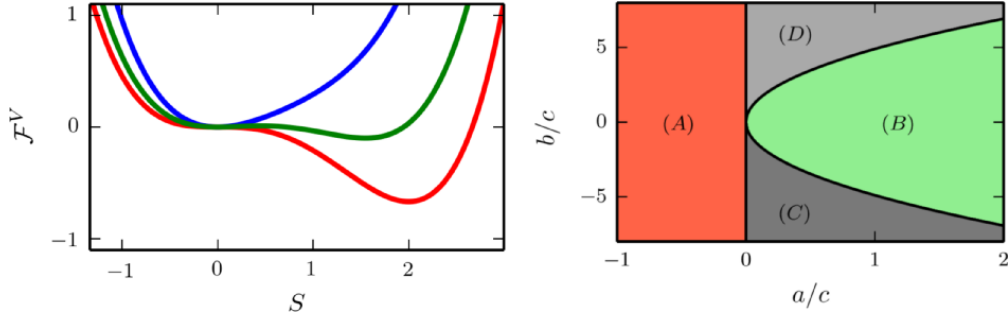


Figure 3.8: **Properties of the thermotropic state potential:** [left] Energy cost versus order parameter for $b = -1/2$, $c = 1/4$ and several values of a across nematic-isotropic transition. $a = 0$, only ordered state with $S^* > 0$ is stable (red line), $a = 0.35$ stable minima at $S^* = 0$ and $S^* > 0$ enabling coexistence of isotropic and ordered phase (green line) and $a = 1$ where $S^* = 0$, only isotropic phase is stable (blue line) [right] phase portrait w.r.t. to ratios of a, b, c (A): stable nematic ordering $S^* \neq 0$, (B): stable isotropic ordering $S^* = 0$, (C): only tangential nematic ordering is stable, $S^* > 0$ or (D): only normal nematic ordering is stable, $S^* < 0$

forward to curved domains by using the associated curved space metric instead of \mathbb{I}_2 and yields

$$q_{ij} = S \left(P_i P_j - \frac{1}{2} g_{ij} \right) \quad \text{or} \quad q_{IJ} = S \left(P_I P_J - \frac{1}{2} (\nu_I \nu_J - \delta_{IJ}) \right) \quad (3.68)$$

Such modeling implies a tangentiality for surface Q tensors in the sense of a zero eigenvalue in normal direction $\mathbf{q} \cdot \boldsymbol{\nu} = 0$. Further \mathbf{q} is symmetric and trace free w.r.t. the surface trace notion, in the sense $\text{tr}_S(\mathbf{q}) = \mathbf{g} : \mathbf{q}$.

The eigenvalue spectra reads therefore $[1/2s, -1/2s, 0]$, which can be interpreted as a global symmetry under rotations of 90° in tangential plane. This eigenvalue spectrum also implies $\text{tr}_S(\mathbf{q}^3) = 0$, such that the cubic term in the thermotropic potential vanishes. In this case, the coexistence of ordered and isotropic state is no longer admissible in the surface model.

The second approach, described by [53], interprets tangentiality of a surface bound Q tensor as a zero eigenvalue of the second moment tensor of the microscopic particle distribution such that

$$\mathbf{M} = \mathbf{P}\mathbf{P} \quad \text{where} \quad \mathbf{M} \cdot \boldsymbol{\nu} = 0 \quad (3.69)$$

This argument is independent from the spatial dimension of the domain and enables us to obtain the previous model (3.67) in the 2D case but also a 3 dimensional Q tensor analog to (3.61)

$$\hat{\mathbf{Q}} = S \left(\mathbf{P}\mathbf{P} - \frac{1}{3} \mathbf{G} \right) \quad \text{where} \quad \mathbf{P} \cdot \boldsymbol{\nu} = 0 \quad (3.70)$$

Contrary to the first approach, here the eigenvalue in normal direction is $\hat{\mathbf{Q}} \cdot \boldsymbol{\nu} = -\frac{1}{3} S \boldsymbol{\nu}$. Therefore, the eigenvalue spectra of the tangential Q tensor $\hat{\mathbf{Q}}$ is identical to the volume formulation \mathbf{Q} and contains a rotational symmetry around the principal director \mathbf{P} . $\hat{\mathbf{Q}}$ is symmetric and trace free w.r.t. the embedding space metric $\text{tr}(\hat{\mathbf{Q}}) = \mathbf{G} : \hat{\mathbf{Q}}$.

Denoting the eigenvalue of $\hat{\mathbf{Q}}$ in normal direction by $\beta = \boldsymbol{\nu} \cdot \hat{\mathbf{Q}} \cdot \boldsymbol{\nu}$, the formulations for tangential tensors can be related by $\hat{\mathbf{Q}}(\mathbf{q}, \beta) = \mathbf{q} - \beta/2 \mathbf{g} + \beta \boldsymbol{\nu} \boldsymbol{\nu}$. In this sense we call \mathbf{q} tangential and β normal part of $\hat{\mathbf{Q}}$. Considering $\beta = 0$ we observe $\hat{\mathbf{Q}}$ to be identical with the degenerate surface \mathbf{Q} tensor \mathbf{q} .

3.3.2 Generalized Thin Shell Limit

In the case of polar ordering we assumed orientational order with no variation in normal direction of the thin shell. Here we want to drop this assumption and model the thin shell as an actual thin volume with boundaries in the normal direction, subsequently allowing variations in normal direction.

To obtain an effective surface model, we discuss a suitable set of boundary conditions for the thin shell domain, establish a description of volume \mathbf{Q} tensor \mathbf{Q} in terms of tangential and normal contributions. Finally we perform the limit of vanishing thickness h to obtain the surface model and consistent equations of motion. While doing so we focus on the conceptual part of this modeling and refer for the technical details to [57].

To preserve readability we will derive the elastic contribution only for a fixed, spatial invariant β . We limit the arguments to thin shells \mathcal{S}_h , which can be considered as tubular extensions of surfaces \mathcal{S} , the presented arguments can be generalized to manifolds by little effort.

Expressing the thin shell model by surface quantities At the thin shell boundaries $\partial\mathcal{S}_h$, we apply the previously discussed tangentiality condition $\mathbf{Q} \cdot \boldsymbol{\nu} = \beta \boldsymbol{\nu}$. But this condition does not fix all degrees of freedom of \mathbf{Q} on $\partial\mathcal{S}_h$. For closure, we choose therefore natural boundary conditions for the remaining degrees of freedom, namely

$$0 = L_1 Q_{ij;\xi} + L_3 Q_{i\xi;j} \quad \text{or} \quad 0 = L_1 (\nabla \mathbf{Q}) \cdot \boldsymbol{\nu} + L_3 \nabla (\mathbf{Q} \cdot \boldsymbol{\nu}) \quad \text{on } \partial\mathcal{S}_h \quad (3.71)$$

These conditions can be interpreted as requiring the conjugate forces, $\mathbf{H} = -\partial f^V / \partial \mathbf{Q}$, to be tangential on the boundary. Alternatively, this boundary conditions can be motivated by the assumption that energy contribution of the thin shell boundaries should be neglectable compared to the energy contributions in the thin shell volume.

Due to the thin shell nature of the geometry, we can approximate the values of \mathbf{Q} and $\nabla \mathbf{Q}$ on the central surface $\mathcal{S} \subset \mathcal{S}_h$ by the surface tensor $\hat{\mathbf{Q}}(\mathbf{q}, \beta)$ and its associated covariant derivative $\nabla_{\mathcal{S}}$. Using a shorthand formulation $\sigma(\mathbf{q}) = \mathbf{q} - \beta/2 \mathbf{g}$ we obtain

$$\begin{aligned} Q_{\xi i}|_{\mathcal{S}} &= Q_{i\xi}|_{\mathcal{S}} = \mathcal{O}(h^2) \\ Q_{\xi\xi}|_{\mathcal{S}} &= \beta + \mathcal{O}(h^2) \\ Q_{ij}|_{\mathcal{S}} &= q_{ij} + \frac{\beta}{2} g_{ij} + \mathcal{O}(h^2) \end{aligned} \quad (3.72)$$

for the components and their derivatives

$$Q_{\xi\xi\xi}|_{\mathcal{S}} = Q_{i\xi\xi}|_{\mathcal{S}} = Q_{\xi i\xi}|_{\mathcal{S}} = \mathcal{O}(h^2) \quad (3.73)$$

$$Q_{\xi\xi;k}|_{\mathcal{S}} = [\sigma(\mathbf{q}) \mathbf{B}]_{ik} + \mathcal{O}(h^2) \quad (3.74)$$

$$Q_{ij;\xi}|_{\mathcal{S}} = -\frac{L_3}{L_1} [\sigma(\mathbf{q}) \mathbf{B}]_{ik} + \mathcal{O}(h^2) \quad (3.75)$$

$$Q_{ij;k}|_{\mathcal{S}} = q_{ij|k} + \mathcal{O}(h^2). \quad (3.76)$$

Inserting this description in the energy contributions of the Landau-de Gennes model, see equation (3.63),(3.64), allows to describe the thin shell energy in terms of the surface tensors \mathbf{q} and normal part β within the error bound of $\mathcal{O}(h^2)$. Terms of the thermotropic energy are expressed by

$$\text{tr}(\mathbf{Q}^2)|_{\mathcal{S}} = \text{tr}_{\mathcal{S}}(\mathbf{q}^2) + \frac{3}{2}\beta^2 + \mathcal{O}(h^2) \quad (3.77)$$

$$\text{tr}(\mathbf{Q}^3)|_{\mathcal{S}} = \frac{3}{2}\beta \left(\frac{\beta^2}{2} - \text{tr}_{\mathcal{S}}(\mathbf{q}^2) \right) + \mathcal{O}(h^2) \quad (3.78)$$

$$\text{tr}(\mathbf{Q}^4)|_{\mathcal{S}} = \text{tr}_{\mathcal{S}}(\mathbf{q}^4) + \frac{3}{2}\beta^2 \text{tr}_{\mathcal{S}}(\mathbf{q}^2) + \frac{9}{8}\beta^4 + \mathcal{O}(h^2). \quad (3.79)$$

Here we observe that the cubic term contains tangential contributions only in quadratic order such that for $\beta = 0$ this term indeed vanishes up to $\mathcal{O}(h^2)$ making β a crucial parameter for enabling coexistence of ordered and isotropic phases in the model. For the terms of the elastic energy we yield

$$L_1 \|\nabla \mathbf{Q}\|_{\mathcal{S}}^2 + L_2 \|\text{div} \mathbf{Q}\|_{\mathcal{S}}^2 + L_3 \left\langle \nabla \mathbf{Q}, (\nabla \mathbf{Q})^{T(23)} \right\rangle_{\mathcal{S}} \quad (3.80)$$

$$= L_1 \|\nabla_{\mathcal{S}} \mathbf{q}\|_{\mathcal{S}}^2 + L_2 \|\text{div}_{\mathcal{S}} \mathbf{q}\|_{\mathcal{S}}^2 + L_3 \left\langle \nabla_{\mathcal{S}} \mathbf{q}, (\nabla_{\mathcal{S}} \mathbf{q})^{T(23)} \right\rangle_{\mathcal{S}} \quad (3.81)$$

$$+ \left(2L_1 - \frac{L_3^2}{L_1} \right) \|\sigma_3(\mathbf{q}) \mathbf{B}\|_{\mathcal{S}}^2 + L_2 (\text{tr}_{\mathcal{S}}(\sigma(\mathbf{q}) \mathbf{B}))^2 + L_3 \text{tr}_{\mathcal{S}}((\sigma(\mathbf{q}) \mathbf{B})^2) + \mathcal{O}(h^2). \quad (3.82)$$

In this operator formulation we have equipped the transpose operator with additional indices to clarify the transposed components, $[(\nabla \mathbf{Q})^{T(23)}]_{ijk} = [\nabla \mathbf{Q}]_{ikj}$. We observe matching terms in surface description plus a set of terms coupling \mathbf{q} to the surface curvature quantities.

$$(\text{tr}_{\mathcal{S}}(\sigma_3(\mathbf{q}) \mathbf{B}))^2 = \langle \mathbf{B}, \mathbf{q} \rangle^2 - 3\beta \mathcal{H} \langle \mathbf{B}, \mathbf{q} \rangle + \frac{9}{4}\beta^2 \mathcal{H}^2 \quad (3.83)$$

$$\text{tr}_{\mathcal{S}}((\sigma_3(\mathbf{q}) \mathbf{B})^2) = \langle \mathbf{B}, \mathbf{q} \rangle^2 + \mathcal{K} \text{tr}_{\mathcal{S}}(\mathbf{q}^2) - 3\beta \mathcal{H} \langle \mathbf{B}, \mathbf{q} \rangle + \frac{9}{4}\beta^2 (\mathcal{H}^2 - 2\mathcal{K}) \quad (3.84)$$

$$\|\sigma_3(\mathbf{q}) \mathbf{B}\|_{\mathcal{S}}^2 = \frac{1}{2} (\mathcal{H}^2 - 2\mathcal{K}) \text{tr}_{\mathcal{S}}(\mathbf{q}^2) - 3\beta \mathcal{H} \langle \mathbf{B}, \mathbf{q} \rangle + \frac{9}{4}\beta^2 (\mathcal{H}^2 - 2\mathcal{K}) \quad (3.85)$$

Considering these terms in detail, we can group them in three categories: an explicit coupling of curvature to the norm of \mathbf{q} , a coupling by contraction of \mathbf{q} with the shape operator \mathbf{B} and β as well as a explicit coupling of β and the curvatures of \mathcal{S} . Again the parameter β plays a crucial role since most of these coupling terms vanish for $\beta = 0$.

Before summing up these results we review a result concerning the first order invariants of $\nabla_{\mathcal{S}} \mathbf{q}$

on surfaces presented in [57]

$$\int_{\mathcal{S}} \|\operatorname{div}_{\mathcal{S}} \mathbf{q}\|^2 \, d\mathcal{S} = \int_{\mathcal{S}} \frac{1}{2} \|\nabla_{\mathcal{S}} \mathbf{q}\|^2 + \mathcal{K} \operatorname{tr}_{\mathcal{S}}(\mathbf{q}^2) \, d\mathcal{S}, \quad (3.86)$$

$$\int_{\mathcal{S}} \left\langle \nabla_{\mathcal{S}} \mathbf{q}, (\nabla_{\mathcal{S}} \mathbf{q})^{T(23)} \right\rangle \, d\mathcal{S} = \int_{\mathcal{S}} \frac{1}{2} \|\nabla_{\mathcal{S}} \mathbf{q}\|^2 - \mathcal{K} \operatorname{tr}_{\mathcal{S}}(\mathbf{q}^2) \, d\mathcal{S}. \quad (3.87)$$

Using these expressions, we can define a surface Landau-de Gennes energy and express it along the surface Q tensor $\hat{\mathbf{Q}}(\mathbf{q}, \beta)$, as defined in equation (3.70), by

$$\mathcal{F}_{el}^{\mathcal{S}}(\mathbf{q}, \beta) = \frac{1}{2} \int_{\mathcal{S}} L'_1 \|\nabla_{\mathcal{S}} \mathbf{q}\|_{\mathcal{S}}^2 + M_1 \operatorname{tr}_{\mathcal{S}}(\mathbf{q}^2) + M_2 \langle \mathcal{B}, \mathbf{q} \rangle^2 + M_4(\beta) \langle \mathcal{B}, \mathbf{q} \rangle + C_e(\beta) \, d\mathcal{S} \quad (3.88)$$

$$\mathcal{F}_{th}^{\mathcal{S}}(\mathbf{q}, \beta) = \omega_n \int_{\mathcal{S}} a'(\beta) \operatorname{tr}_{\mathcal{S}}(\mathbf{q}^2) + \frac{c}{2} \operatorname{tr}_{\mathcal{S}}(\mathbf{q}^2)^2 + C_t(\beta) \, d\mathcal{S} \quad (3.89)$$

with coefficient functions for elastic

$$L'_1 = L_1 + \frac{1}{2} (L_2 + L_3) \quad (3.90)$$

$$M_1 = \frac{1}{2} \left(\left(2L_1 - \frac{L_3^2}{L_1} \right) (\mathcal{H}^2 - 2\mathcal{K}) + (L_2 + L_3) \mathcal{K} \right) \quad (3.91)$$

$$M_2 = (L_2 + L_3) \quad (3.92)$$

$$M_4(\beta) = -3 \left(2L_1 + L_2 + L_3 - \frac{L_3^2}{L_1} \right) \beta \mathcal{H} \quad (3.93)$$

and thermotropic contributions

$$a'(\beta) = \frac{1}{2} (2a - 2b\beta + 3c\beta^2) \quad (3.94)$$

$$C_e(\beta) = \frac{9}{4} \left(\left(2L_1 + L_3 - \frac{L_3^2}{L_1} \right) (\mathcal{H}^2 - 2\mathcal{K}) + L_2 \mathcal{H}^2 \right) \beta^2 \quad (3.95)$$

$$C_t(\beta) = \frac{\beta^2}{8} (12a + 4b\beta + 9c\beta^2). \quad (3.96)$$

Thin shell limit and equations of motion To establish the relation of Landau-de Gennes energy $\mathcal{F}^{\mathcal{S}_h}(\mathbf{Q})$ with the derived surface energy $\mathcal{F}^{\mathcal{S}}(\mathbf{q}, \beta) = \mathcal{F}_{el}^{\mathcal{S}}(\mathbf{q}, \beta) + \mathcal{F}_{th}^{\mathcal{S}}(\mathbf{q}, \beta)$ we consider, as in the case of polar ordering, the averaged thin shell energy

$$\mathcal{F}^{\mathcal{S}}(\mathbf{Q}, h) = \frac{1}{h} \mathcal{F}^{\mathcal{S}_h}(\mathbf{Q}) = \frac{1}{h} \int_{\mathcal{S}_h} f^{\mathcal{S}_h} \, d\mathcal{S}_h \quad (3.97)$$

Splitting now the integration in normal and surface parts of the thin shell, using a split volume element $d\mathcal{S}_h = (1 - \xi\mathcal{H} + \xi^2\mathcal{K}) \, d\xi \, d\mathcal{S}$ [57], as well as inserting the description in surface Q tensors

of (3.80) we yield

$$\begin{aligned}\mathcal{F}^{\mathcal{S}}(\mathbf{Q}, h) &= \frac{1}{h} \int_{-\frac{h}{2}}^{\frac{h}{2}} \int_{\mathcal{S}} (1 - \xi \mathcal{H} + \xi^2 \mathcal{K}) f^{\mathcal{S}h} \, d\mathcal{S} d\xi = \int_{\mathcal{S}} f^{\mathcal{S}} \, d\mathcal{S} + \mathcal{O}(h^2) \\ &= \mathcal{F}^{\mathcal{S}}(\mathbf{q}, \beta) + \mathcal{O}(h^2) \longrightarrow \mathcal{F}^{\mathcal{S}}(\mathbf{q}, \beta)\end{aligned}\quad (3.98)$$

The surface L^2 -gradient flow is given by

$$\int_{\mathcal{S}} \langle \partial_t \mathbf{q}, \boldsymbol{\psi} \rangle \, d\mathcal{S} = - \int_{\mathcal{S}} \left\langle \frac{\partial f^{\mathcal{S}}}{\partial \mathbf{q}}, \boldsymbol{\psi} \right\rangle \, d\mathcal{S}, \quad \forall \boldsymbol{\psi} \in \mathcal{Q}(\mathcal{S}), \quad (3.99)$$

w.r.t. the L^2 inner product over the space of Q-tensors, but to obtain the strong formulation we have to ensure that $\partial f^{\mathcal{S}}/\partial \mathbf{q} \in \mathcal{Q}(\mathcal{S})$. Considering the derivative of the M_2 and M_4 term in (3.88) we observe them to be not trace free, namely

$$\text{tr}([2M_2\langle \mathcal{B}, \mathbf{q} \rangle + M_4(\beta)] \mathcal{B}) = [2M_2\langle \mathcal{B}, \mathbf{q} \rangle + M_4(\beta)] \mathcal{H}. \quad (3.100)$$

Therefore we will only consider the trace free part of \mathcal{B} . Further, defining $\text{div}_{\mathcal{S}} \nabla_{\mathcal{S}} \mathbf{q} = \boldsymbol{\Delta}_{\mathcal{S}}^{dG} \mathbf{q}$ as the div-Grad (Bochner) Laplace operator, the equations of motion, for the tangential part of $\hat{\mathbf{Q}}$, reads

$$\begin{aligned}\partial_t \mathbf{q} &= L_1' \boldsymbol{\Delta}_{\mathcal{S}}^{dG} \mathbf{q} - M_1 \mathbf{q} - \left(M_2 \langle \mathcal{B}, \mathbf{q} \rangle + \frac{M_4}{2} \right) \left(\mathcal{B} - \frac{1}{2} \mathcal{H} \mathbf{g} \right) \\ &\quad - (2a' + 2c \, \text{tr}_{\mathcal{S}}(\mathbf{q}^2)) \mathbf{q}\end{aligned}\quad (3.101)$$

Initial values for this surface model are obtained by restricting \mathbf{Q}_0 to the surface and projecting its tangential part into $\mathcal{Q}(\mathcal{S})$ by a suitable projection $\Pi_{\mathcal{Q}}$

$$\mathbf{q}_0 = \Pi_{\mathcal{Q}} [\Pi_{\mathcal{S}}[\mathbf{Q}_0|_{\mathcal{S}}]] \quad (3.102)$$

Consistency of the surface model To conclude this section, we present two remarkable results of [57]. The first one concerns the description of the averaged gradient flow of the Landau-de Gennes energy by the gradient flow of the the surface energy

$$\frac{1}{h} \int_{\mathcal{S}_h} \left\langle \frac{\partial f^{\mathcal{S}_h}(\mathbf{Q})}{\partial \mathbf{Q}} + \partial_t \mathbf{Q}, \boldsymbol{\Psi} \right\rangle \, d\mathcal{S}_h = \int_{\mathcal{S}} \left\langle \frac{\partial f^{\mathcal{S}}(\mathbf{q}, \beta)}{\partial \mathbf{q}} + \partial_t \mathbf{q}, \boldsymbol{\psi} \right\rangle \, d\mathcal{S} + \mathcal{O}(h^2), \quad (3.103)$$

while the second result refers to a point wise approximation of the equations of motion derived from the Landau-de Gennes and the surface energy.

$$\| \Pi_{\mathcal{Q}} [\Pi \cdot (\partial_t \mathbf{Q} + \delta \mathcal{F}^{\mathcal{S}_h}(\mathbf{Q}))|_{\mathcal{S}} \cdot \Pi] - (\partial_t \mathbf{q} + \delta \mathcal{F}^{\mathcal{S}}(\mathbf{q}, \beta)) \|_{\mathbf{g}} = \mathcal{O}(h^2) \quad (3.104)$$

Together, these results ensure that also the approach of first considering the averaged gradient flow of the volume Landau-de Gennes energy and performing the thin shell limit afterwards also yields

the surface model. Or more formal speaking the following operator diagram

$$\begin{array}{ccc}
 \mathcal{F}^{\mathcal{S}_h} & \xrightarrow[\frac{1}{h}]{h \rightarrow 0} & \mathcal{F}^{\mathcal{S}} \\
 \delta \downarrow & & \downarrow \delta \\
 \partial_t \mathbf{Q} = -\delta \mathcal{F}^{\mathcal{S}_h}(\mathbf{Q}) & \xrightarrow[\Pi_{\mathcal{Q}, \Pi_{\mathcal{S}}}]{{h \rightarrow 0}} & \partial_t \mathbf{q} = -\delta \mathcal{F}^{\mathcal{S}}(\mathbf{q})
 \end{array} \tag{3.105}$$

commutes. This structural result underscores the consistency of the derived surface model of energy $\mathcal{F}^{\mathcal{S}}(\mathbf{q}, \beta)$ and equations of motion $\partial_t \mathbf{q} + \delta \mathcal{F}^{\mathcal{S}}(\mathbf{q}) = 0$.

3.3.3 Coupling Mechanisms of Geometry and Ordering in the Effective Surface Q Tensor Model

In this section we will discuss the interplay of the derived surface model and curvature by performing numerical experiments. Further, we will highlight the impact of choosing either degenerate ($\beta = 0$) or non-degenerate ($\beta \neq 0$) Q tensors in the surface model. To focus here on the principal effects we use a set of phenomenological parameter for the Landau-de Gennes energy such that the amount of energy contributions is limited. Namely $L_1 = L_2 = -L_3 = L$ for the elastic energy and $a = -2/3$, $b = -1/2$, $c = 1$ in the thermotropic potential.

For the evaluation of numerical experiments we used a numerical scheme basing on a componentwise FEM for a triangular approximation of the considered surface, for details see [55].

Surface model for degenerate surface Q tensors As starting point, we will review the surface model for degenerate Q tensors with $\beta = 0$. The associated free energy reads

$$\mathcal{F}^{\mathcal{S}}(\mathbf{q}, 0) = \frac{1}{2} \int_{\mathcal{S}} L \|\nabla_{\mathcal{S}} \mathbf{q}\|_{\mathcal{S}}^2 + \frac{L}{2} (\mathcal{H}^2 - 2\mathcal{K}) \text{tr}_{\mathcal{S}}(\mathbf{q}^2) \, d\mathcal{S} + \omega_n \int_{\mathcal{S}} a \text{tr}_{\mathcal{S}}(\mathbf{q}^2) + \frac{c}{2} \text{tr}_{\mathcal{S}}(\mathbf{q}^2)^2 \, d\mathcal{S} \tag{3.106}$$

and consists of a typical elastic contribution, a thermotropic potential of double well type and a zero order term coupling curvature of \mathcal{S} with the norm of \mathbf{q} .

As in the case of polar orientation we can interpret this coupling as a, geometry induced, local deformation of the thermotropic potential changing the preferred order parameter S^* , namely

$$S^* = \sqrt{3 \left(1 - \frac{L \|\mathcal{B}\|_{\mathcal{S}}^2}{4 \omega_n} \right)} \quad \text{or} \quad \|\mathbf{q}^*\|^2 = 2 \left(1 - \frac{L \|\mathcal{B}\|_{\mathcal{S}}^2}{4 \omega_n} \right) \tag{3.107}$$

Contrary to the polar case, see figure 3.4, where only areas with negative Gaussian curvature induced a local melt we observe here, that any deviations from a flat geometry can induce a local melt. So, while the thermotropic potential itself inhibits isotropic-nematic phase coexistence, a global phase coexistence can emerge on surfaces by local variance of geometric properties, as shown in figure 3.9. In numerical experiments we considered a sequence of ellipsoids, ordered by the value of the major axis B , ranging from prolate $B < 1$ via sphere $B = 1$ to oblate $B > 1$ geometries.

Using the four defect configuration on a sphere, with circular shaped regions of broken order, as

reference we observe two major effects. For the prolate geometries we observe that pairs of defects are attracted to the long poles of the ellipsoid such that the distance between them is significantly reduced, see also [37]. Second the defects are asymmetrically deformed towards the poles leading, for further decreased B , to an effective fusion of the defect pairs. As figure 3.9 shows, the resulting area of isotropic ordering is enlarged compared to the spherical geometry.

This effect is also present in the oblate case. Here the strong curvature is concentrated in the "rim" of the geometry, leading to heavy deformations of the defect shapes parallel to the rim. For sufficient large B , the elongated defects merge, forming a line defect separating the quasi flat domains of the upper and lower half.

Summing up, the geometry distorts the defects such that eventually defects unify and enlarged regions of broken order emerge. Further, the transition between these configuration is highly coupled to the local features of the considered geometries.

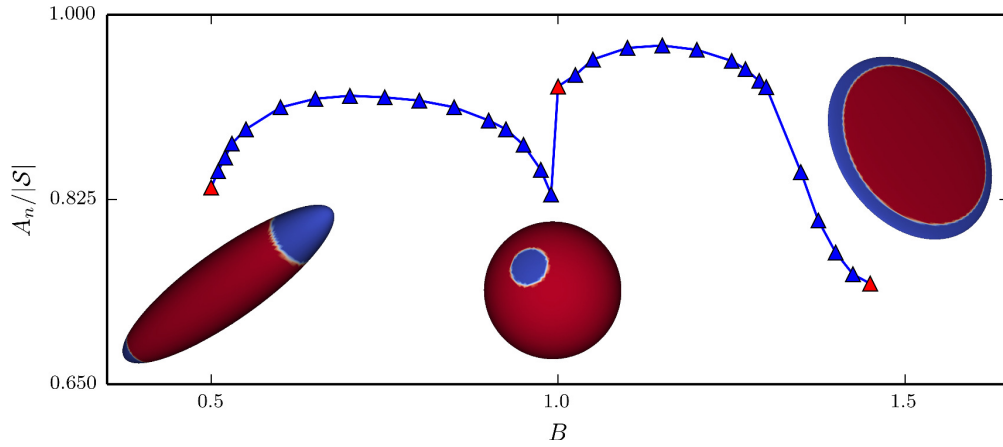


Figure 3.9: Curvature controls isotropic-nematic phase coexistence: Relative area of the nematic phase $A_n/|S|$ as a function of the geometry of the ellipsoid, parameterized by its axis B . For prolate ($B < 1.0$) the isotropic phases are located at the high curvature regions at the poles. They increase with increasing curvature for $B \lesssim 0.6$. For oblates ($B > 1.0$) the isotropic phase is located at the high curvature region along the rim. It increases with increasing curvature for $B \gtrsim 1.2$. The non-monotone behavior in between results from a rearrangement of two regions on a prolate to four regions on an oblate, which merge for larger B . The insets show realizations with red corresponding to the nematic and blue to the isotropic phase. The corresponding shape parameters are highlighted with red triangle markers. To distinguish between both phases a threshold of 10% of the expected norm of \mathbf{q} is used. We used $\omega_n = 2.5$ to highlight the behavior already for moderate curvatures.

Surface model for non-degenerate surface Q tensors Considering the model with constant $\beta \neq 0$ we have to specify the value of β . Here we propose an approach to choose β such that surface and thin shell formulation of the nematic energy match. For $\beta = -\frac{1}{3}S^*$, where $S^* = \frac{1}{4c}(-b + \sqrt{b^2 - 24ac})$, we yield indeed matching the minima of $\mathcal{F}_{\text{th}}^{S^*}$ and $\mathcal{F}_{\text{th}}^S$ which are achieved for $S = S^*$. The complete surface Q-tensor $\hat{\mathbf{Q}} = \mathbf{q} - \frac{\beta}{2}\mathbf{g} + \beta\nu\nu$ is then uniaxial with eigenvalues $[\frac{2}{3}S, -\frac{1}{3}S, -\frac{1}{3}S]$. Figure 3.10 shows the phase diagram. Contrary to the modeling via degenerate

states with $\beta = 0$, the phase diagram of the thermotropic energy is preserved for $\beta = -\frac{1}{3}S^*$.

Such parameter choice for β leads to an extended thermotropic potential and additional coupling terms in the elastic energy. The surface energy reads

$$\begin{aligned} \mathcal{F}^S(\mathbf{q}, -1/3S^*) &= \frac{1}{2} \int_S L \|\nabla_S \mathbf{q}\|_S^2 + \frac{L}{2} (\mathcal{H}^2 - 2\mathcal{K}) \text{tr}_S(\mathbf{q}^2) + S^* L \mathcal{H} \langle \mathcal{B}, \mathbf{q} \rangle + \frac{(S^*)^2}{4} L \mathcal{H}^2 \text{d}\mathcal{S} \\ &+ \omega_n \int_S a'(-1/3S^*) \text{tr}_S(\mathbf{q}^2) + \frac{c}{2} \text{tr}_S(\mathbf{q}^2)^2 + C_t(-1/3S^*) \text{d}\mathcal{S} \end{aligned} \quad (3.108)$$

The additional term $\langle \mathcal{B}, \mathbf{q} \rangle$ in the elastic energy imposes further restrictions on energetic favorable

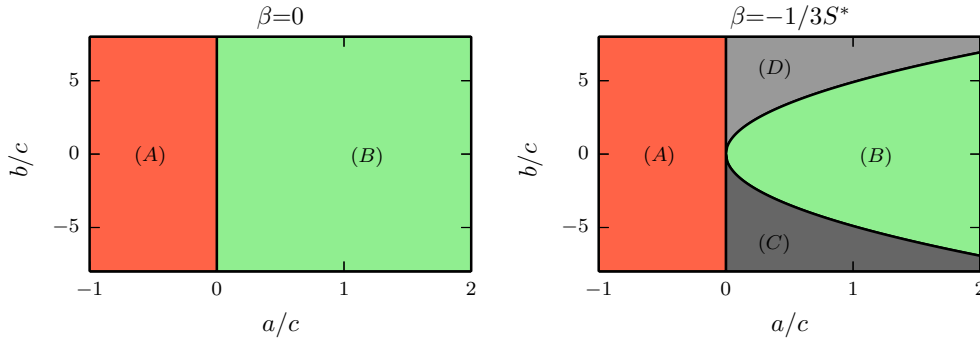


Figure 3.10: **Phase diagram of bulk energy vs choice of β** : (left) Double-well potential phase diagram for $\beta = 0$ exhibiting two domains enabling the existence of (A): stable nematic ordering $S^* \neq 0$ or (B): stable isotropic ordering $S^* = 0$. (right) Phase diagram for $\beta = -\frac{1}{3}S^*$ enabling additional stable phases discriminating between (C): only tangential nematic ordering is stable, $S^* > 0$ or (D): only normal nematic ordering is stable, $S^* < 0$.

ordering. Similar to the case of polar ordering this term can be expressed in terms of principal director $\mathbf{p} = \Pi_S[\mathbf{P}]$ of \mathbf{q} by $\langle \mathcal{B}, \mathbf{q} \rangle = \langle \mathcal{B} \cdot \mathbf{p}, \mathbf{p} \rangle - \frac{1}{2} \mathcal{H} \|\mathbf{p}\|$. These terms induce a geometric forcing towards the ordering along lines of minimal curvature. Such forcing does e.g. eliminate the invariance, under consistent rotation $R(\mathbf{p}, \Delta\theta)$ of the principal director, of the four $+\frac{1}{2}$ defect configuration on an ellipsoid as demonstrated in figure 3.11. The same effect has also been observed in surface Frank-Oseen model discussed in the previous section, see (3.55) and figure 3.3.

3.3.4 Impact of System Size

Reviewing the obtained thin shell limit of the elastic energy under the aspect of rescaling by a characteristic length l

$$\begin{aligned} \mathcal{F}_{el}^S(\mathbf{q}, \beta) &= \frac{1}{2} \int_S L_1 \underbrace{\|\nabla \mathbf{q}\|_S^2}_{\approx \mathcal{O}(1/l^2)} + L_2 \underbrace{\|\text{div} \mathbf{q}\|_S^2}_{\approx \mathcal{O}(1/l^2)} + L_3 \underbrace{\langle \nabla \mathbf{q}, (\nabla \mathbf{q})^{T(23)} \rangle_S}_{\approx \mathcal{O}(1/l^2)} \underbrace{\text{d}\mathcal{S}}_{\approx \mathcal{O}(l^2)} \\ &+ \frac{1}{2} \int_S \left(2L_1 - \frac{L_3^2}{L_1} \right) \underbrace{\|\sigma(\mathbf{q}) \mathcal{B}\|_S^2}_{\approx \mathcal{O}(1/l^4)} + L_2 \underbrace{(\text{tr}_S(\sigma(\mathbf{q}) \mathcal{B}))^2}_{\approx \mathcal{O}(1/l^4)} + L_3 \underbrace{\text{tr}_S((\sigma(\mathbf{q}) \mathcal{B})^2)}_{\approx \mathcal{O}(1/l^4)} \underbrace{\text{d}\mathcal{S}}_{\approx \mathcal{O}(l^2)} \end{aligned} \quad (3.109)$$

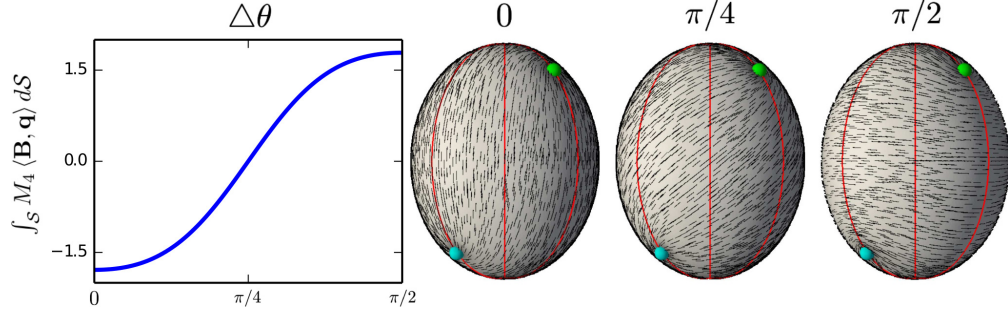


Figure 3.11: $\langle \mathbf{B}, \mathbf{q} \rangle$ term removes rotational invariance of elastic energy: (from left to right) Elastic energy contribution of $\int_S M_4 \langle \mathbf{B}, \mathbf{q} \rangle dS$ Q-tensor field \mathbf{q} for rotated principal eigenvectors $R(\mathbf{p}, \Delta\theta)$. Energetic minimum at $\Delta\theta = 0$ with director parallel to lines of minimal curvature (marked in red), increased energy at intermediate state at $\Delta\theta = \pi/4$ and maximal energy for director orthogonal to lines of minimal curvature at $\Delta\theta = \pi/2$. Energy contributions of L'_1 and M_1 are invariant under rotation and therefore constant.

we observe that the energy contributions of first order invariants of the tangential part of \mathbf{Q} scale by $\mathcal{O}(1)$ while the contributions of terms, coupling normal and tangential parts to the curvature, scale by $\mathcal{O}(1/l^2)$.

As discussed in the case of polar ordering the parameter ω_n influences the size of the defects. Due to the strong similarities in modeling of thermotropic energy in polar and nematic case we expect here also a relation of defect core radius r_c and ω_n of $r_c^2 = 1/\omega_n$. In this case, the thermotropic energy yields an approximate scaling by $\mathcal{O}(1)$. In agreement with the results for polar ordering, we observe strong impact of domain curvature for small geometries $l \ll 1$.

3.4 Active Polar Gels in Thin Shells

We will now use the generalized thin shell limit to obtain an effective model for active polar gels in thin shells. To avoid formal derivations, we present here only a sketch of the argumentation.

For the initial steps we reproduce the previous argumentations for the volume, transferred to the thin shell \mathcal{S}_h , up to the rate of dissipation given in (3.6). Contrary to the previous derivations we can not neglect the boundary terms of the dissipation rate by assuming a sufficient large distance.

$$\begin{aligned} \frac{d\mathcal{F}^{\mathcal{S}_h}}{dt} = & \int_{\mathcal{S}_h} -(\nabla\nabla) : \boldsymbol{\sigma}^{tot} + \Delta\mu r + \mathbf{J} \cdot \nabla\Delta\mu - \mathbf{H} \cdot \frac{D\mathbf{P}}{Dt} d\partial\mathcal{S}_h \\ & + \int_{\partial\mathcal{S}_h} \left[\mathbf{V} \cdot \boldsymbol{\sigma}^{tot} \cdot \boldsymbol{\nu} - \boldsymbol{\nu} \cdot \mathbf{V} \left(\frac{|\mathbf{M}|^2}{2\rho} + f_0 \right) - \Delta\mu \boldsymbol{\nu} \cdot \mathbf{J} + \boldsymbol{\nu} \cdot \frac{\partial f_0}{\partial \nabla \mathbf{P}} \cdot \frac{D\mathbf{P}}{Dt} \right] d\partial\mathcal{S}_h \quad (3.110) \end{aligned}$$

As in the case of nematic ordering, we stick with the idea that dissipation at the boundary should be neglectable compared to the thin shell contribution. We therefore determine suitable boundary conditions for the state variables such that the boundary terms vanish.

Following the previous assumptions of predominately tangential aligned particles on the thin

shell boundary we require $\mathbf{P} \cdot \boldsymbol{\nu} = 0$. For a thin shell of fixed shape we require $\mathbf{V} \cdot \boldsymbol{\nu} = 0$ on $\partial\mathcal{S}_h$ such that $\mathbf{V} (|\mathbf{M}|^2/2\rho + f_0)$ vanishes. Combined with Neumann type of boundary conditions for $\Delta\mu$ we obtain $\boldsymbol{\nu} \cdot \mathbf{J} = 0$. The requirement $\boldsymbol{\nu} \cdot \partial f_0 / \partial(\nabla\mathbf{P}) = 0$ is satisfied for a Neumann type of boundary condition (depending on the actual shape of f_0) for \mathbf{P} on $\partial\mathcal{S}_h$. These Neumann type of boundary conditions can be interpreted as an absence of chemical forces and molecular stress in normal direction. Finally $\mathbf{V} \cdot \boldsymbol{\sigma}^{tot} \cdot \boldsymbol{\nu}$ vanishes if $\boldsymbol{\nu}$ is a right side eigenvector of $\boldsymbol{\sigma}^{tot}$.

Settling these boundary conditions allows us to perform the thin shell limit and obtain an effective surface model for active polar gels. For example, considering an one constant type of Frank-Oseen energy $f_0 = K/2\|\nabla\mathbf{P}\|^2 + \mathcal{A}(\|\mathbf{P}\|)$, with state potential \mathcal{A} , we obtain as surface energy and conjugate/molecular field \mathbf{h}

$$f_0^{\mathcal{S}} = \frac{K}{2} [\|\nabla_{\mathcal{S}}\mathbf{P}\|^2 + \|\mathcal{B} \cdot \mathbf{P}\|^2] + \mathcal{A}(\|\mathbf{P}\|) \quad (3.111)$$

$$\mathbf{h} = \underbrace{-K \operatorname{div}_{\mathcal{S}} \nabla_{\mathcal{S}} \mathbf{P}}_{=\mathbf{h}^{di}} + \underbrace{K \mathcal{B}^2 \cdot \mathbf{P}}_{=\mathbf{h}^{cu}} + \underbrace{\mathcal{A}'(\|\mathbf{P}\|)\mathbf{P}}_{=\mathbf{h}^{de}} \quad (3.112)$$

Further we apply the thin shell limit to the conservation laws. Here we observe, due to $\mathbf{P} \cdot \boldsymbol{\nu} = 0$ and $\mathbf{V} \cdot \boldsymbol{\nu} = 0$ that scalar valued equations for conservation of mass and particle numbers remains structurally unchanged.

$$\partial_t \rho + \operatorname{div}_{\mathcal{S}}(\rho \mathbf{v}) = 0 \quad (3.113)$$

$$\partial_t n + \operatorname{div}_{\mathcal{S}}(n \mathbf{v} + \mathbf{j}) = r \quad (3.114)$$

For the momentum balance, as vector valued equation, we expect structural changes. As preparation, we separate the stress tensor $\boldsymbol{\sigma}^{tot}$ into tangential, normal-tangential and normal parts

$$\text{tensor valued: } \boldsymbol{\sigma}_{\mathcal{S}}^{tot} = \{\sigma_{ij}^{tot}\}, \quad (3.115)$$

$$\text{vector valued: } \boldsymbol{\sigma}_{nt}^{tot} = \{\sigma_{\xi i}^{tot}\}, \quad \boldsymbol{\sigma}_{tn}^{tot} = \{\sigma_{i\xi}^{tot}\}, \quad (3.116)$$

$$\text{scalar valued: } \boldsymbol{\sigma}_{\boldsymbol{\nu}}^{tot} = \sigma_{\xi\xi}^{tot} \quad (3.117)$$

We now can separate the momentum balance in a tangential and normal part, where $f(\lambda_{\boldsymbol{\nu}})$ is a shorthand for the scalar valued terms depending on the value of $\lambda_{\boldsymbol{\nu}}$ and its spatial variations.

$$\partial_t \mathbf{m} + \operatorname{div}_{\mathcal{S}}(\mathbf{m} \mathbf{v}) - \operatorname{div}_{\mathcal{S}}(\boldsymbol{\sigma}_{\mathcal{S}}^{tot}) - \mathcal{B} \cdot \boldsymbol{\sigma}_{tn}^{tot} = 0 \quad (3.118)$$

$$\operatorname{div}_{\mathcal{S}}(\boldsymbol{\sigma}_{nt}^{tot}) - \langle \mathcal{B}, \boldsymbol{\sigma}_{\mathcal{S}}^{tot} \rangle_{\mathcal{S}} - \mathcal{H} \lambda_{\boldsymbol{\nu}} = f(\lambda_{\boldsymbol{\nu}}) \quad (3.119)$$

As prescribed by the boundary conditions, $\boldsymbol{\nu}$ is a right side eigenvector and we yield $\boldsymbol{\sigma}_{tn,i}^{tot} = [\boldsymbol{\sigma}^{tot} \cdot \boldsymbol{\nu}]_i = \lambda_{\boldsymbol{\nu}} \boldsymbol{\nu}_i = 0$. In the case of symmetric stress, $\boldsymbol{\nu}$ is also a left eigenvector, such that $\boldsymbol{\sigma}_{nt,i}^{tot} = 0$. In such situations, the tangential and normal momentum balances reduce to

$$\partial_t \mathbf{m} + \operatorname{div}_{\mathcal{S}}(\mathbf{m} \mathbf{v}) - \operatorname{div}_{\mathcal{S}}(\boldsymbol{\sigma}_{\mathcal{S}}^{tot}) = 0 \quad (3.120)$$

$$\langle \mathcal{B}, \boldsymbol{\sigma}_{\mathcal{S}}^{tot} \rangle_{\mathcal{S}} + \mathcal{H} \lambda_{\boldsymbol{\nu}} = -f(\lambda_{\boldsymbol{\nu}}) \quad (3.121)$$

These equations are one way coupled and we have to distinguish two cases.

We can either consider λ_ν as a state variable describing the force exerted by the active polar gel in normal direction, due to bending of the fluid layer. Or we can assume dynamics without normal forces $\lambda_\nu \equiv 0$. In this case the surface stress must satisfy the condition $\langle \mathcal{B}, \sigma_S^{tot} \rangle_S = 0$ which imposes a very restrictive state constraint given by the geometry.

Given these conversation equations, we can turn to the Onsager relations and discuss additional terms emerging by the thin shell limit for $f_0^{S_h} \rightarrow f_0^S$. Using $\mathbf{v} = 1/2(\nabla_S \mathbf{v} + \nabla_S \mathbf{v}^T)$ we yield fully analogous relations to [40] in the surface bound state variables

$$\sigma_S^d = 2\eta\mathbf{v} + \frac{\nu_1}{2} (\mathbf{p}\mathbf{h} + \mathbf{h}\mathbf{p} - (\mathbf{p} \cdot \mathbf{h})\mathbf{g}) + \zeta\Delta\mu \left(\mathbf{p}\mathbf{p} - \frac{\mathbf{p} \cdot \mathbf{p}}{2}\mathbf{g} \right) \quad (3.122)$$

$$\frac{D^c \mathbf{p}}{Dt} = -\nu_1 \mathbf{p} \cdot \mathbf{v} + \frac{1}{\gamma} \mathbf{h} + \lambda_1 \mathbf{p} \Delta\mu \quad (3.123)$$

$$r = -\zeta \left(\mathbf{p}\mathbf{p} - \frac{\mathbf{p} \cdot \mathbf{p}}{2}\mathbf{g} \right) : \mathbf{v} + \lambda_1 \mathbf{p} \cdot \mathbf{h} + \Lambda \Delta\mu \quad (3.124)$$

Additional terms, due to curvature, emerge by recalling the conjugate force contributions $\mathbf{h}^{cu} = K \mathcal{B}^2 \cdot \mathbf{p}$ and $\mathbf{h}^{de} = \mathcal{A}'(\|\mathbf{p}\|)\mathbf{p}$. Considering the typical terms $\mathbf{p}\mathbf{h}$ and $\mathbf{p} \cdot \mathbf{h}$ we yield

$$\begin{aligned} \mathbf{p}\mathbf{h} &= \frac{1}{2} \left(\mathbf{p}\mathbf{h}^{di} + \mathbf{h}^{di}\mathbf{p} \right) + \frac{K\mathcal{H}}{2} (\mathbf{p}\mathbf{p} \cdot \mathcal{B} + \mathcal{B} \cdot \mathbf{p}\mathbf{p}) + (\mathcal{A}'(\|\mathbf{p}\|) - K\mathcal{K}) \mathbf{p}\mathbf{p} \\ &\quad + \frac{1}{2} \left(\mathbf{p}\mathbf{h}^{di} - \mathbf{h}^{di}\mathbf{p} \right) + \frac{K\mathcal{H}}{2} (\mathbf{p}\mathbf{p} \cdot \mathcal{B} - \mathcal{B} \cdot \mathbf{p}\mathbf{p}) \end{aligned} \quad (3.125)$$

$$\mathbf{p} \cdot \mathbf{h} = \mathbf{p} \cdot \mathbf{h}^{di} + K\mathcal{H}\mathbf{p} \cdot \mathcal{B} \cdot \mathbf{p} + (\mathcal{A}'(\|\mathbf{p}\|) - K\mathcal{K}) \|\mathbf{p}\| \quad (3.126)$$

Here we observe that desired alignment of the director towards lines of minimal curvature exerts additional symmetrical and antisymmetric stresses. Also, the discussed interplay of curvature and state potential introduces additional symmetric stresses. For reaction rates r curvature induces additional dissipative contributions by unaligned particles or curvature-defect interaction.

Overall, this sketch demonstrates how, by determining suitable boundary conditions and performing the thin shell limit, an effective surface model for active polar gels can be derived. A short glance on the additional terms of the surface model highlights that restricting active polar gels to thin shells gives rise to several coupling mechanisms between the gel and the curvature of the thin shell. These couplings originate in the non scalar nature of the state variables and geometric constraints imposed by the surface topology.

3.4.1 Conclusion

In this chapter we presented a fundamental approach to model the coupling of mechanochemical processes and geometry of thin shells. We used numeric experiments and theoretic considerations to explored the proposed models, the key results are:

Dynamics in thin shells can be described by effective surface models We presented two methods to derive effective surface models, basing each on a specific assumption. In section 3.2

we started with an apriori assumption of homogeneity in normal direction. The second approach labeled thin shell limit, presented in section 3.3, made specific assumption on the boundary conditions for the variables defined in the thin shell. Both approaches can be interpreted as a result of external forcing. Which modeling is more suitable, most likely depends on considered system and should be decided by physical experiments.

The thin shell limit has proven to be an analytical tool to derive effective surface models. On the one hand side, it provides an error estimate by $1/h^2$ for the effective model and on the other hand side it has been established that derived surface models are consistent with the thermodynamic processes described by a L^2 gradient flow. By the continuous limiting process from thin shell to surface we have gained insight how dynamics of normal and tangential components of hydrodynamic variables decouple.

Fundamental for the process $h \rightarrow 0$ is the choice of boundary conditions at the thin shells boundary. The relevance of this modeling choices can be demonstrated by considering the thin shell limit of the elastic energy of polar ordering (3.46). With the boundary condition $\mathbf{P} \cdot \boldsymbol{\nu} = 0$ we would yield the discussed surface elastic energy (3.51), while requiring $\boldsymbol{\nu} \times \nabla \times \mathbf{P} = 0$ would yield a surface model equivalent to the intrinsic energy (3.54), lacking the curvature contribution $\int_{\mathcal{S}} \|\mathcal{B} \cdot \mathbf{P}\|^2 d\mathcal{S}$.

In the context hydrodynamic theory the rate of dissipation provides instructive restrictions on the choice of suitable boundary conditions for the hydrodynamic variables. Here we used the approach to choose boundary conditions such that the boundary contributions to the rate of dissipation vanish, preserving the thermodynamic consistency of the original volume models.

Due to its continuous description of the dimensional reduction and its consistency the thin shell limit has shown to be a generic approach applicable to complex hydrodynamic systems like active polar gels.

Hydrodynamic variables of orientational order couple in complex manner to the geometry We have discussed possible coupling mechanism along the example systems of polar and nematic order. These effective surface models can be considered as prototype systems of vector and tensor valued hydrodynamic variables. There, we observed that the amount and type of possible couplings increase with the tensorial degree.

Further the effective dimensional reduction in thin shells required a special attention to preserve symmetry properties of the volume Q-tensor, see eigenvalue spectra, in the effective surface models. Here we had to take the normal parts into account, leading to another coupling mechanisms. The explored coupling mechanisms can be roughly summarized into three categories.

By dimensional reduction, while requiring a suitable notion of tangentiality on the thin shell boundaries, lead to the emergence of geometric frustration and defects. The experiments confirmed the strong coupling of defect positioning and local curvature. Further we have observed that inho-

ogeneous curvature leads to distortion in the defect shapes. It has been demonstrated how the overall modulations of the surface curvature influence the energetic landscape of the surface models. Namely, we showed the emergence of local energetic minima by curvature modulation. Therefore curvature can induce and stabilize, otherwise unstable, non minimal defect configurations.

The second category includes a wide array of couplings, stemming from the interaction of the thermotropic energy with the local curvature. Here we observed how, depending on the type of orientational order, coupling to geometry can induce areas of broken order which are not defects, in the sense of isolated zeros. In the case of rotational symmetric Q tensors $\hat{\mathbf{Q}}(\mathbf{q}, -1/3S^*)$ we have demonstrated that curvature can induce non local areas of broken order, effectively reintroducing the coexistence of nematic and isotropic phase.

Finally we observed that anisotropic shapes of \mathcal{S} and non homogeneous curvature induces a geometric forcing in the effective surface models that removes the energetic invariance under consistent rotation of the state variables.

Overall, the occurrence of coupling mechanism depends on the tensorial degree of the considered variable as well as the chosen boundary conditions in the thin shell limit. Anyhow, most of these mechanisms interfere with each other, enabling a wide array of complex states and dynamics.

An effective model of active polar gels in curved thin shells We used the thin shell limit to derive an effective surface model for active polar gels in thin shells. There, we observed a coupling of polar order variables and geometry. Due to the active nature of the gel, these coupling terms induced additional stresses governed by local curvature and the position of defects.

Given a natural boundary condition of strict normal orientation of normal stresses $\Pi_{\mathcal{S}}[\boldsymbol{\sigma}^{tot} \cdot \boldsymbol{\nu}] = 0$, we yielded in the momentum balance a decoupling of normal and tangential components of the stress.

It has been discussed how activity destabilizes the uniform orientational order and lead to the emergence of defects in flat domains, see e. g. [39, 77]. The additional effects given by restricting the dynamics to thin shells, the discussed couplings and geometric forcings add to this complexity.

Coupling effects are strong on cellular scale The proposed models are derived unit free and under the assumption that the considered physical systems form continua. While the tangential alignment is predominant in the case of the cortical layers, the ratio of molecule vs system size might push the modeling, by continuous macroscopic order parameters, to the limit.

Rescaling the effective surface models, revealed that for shrinking system size the energy contributions of thermotropic energy and intrinsic/tangential distortion does not change while the curvature related terms increase by $1/l^2$.

The numerical experiments have been performed at $K, L = 1$ and $l = 1$. Considering the *C. elegans* embryo with $l \approx 10^{-6}$ [m] and using a value obtained for experiments with a nematic suspension [71] where $L \approx \mathcal{O}(10^{-12})$ [N] as orientation, we have a ratio $L/l^2 \approx \mathcal{O}(1)$. Under this assumption we expect the observed effects of coupling ordering and geometry to be observable at cellular scale.

To validate the proposed models experimental data is needed. Experiments regarding the localized melt in areas of positive or negative Gaussian curvature and the preferred alignment along lines of minimal curvature could provide valuable insights for answering this question.

CHAPTER 4

ALIGNMENT OF A DEVELOPMENTAL AXIS BY A MECHANICAL FEEDBACK LOOP

4.1 Establishment of a Developmental Axis in the *C. elegans* Embryo

The *C. elegans* embryo breaks the first symmetry in its cellular organization before the first cell division, resulting in a different biochemical composition of one half of the cell compared to the other. This difference coordinates a so-called asymmetric cell division; a division where both daughter cells differ in size but also chemical composition. This asymmetric division is the event that specifies the location of the future head and tail. Consequently, embryologists identified this time-point as the moment of the establishment of the head-tail, or also called anterior-posterior axis. Key to this symmetry breaking is the formation of so-called polarity domains; membrane-regions which are populated with only with either pPAR or aPAR proteins.

Interestingly, these PAR domains are always aligned with the ellipsoidal shape of the embryo at the time of the asymmetric cell division. At the moment when these domains just form, the alignment is however not that pronounced. A significant fraction of embryos shows pronounced misalignment between the axis defined by the polarity domains and the geometric axis of the ellipsoidal shape. This misalignment is corrected by the cell, but the underlying mechanism that conducts this alignment has been unknown so far. Elucidating this mechanism will be the focus of this chapter.

The PAR domain formation is well described as a process where a bistable reaction diffusion system undergoes a guided transient between two stable states [27, 17, 21, 52]. The initial state consists of a homogeneous distribution of anterior proteins (aPAR), residing in the cortex, and

the posterior proteins (pPAR), distributed in the cytoplasm. The state is actively distorted by a depletion trigger that depletes the aPAR concentration via advective transport [51, 17]. There, pPARs bind to the cortex and, by mutual exclusion, an interface is established such that stable exclusive PAR domains in cortex and cytoplasm form. As demonstrated in [48] and shown in figure 2.10 these domains can be displaced along the cortical domain by cytoplasmic streaming. Such displacements are also observed in the normal course of development, e. g. due to misplaced sperm entry point [18]. Remarkably, such misplaced PAR domains have been observed to align to the long body axis in the phase of cytoplasmic streaming, see figure 4.1-C.

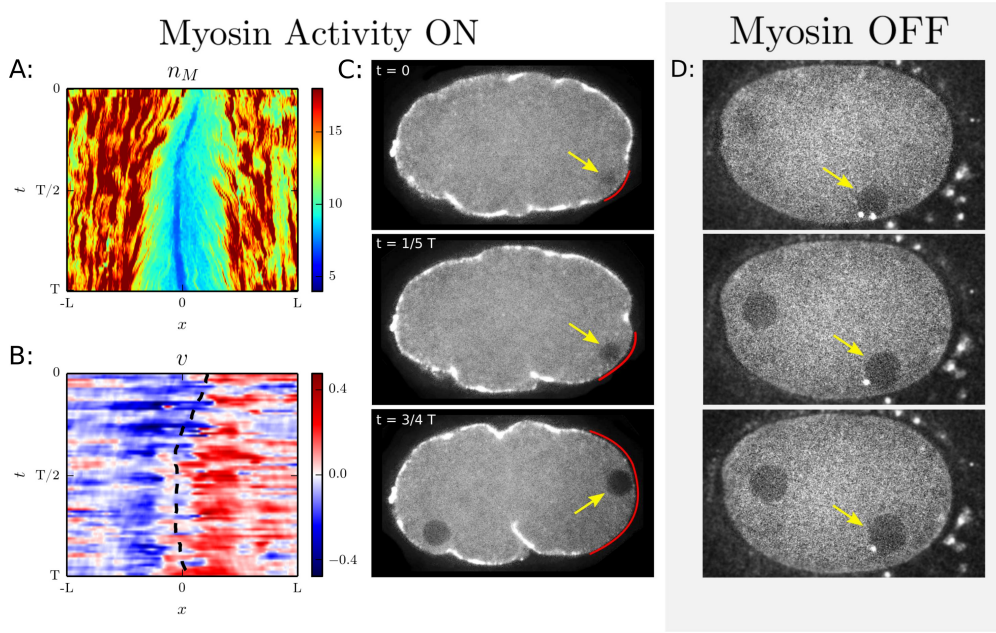


Figure 4.1: ***In-vivo* observations of axis alignment w.r.t. Myosin activity:** [A-C]: Experimental observations for *C. elegans* embryo with misaligned nucleus (e. g. due to displaced sperm entry [19]). Myosin depletion is correlated with nucleus position. [A]: Cortical Myosin particle numbers, $x = 0$ indicates posterior pole, $x < 0$ upper part and $x > 0$ lower part of cortical domain. [B]: Cortical velocity magnitudes w.r.t. counter clockwise orientation. [C]: Snapshots of microscopy at central plane with labeled Myosin particles. Male nucleus (indicated by yellow arrow) is transported through cytoplasmic flow phase to align with long body axis. Cortical area of Myosin depletion (red labeled) is aligned with nucleus position. [D]: Snapshots of microscopy at central plane of genetic mutant with disabled Myosin activity and misaligned male nucleus (indicated by yellow arrow). No alignment of nucleus with long body axis is observed.

Systematic investigations exploring the mechanical properties of the cortical layer [46, 68] established an accurate notion of the mechanical processes in the cortex leading to cytoplasmic streaming. Key concept is that Myosin motors individually generate isotropic stresses, while through non-homogeneous distribution of motors a non-zero stress balance occurs and forces are exerted.

At the onset of cell polarization the Myosin is evenly distributed in cytoplasm and cortex. Furthermore, the activity of the motors increase at the onset such that an increased isotropic stress across the cortex is observed. In the normal development the symmetry of cortical stresses is

broken by centrosome, which induces a localized depletion of Myosin close to the trigger position. The thereby induced cortical flows have been identified, see chapter 2, to drive the cytoplasmic streaming.

Remarkably, suppressing the active stress generation, by genetically deactivating the Myosin activity, does not only yield no cortical or cytoplasmic streaming but also suppresses the self alignment of the PAR domains as shown in figure 4.1-D. Such observation provides a first hint on the mechanical nature of the driving mechanism of the self alignment, ruling out an exclusive (re)binding phenomena in the PAR chemistry as suggested in [16]. Furthermore, [21] demonstrates that the location of PAR domains is tightly coupled to the trigger position. In [27, 52, 18] the centrosome is suggested as central cellular organizer, thereby providing the triggering cue in this process. The centrosome being attached to the envelope of the male nucleus, adds the position of the nucleus as relevant to entity to the system.

Thereby understanding how the repositioning of nucleus and associated Myosin depletion region is facilitated, will also provide a statement regarding the alignment of PAR domains.

In this set up, we will propose and discuss a control mechanism capable of robustly aligning Myosin domains and nucleus position with the embryos long body axis. Therefore the central questions of this chapter are:

What kind of mechanism enables a control such that Myosin and PAR domains robustly align with long body axis? How does the mechanism sense the desired geometric axis?

As suggested by the strong dependence of the self alignment on Myosin activity, we propose a mechanical feedback loop. Key ingredients are the depletion trigger position, which we identify with the nucleus position, the cortical concentrations of Myosin, cortical flows and nucleus transport by cytoplasmic streaming.

To establish and validate the proposed feedback system we structure the chapter as follows. In the initial section 4.1.1, we briefly review a recent model for the mechanical processes in the cortex induced by Myosin gradients [21]. Given this building block we can detail the mechanical feedback loop in section 4.1.2. Furthermore, to obtain a quantitative understanding of the alignment process, we analyze and discuss an experimental data set of cortical and cytoplasmic flow fields capturing the self alignment process in section 4.2. As second step, we aim for a qualitative understanding of the underlying mechanisms. In section 4.2.2 we provide an intuitive model reproducing the nucleus trajectories and apply linear stability analysis to describe the fundamental geometry sensing mechanism. We derive an additional model of cortical activity from first principles via thin shell limit technique in section 4.3 and discuss the impact of the curved nature of the cortical layer on the mechanical processes. To concluded the chapter, we summarize the proposed mechanical feedback system, its key mechanisms and discuss the observed couplings between mechanics and geometry, see section 4.4.

Description of experimental data set and nomenclature As reference and for validation purpose we consider a data set similar to the one used in section 2.2. Across a set of 6 individual *C. elegans* embryos we have a sequence of snapshots consisting of a central 2D slice through the cell body. From these observations we can extract the cell shape Γ_C and the nucleus center \mathbf{x}_N . Furthermore, we can infer cortical Myosin particle numbers n_M and flow velocities v as well as the cytoplasmic flow fields \mathbf{V} . To limit impact of noise and to cancel elastic effects in the flow fields we perform a temporal binning across 10 [s].

As geometric reference shape we use an ellipse (major axes $[27 [\mu\text{m}], 15 [\mu\text{m}]]$), which has been obtained by best fit across all individuals and snapshots. On this ellipse \mathcal{E} we define a counterclockwise tangential direction \mathbf{t} . We define the posterior pole as origin of a cortical coordinate system $x \in [-L, L]$. There, L corresponds to the half of the ellipse circumference. $x \in [0, L]$ denotes the "upper" and $x \in [-L, 0]$ the "lower" branch of the observed cortical slice (see e. g. figure 4.3-B). We use this coordinate system to describe the origin of flow $d(t)$. This point is defined by evaluating the point on the reference ellipse with minimal distance to the nucleus center \mathbf{x}_N . We abbreviate the relation between origin of flow and nucleus position by $d(t) = \Pi_{\mathcal{E}}[\mathbf{x}_N(t)]$. Finally, we define the cortical velocity vectors by $\mathbf{V}_C = vt$.

4.1.1 Active Mechanics of Cortical Streaming

A recent paper [21] provides a comprehensive model of the chemo-mechanical dynamics of the cortical PAR domain formation process. Here the *in-vivo* observations are reproduced by a system with the principal components PAR chemistry, Myosin driven active mechanics and a trigger.

The model uses a basic approximation of the cellular geometry by assuming the cortical domain as a flat, periodic, one dimensional geometry. Thereby, the neighboring cytoplasm is not modeled explicitly. Nonetheless, the cytoplasm is present in the model as a reservoir for PAR and Myosin particle, such that the total number is preserved and as a friction contribution in the mechanical force balance, representing the drag between the cytoplasmic and cortical flows. Furthermore, the rod like nature of the Actin mesh work is neglected such that only isotropic active stresses are included, compare to the model of cortical activity by an active polar fluid discussed in chapter 3, equation (3.122). The cortical layer is considered as a barotropic, compressible fluid where pressure is approximated by linear relation to the density, which is identified with the Myosin particle number.

In this set up the PAR and Myosin particle numbers are described by advection-diffusion-binding equations and the active mechanics are expressed by a force balance at Stokes regime. The trigger enters the model as a additional localized source term in the pPAR, Myosin equation and as a temporal modulation of the active stresses.

Active mechanics and system trigger Since we suspect a mechanical process as driving effect in the axis alignment we review on the mechanical part of the model given in [21] in detail

$$\partial_t n_M = \underbrace{D_M \partial_{xx} n_M}_{\text{diffusion}} - \underbrace{\partial_x \cdot (v n_M)}_{\text{advection}} + \underbrace{k_{on,M} n_M^{cyto} - k_{off,M} n_M + \mathcal{R}_M n_M}_{\text{binding dynamics}} \quad \text{in } [-L, L] \quad (4.1)$$

$$\lambda^2 \partial_{xx} v - v = \underbrace{\mathcal{R}_v \partial_x \left(\frac{n_M}{n_M + n_M^*} \right)}_{\text{active force}} \quad \text{in } [-L, L] \quad (4.2)$$

$$\mathcal{R}_M = k_{off,M} \mathbb{K}_M(x) f_M(t), \quad \mathcal{R}_v = C^* f_v(t), \quad n_M^{cyto} = n_M^{tot} - \frac{\psi}{2L} \int_{-L}^L n_M dx \quad (4.3)$$

The first equation describes the dynamics of the Myosin particle numbers n_M with diffusivity D_M and binding rates $k_{on,M}$, $k_{off,M}$. The second is the force balance w.r.t. velocities v and third line provides the definition of the trigger terms \mathcal{R}_M , \mathcal{R}_v and particle conservation. In the force balance, we summarize the barotropic pressure and isotropic active stress to the left hand side term and refactor with $-\gamma$ and yield the hydrodynamic length scale $\lambda = \sqrt{\eta/\gamma}$. The trigger contributions are separated in a fixed spatial profile and switching functions

$$\mathbb{K}_M(x) = k_M e^{-(x/\sigma_M)^2} \quad (4.4)$$

$$f_{(\cdot)}(t) = \frac{1}{2} \left[\tanh \left(\frac{t}{\tau_{(\cdot),on}} \right) - \tanh \left(\frac{t - T_{(\cdot)}}{\tau_{(\cdot),off}} \right) \right] \quad (4.5)$$

Reviewing this model we observe two major features.

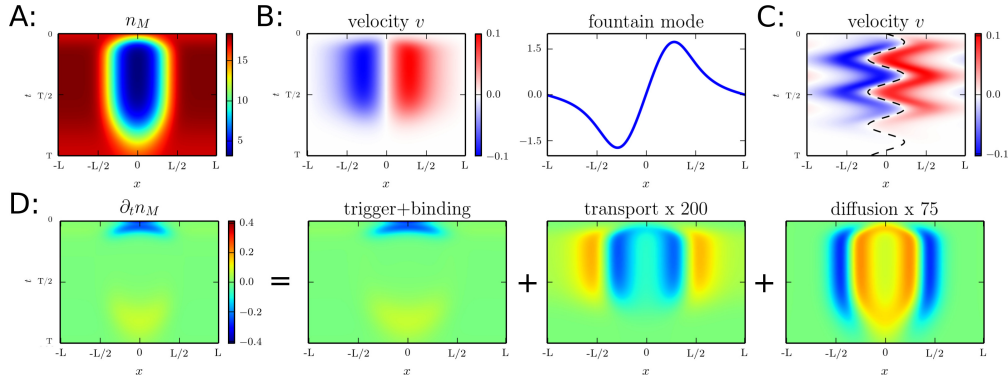


Figure 4.2: Dynamics of mechanical contribution in cortex: [A]: Depletion of Myosin concentration [B]: cortical flows induced by Myosin gradients, and characteristic, normalized flow profile labeled fountain mode \mathbb{X} [C]: evaluated flow profile for moving trigger, trajectory of trigger indicated by black dashed line [D]: decomposition of Myosin concentration evolution, impact of trigger at $\mathcal{O}(10^{-1})$ while transport and diffusion at $\mathcal{O}(10^{-3})$. Transport and diffusive contributions are presented rescaled by denoted factor. Model parameters are chosen as described in [21].

The cortical system is driven by the trigger position and strength We evaluate the dynamical system (4.1) with the parameters specified in [21] and consider the kymographs of the state variables n_M and v as shown in figure 4.2-A and B. We observe the described depletion of Myosin in the trigger region and symmetric flows along the gradients of n_M . More precisely we can

identify a dominant flow mode $\mathbb{X}(x)$ such that $v(x, t) \approx k_0(t)\mathbb{X}(x)$ and $k_0(t) \approx f_M(t)$. The mode is obtained by temporal averaging and normalization (w.r.t. the L^2 norm $|\cdot|$ on $[-L, L]$).

$$\tilde{\mathbb{X}}(x) = \frac{1}{T} \int_0^T v(x, t) dt, \quad \mathbb{X} = \frac{\tilde{\mathbb{X}}}{|\tilde{\mathbb{X}}|}, \quad |\tilde{\mathbb{X}}| = \sqrt{\frac{1}{2L} \int_{-L}^L \langle \tilde{\mathbb{X}}, \tilde{\mathbb{X}} \rangle dx} \quad (4.6)$$

Since this mode describes flows originating at the trigger center, we call this the fountain mode. Also by temporal averaging of the active force term $\mathcal{R}_v \partial_x (n_M / (n_M + n_M^*))$ we define a force mode \mathbb{F} . Recalling the essentially diffusion like character of the force balance ($\lambda^2 \gg 1$) in equation (4.1) we are not surprised to find a strong correlation (in sense of a L^2 scalar product) between the fountain and force mode, see figure 4.5-C.

Furthermore, we point out that, due to the homogeneity of the domain (absence of boundaries and curvature, isotropic material parameters) and the neglectable transport, the system is de facto invariant under arbitrary shift in spatial dimension. Therefore applying a shift $d(t)$ to the system we yield equivalently displaced states, see figure 4.2-C. This displacement applies also to the PAR and Myosin distributions. Furthermore, such shifted states can be identified as dynamics of a systems with a moving trigger $\mathcal{R}_M = k_M k_{off, M} \mathbb{K}_M(x - d(t)) f_M(t)$. Here the flow can be approximated by a shifted fountain mode $v \approx k_0(t)\mathbb{X}(x - d(t))$, see figure 4.2-C.

Mechanical response is downstream effect of motor protein dynamics In figure 4.2-D we compare the contributions of binding dynamics, advection and diffusion to the rate of change $\partial_t n_M$. Here we observe a dominance of binding dynamics such that advection and diffusion can be neglected in the dynamics of n_M . In the context of the model presented in [21], we therefore conclude that cortical flows effectively do not couple to the Myosin dynamics and can be considered as a purely downstream effect of the Myosin depletion.

4.1.2 Mechanical Feedback System Promotes Alignment of Nucleus

We now turn to the description of the proposed mechanical feedback loop, see also figure 4.3, driving the alignment of the nucleus position with the long body axis of the embryo. Again we emphasize, by such aligning of the trigger also the developing PAR domains are aligned with the long body axis.

First element of the feedback system are the cortical flows v induced by the active mechanics, see (4.1). As discussed these are downstream effects of the Myosin binding dynamics and resulting flows v are linear w.r.t. to the active forces. Furthermore, these forces are the sole input of the system such that we expect dynamics to cease immediately in the absence of Myosin gradients, as observed in the control experiment in figure 4.1-D.

The second element are the flows \mathbf{V} in the cytoplasmic bulk. As discussed in chapter 2 these flows are driven by the cortical flows. We recall the modeling of the cytoplasmic flows as incompressible Stokes like, chemically inactive and linear w.r.t. the cortical flows at the boundary.

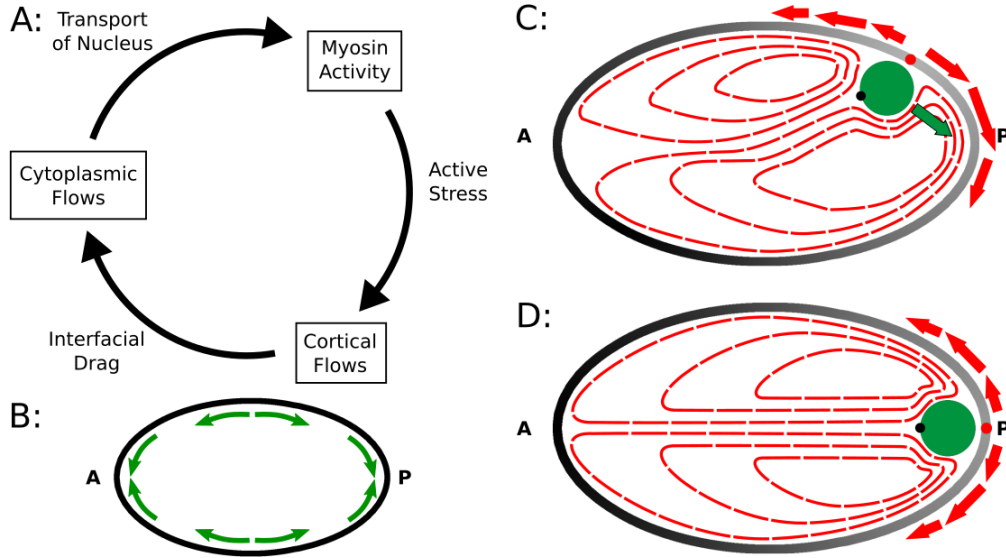


Figure 4.3: **Geometry sensitive mechanical feedback loop facilitates axis alignment of nucleus:** [A]: Three parts of feedback loop: Position of nucleus defines center of Myosin depletion, called origin of flow. Gradients in Myosin motors induce active stress generation in the cortex. Stresses are compensated by cortical flows which induce cytoplasmic streaming. Nucleus is displaced by cytoplasmic streaming. [B]: Stationary points of the feedback loop. No transport for Nucleus positions at anterior/posterior pole (bold A,P), stable position, and at short axis tips, metastable position. Green arrows indicate nucleus transport direction, exhibiting a threshold at short body axis separating attractive regions of A, P pole, as observed in figure 2.10. [C]: Schematic slice of *C. elegans* embryo. Misaligned nucleus (green circle) induces symmetric (w.r.t. origin of flow, marked by red dot) Myosin gradients (gray scale). Resulting active stresses are compensated by asymmetric cortical flows (red arrows). Asymmetry originates in a geometric forcing term scaling with the curvature of cortex. Asymmetric cortical flow induce asymmetric cytoplasmic flows (streamlines as red dashed lines) with non orthogonal stagnation point of cytoplasmic jet on nucleus (black dot). Hydrodynamic forces induce transport of nucleus (green arrow). [D]: Schematic slice of *C. elegans* embryo with aligned nucleus. Due to placement of nucleus on geometric symmetry axis, Myosin gradients induce symmetric cortical flows. Subsequent symmetric cytoplasmic flows with orthogonal stagnation point on nucleus yield no transport.

Last element is the guiding trigger of the binding dynamics of Myosin in the cortex. Experiments [26, 52] have identified the centrosome as a trigger for locally reduced cortical tension. Since the centrosome is attached to the male pronucleus envelope, we use the nucleus center \mathbf{x}_N as approximate location of the centrosome. The position of the guiding trigger d of the cortical dynamics is then defined as closest point on cortex to the nucleus and measured as geodesic distance to the posterior pole. For the nucleus we consider it as free floating in the cytoplasm, such it is transported by the cytoplasmic streaming ($\dot{\mathbf{x}}_N = \mathbf{U}_N$). Again, due to the Stokes character of cytoplasmic flows, the transport is linear with respect to the applied cortical flows v .

The resulting feedback loop is then defined by three steps. For a given nucleus position we yield (by orthogonal projection of \mathbf{x}_N to the cortical domain) a cortical trigger position d , also called origin of flow, which determines the trigger position and the center of Myosin depletion. The resulting Myosin gradients induce cortical and subsequent cytoplasmic flows. As final step the

cytoplasmic flows displace the nucleus and the loop is closed. Please note, at cellular scale and in the parameter regime described by [21] all displacements take *de facto* instantly effect, such that effectively no delay is observed.

4.2 Principal Properties of the Alignment Mechanism

4.2.1 Coupling Mechanisms in the Feedback Loop

To analyze and validate the proposed mechanical feedback loop we review the available *in-vivo* observations under the aspect of the coupling mechanisms, see figure 4.3-A. The coupling of cortical and cytoplasmic streaming via interfacial drag has been established in chapter 2, such that we straight forward apply the discussed model for the cytoplasm.

For the coupling between cytoplasmic streaming and cortex bound Myosin activity we use the available data to validate the nucleus transport as driving mechanism in the displacement of the origin of flow.

The coupling of Myosin activity to generate cortical flows by active stress generation has been modeled [21]. Here we will compare this modeling with the observed velocities by projecting them to a modal basis and discuss agreements and differences.

Transport by cytoplasmic streaming reproduces tangential nucleus velocities and displacement of the origin of flow To obtain a quantitative understanding of the transport of the nucleus and the displacement of the origin of flow d we perform numerical experiments to evaluate the nucleus trajectory by a cytoplasmic flow transport and compare the tangential velocities of the nucleus with the observed velocities as well as comparing the evaluated and observed trajectory of the origin of flow.

To evaluate the nucleus velocities we use a basic transport model for colloids [75]. Analog to the model of chapter 2 we consider cytoplasmic streaming as Stokes flow driven by Dirichlet boundary conditions with values according to the experimentally observed cortical velocities. Following [75] we model the nucleus as a region in the cytoplasm with significantly increased viscosity, effectively suppressing gradients in the cytoplasmic flow field \mathbf{V} . The nucleus region is approximated by a diffuse phase field $\phi_N(\mathbf{x})$. Given the nucleus center \mathbf{x}_N and radius r we can define a phase field function, describing the region, and use it to define spatial variations in viscosity as well as determining the nucleus velocity from the cytoplasmic flow fields

$$\phi_N(\mathbf{x}) = \frac{1}{2} \left[1 - \tanh \left(-\frac{3(\|\mathbf{x} - \mathbf{x}_N\| - r_N)}{\varepsilon} \right) \right], \quad (4.7)$$

$$\eta(\mathbf{x}) = 1 + \eta_N \phi_N(\mathbf{x}) \quad (4.8)$$

$$\mathbf{U}_N = \frac{\int_V \phi_N \mathbf{V} dV}{\int_V \phi_N dV} \quad \text{and} \quad U_{\parallel} = \mathbf{U}_N \cdot \mathbf{t}(\underbrace{\Pi_{\mathcal{E}}[\mathbf{x}_N]}_{=d}) \quad (4.9)$$

Using the diffuse domain parameters β and ε used previously to define cellular domain geometry,

by another phase field function ϕ_C , defined in section 2.2 and using a step viscosity increase of $\eta_N = 100$, the overall model to evaluate cytoplasmic velocities is given by

$$-\nabla \cdot \left[\tilde{\phi}_C \eta (\nabla \mathbf{V} + \nabla \mathbf{V}^T) \right] + \nabla(\phi_C P) = \frac{\beta}{\varepsilon} (1 - \phi_C) (\mathbf{V} - \mathbf{V}_C) \quad \text{in } V \quad (4.10)$$

$$\nabla \cdot (\phi \mathbf{V}) = 0 \quad \text{in } V \quad (4.11)$$

Evaluating the nucleus velocities across all individuals and observed time steps we yield a dataset consisting of 949 points. For systematic comparison we use the ellipse approximation of the cell shape to determine the origin of flow at the cortex, its geodetic distance d to the posterior pole and ellipse normal at the origin of flow to separate the nucleus velocity in normal and tangential contribution.

In figure 4.4-A we observe similar velocity distribution for the evaluated and observed nucleus velocities. Remarkably the evaluated velocities exhibit much stronger variation including data points indicating a transport of the nucleus away from posterior pole. Using a sliding mean (2.5% width) on both velocity data sets we obtain smooth distribution functions. Both function exhibit very low velocities for nucleus positions close to the posterior pole and increasing tangential velocities for higher distances to the pole. Furthermore, the evaluated velocities U_{\parallel} are at magnitudes half of the observed. Reevaluating the trajectories, across all individuals, with consistently rescaled velocities we yield trajectories very close to the observed ones. Therefore, we assume this discrepancy in nucleus velocities as a systematic underestimation of the transport model and introduce the factor $K = 2$ to address this discrepancy.

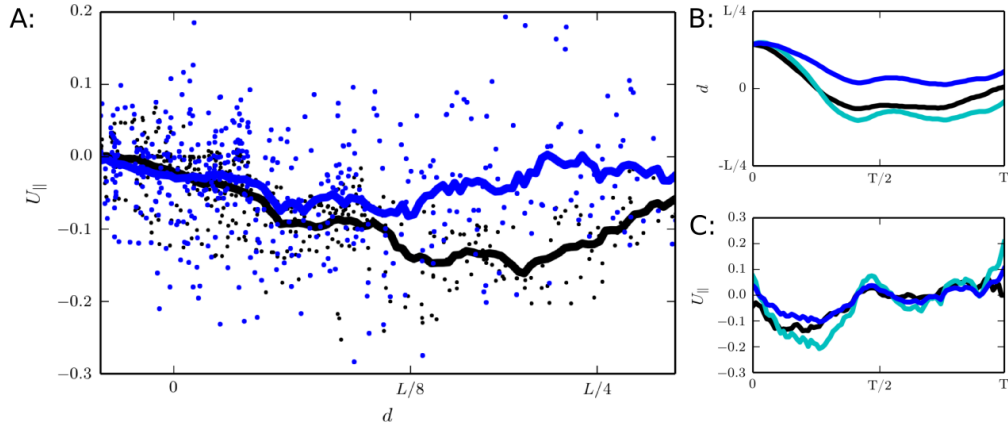


Figure 4.4: **Quantitative comparison of observed nucleus velocities:** [A]: Distribution of tangential nucleus velocities U_{\parallel} versus origin of flow position d . Velocities inferred from observed trajectory (black) and velocities evaluated by model from cortical flows (blue). Dots indicate value for single instant, lines denote sliding mean average (width 2.5%). [B]: Trajectories of origin of flow (black) compared to integrated velocities (blue unscaled velocities, cyan rescaled velocities by $K = 2$) for individual 2. [C]: Temporal distribution of nucleus velocities for individual 2.

To further verify the model we consider the distribution of tangential velocities vs time for each individual. In figure 4.4-C we present these velocities for individual 2 and observe a good

agreement for rescaled velocities. To estimate the systematic impact of strong variations in the evaluated velocities we compare the trajectories $d(t)$ of the origin of flow to observed trajectories. In this case, see 4.4-B, we observe good agreement of the trajectories for $K = 2$.

Overall we conclude that the proposed transport model does reproduce the observed tangential nucleus velocities up to a consistent factor K . The significant better results for comparison w.r.t. an integrated feature, like the trajectories, suggests a strong noise contribution in the observed cortical velocities. Furthermore, we point out that we have not compared normal velocities, since these depend strongly on the modeled nucleus-wall interaction. A fully satisfactory modeling requires a significant better understanding of this interaction. For the time being, we therefore remain with the described model [75] and $K = 2$ to effectively describe the nucleus transport induced by cytoplasmic streaming.

Cortical flows are coupled to nucleus position and excite cytoplasmic transport mode

In section 4.1.1 we discussed a model of cortical flows as proposed in [21]. There, we identified the characteristic flow mode \mathbb{X} . The model made strong assumptions on the homogeneity of the cortical domain, like the absence of a distinct body axis and a translational invariance. Since experimental observations already suggests a sensitivity to the body axis these assumption might not be valid in the case of a misaligned nucleus.

To test the applicability of the model and to identify the contributions of the dominant fountain mode in the observed cortical flows we project them onto a modal basis derived from the fountain mode. Namely we define $\mathbb{Z}_1 = \mathbb{X}$ and define recursively higher order modes by

$$\tilde{\mathbb{Z}}_i = \partial_x \mathbb{Z}_{i-1} - \sum_{l=0}^{i-1} \langle \partial_x \mathbb{Z}_{i-1}, \mathbb{Z}_l \rangle \mathbb{Z}_l \quad \forall i > 1, \quad \mathbb{Z}_i = \tilde{\mathbb{Z}}_i / |\tilde{\mathbb{Z}}_i| \quad (4.12)$$

The resulting mode basis is an alternating sequence of even and odd scalar valued, periodic functions $\mathbb{Z}_i : [-L, L] \rightarrow \mathbb{R}$, $\mathbb{Z}_i(-L) = \mathbb{Z}_i(L)$ with $\int \mathbb{Z}_i dx = 0$. To include flow contribution with non zero mean we also add the constant transport mode $\mathbb{T}(x) = \mathbb{Z}_0(x) \equiv 1$. Furthermore, we have identified the nucleus position \mathbf{x}_N and its cortical counter part, the origin of flow d , as pivotal points in the feedback loop. Therefore we incorporate this dependence as a consistent shift in all modes

$$\mathbb{Z}_i(x; d) = \mathbb{Z}_i(x - d) \quad (4.13)$$

For further reference we use $\mathbb{T} = \mathbb{Z}_0$, $\mathbb{X} = \mathbb{Z}_1$, $\mathbb{Y} = \mathbb{Z}_2$ as short hand for the first three basis modes, see figure 4.5-C for plots of those modes.

Along this basis we can project the observed cortical velocities w.r.t. the trajectory $d(t)$

$$v(x, t) = k_0(t)\mathbb{T}(x) + k_1(t)\mathbb{X}(x - d(t)) + k_2(t)\mathbb{Y}(x - d(t)) + \sum_{i=3}^{\infty} k_i(t)\mathbb{Z}_i(x - d(t)) \quad (4.14)$$

$$\text{where } k_i(t) = \langle \mathbb{Z}_i(x - d(t)), v(x, t) \rangle \quad (4.15)$$

As shown in figure 4.5-A, B (left), we observe the total “kinetic” fluctuations

$$\|v(x, t)\| = \sqrt{\frac{1}{T} \int_0^T |v(x, t)|^2 dt} \quad (4.16)$$

of observed flows v and captured fluctuation by a truncated mode base. Remarkably already the first three modes are sufficient to capture 70–80% of the fluctuations across all observed flow fields. Figure 4.5-D shows the decomposition of experimental flow fields into contributions captured by the first three modes and the residual flows. Here we observe a distinct separation into large structures correlating with the position of origin of flow and high frequency fluctuating residual structures.

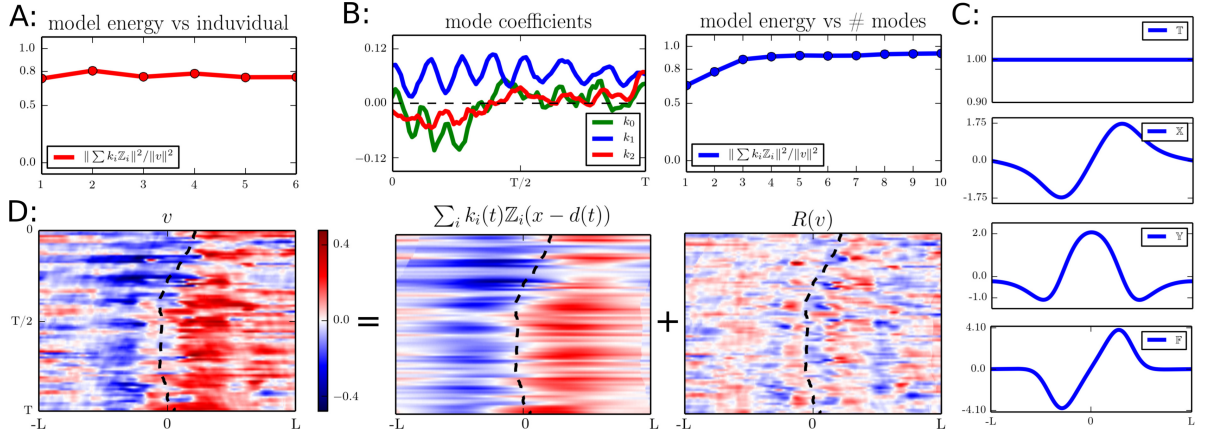


Figure 4.5: **Three fixed shaped flow modes capture essential features of cortical flows:** [A]: relative kinetic energy captured by 3 mode model for set of individuals. [B]: (left) Coefficients functions of first three modes for individual. Functions have been smoothed for plotting purpose with sliding mean 2.5% width. (right) captured relative kinetic energy depending on amount of modes for individual 2 [C]: First invariant model modes. (from top to bottom) Transport mode \mathbb{T} , fountain mode $\mathbb{X}(x)$, shift mode $\mathbb{Y}(x)$ and force mode $\mathbb{F}(x)$. [D]: Decomposition of cortical flows for individual 2. (left) observed flow profiles (mid) flows captured by three mode model (right) residual flows. Black dashed line indicates nucleus position $d(t)$.

Comparing these results to the model of [21] we observe two major features. The most prominent one is the occurrence of two additional modes \mathbb{T} , \mathbb{Y} which are orthogonal to \mathbb{X} and therefore represent dynamics not present in the model of [21]. Furthermore, the coefficients $k_0(t)$, $k_2(t)$, see figure 4.5-B(left) associated with the modes \mathbb{T} , \mathbb{Y} seem to correlate with the displacement of the origin of flow in the sense that $k_0, k_2 < 0 \Leftrightarrow \dot{d} < 0$. On the other hand, the coefficients k_1 associated with the fountain mode \mathbb{X} seem not to correlate with the displacement of the origin of flow.

4.2.2 A Qualitative Model for the Feedback Loop

After finishing the formal description of the coupling mechanisms in the feedback loop and the validation of these couplings with experimental observations, we have established a mode decomposition of the cortical flow w.r.t. to the nucleus position capturing the principal flow structures. We now turn to investigate the impact of the geometry on the feedback loop. Which parts of the loop are sensitive to geometry and how does the broken symmetry relates to the emergence of the threshold of nucleus alignment as observable in figure 2.10 and 4.3-B.

To do so, we extend the mode decomposition of cortical flow to the cytoplasmic flows and set up a basic dynamical system describing the mechanical feedback loop in terms of temporal evolution of the mode coefficient functions $k_i(t)$ and the position of the origin of flow $d(t)$. Such a simplified model might neglect features but enables the application of linear stability analysis, providing insights in the fundamental properties, like stationary points and their stability, of the mechanical feedback loop.

Cytoplasmic flow modes and nucleus transport is sensitive to cell eccentricity Due to the linearity in the coupling of cortical and cytoplasmic flows we can immediately obtain cytoplasmic flow modes $\mathbb{V}_T, \mathbb{V}_X$ and \mathbb{V}_Y , see figure 4.6-A.

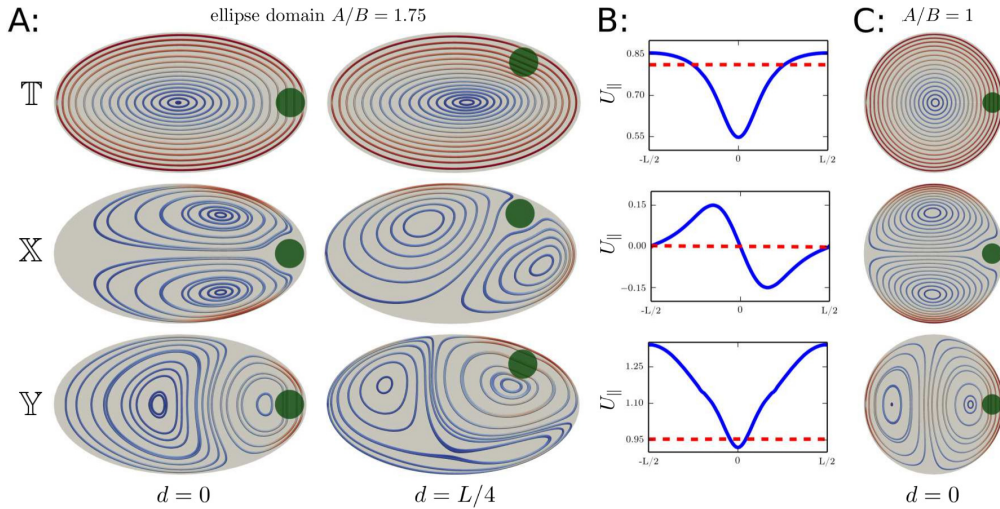


Figure 4.6: **Cytoplasmic flow modes and induced nucleus transport:** [A]: Streamlines of cytoplasmic flows in ellipse domain with body axes [$A = 27 [\mu\text{m}]$, $B = 15 [\mu\text{m}]$] induced by cortical flow modes T (top), X (mid) and Y (bottom) for aligned $d = 0$ (left) and misaligned nucleus $d = L/4$ (right). [B]: Tangential nucleus velocities induced by cytoplasmic flows depending on the alignment of nucleus. $\mathbb{V}_T, \mathbb{V}_Y$ induce nucleus strong positive velocities, implying a clockwise transport (blue lines top and bottom). Nucleus velocities induced \mathbb{V}_X (blue lines mid) with strong dependence on the position d . Subsequent transport is always directed towards the posterior pole, except for nucleus positions at the short body axis $d = -L/2, L/2$ [C]: Control experiment for cytoplasmic flow modes in a circular domain. Resulting nucleus velocities (in B red dashed lines) are invariant under alignment d and \mathbb{V}_X does not yield any transport at all.

Considering the case of an aligned origin of flow $d = 0$, we observe two major features. For

the flows induced by the fountain mode we observe two large vortices forming a jet parallel to the AP axis, as observed in the 2D flow observations of figure 2.1. The jet has its stagnation point at the nucleus and normal to the cortical such that no transport is induced. Quite contrary for the flow modes $\mathbb{V}_{\mathbb{T}}, \mathbb{V}_{\mathbb{Y}}$, which exhibit in the nucleus vicinity vortices flowing parallel to the cortical layer, inducing a strong counter clockwise transport of the nucleus.

Considering now the case for a misaligned nucleus position $d > 0$ we observe for $\mathbb{V}_{\mathbb{X}}$ a similar vortex configuration. But due to the broken symmetry in the cellular domain we observe two unequally deformed vortices, yielding a jet hitting the nucleus off the normal axis. This displaced stagnation point induces a weak nucleus transport. Most remarkably the direction of the transport is always directed towards the posterior pole ($-L/2 < d < L/2$, see figure 4.6-B) such that the unequal deformation of the vortex pair poses a sensing mechanism. Furthermore, we observe that nucleus positions at the symmetry axis of the cell geometry ($d = 0$, L long/AP axis, $d = -L/2, L/2$ short body axis) yield equally deformed vortices and subsequently no nucleus transport by flows of $\mathbb{V}_{\mathbb{X}}$. For the modes $\mathbb{V}_{\mathbb{T}}, \mathbb{V}_{\mathbb{Y}}$ we do not observe such a complex behavior. Regardless the position of the nucleus, its transport remains strong and is always directed counterclockwise.

To emphasize the impact of the cell geometry on this two fold behavior we repeated the calculations on a circular domain, see figure 4.6-C. Due to the symmetry of the geometry the flow modes and associated nucleus transport is independent of d and in the case of $\mathbb{V}_{\mathbb{X}}$ no nucleus transport is induced. Further, combining this findings, regarding the nucleus transport, with the observations of the mode coefficients, see figure 4.5-B, we observe indeed a systematical alignment of the nucleus towards the posterior pole induced by cytoplasmic transport. In detail, for $k_1 > 0$ the associated mode $\mathbb{V}_{\mathbb{X}}$ induces always a weak transport towards the long body axis poles, while k_0, k_2 change signs according to the “desired” direction ($d > 0 \leftrightarrow k_0, k_2 < 0$ and vice versa), yielding strong transport towards the poles.

Geometric sensitivity of cytoplasmic flows enables stationary points of mechanical feedback loop and controls their stability To expand our understanding of the alignment mechanism in terms of modes $\mathbb{Z}_i(x; d(t))$, coefficient functions $k_i(t)$ and nucleus/origin of flow position $d(t)$ we set up a dynamical system. This system describes the temporal evolution of k_i and d , enables to discuss cross-coupling between the modes and systematic analyze w.r.t. stationary points and their stability.

For the cortical dynamics we follow [21] and use a momentum balance consisting of a force input and a friction term as sink mechanism.

$$\rho \dot{v} + \gamma v = F \quad (4.17)$$

We insert the mode expansion discussed in (4.14) and truncate it after three modes.

$$v(x, t) \approx k_0(t)\mathbb{T}(x) + k_1(t)\mathbb{X}(x - d(t)) + k_2(t)\mathbb{Y}(x - d(t)), \quad F(x, t) = f(t)\mathbb{F}(x - d(t)) \quad (4.18)$$

Testing with the cortical flow modes we remove the spatial dependence and obtain a dynamical equations in k_i

$$\dot{k}_j(t) + \dot{d}(t) \sum_i k_i(t) S_{ji} + \frac{\gamma}{\rho} k_j(t) = \frac{f(t)}{\rho} B_j \quad \forall j = 0, 1, 2 \quad (4.19)$$

where the matrix $S_{ji} = \langle \mathbb{Z}_j(x - d(t)), \partial_x \mathbb{Z}_i(x - d(t)) \rangle$ expresses couplings between the mode coefficient functions while $B_j = \langle \mathbb{F}(x - d(t)), \mathbb{Z}_j(x - d(t)) \rangle$ describes the mode excitation by the external forcing. Please note, by the symmetric shift $d(t)$ in these matrix definitions, \mathbf{S} and \mathbf{B} do not depend on d .

To model the temporal evolution of d we use the results of figure 4.6-B to define a set of transport functions $U_{\mathbb{T}}$, $U_{\mathbb{X}}$ and $U_{\mathbb{Y}}$ to express the displacement of d induced by the cytoplasmic flow modes depending on the position of d . The total transport is then a linear combination of the transport functions scaled by k_i

$$\dot{d}(t) = k_0(t)U_{\mathbb{T}}(d(t)) + k_1(t)U_{\mathbb{X}}(d(t)) + k_2(t)U_{\mathbb{Y}}(d(t)) \quad (4.20)$$

Summarizing the transport functions in a vector $\mathbf{U} = [U_{\mathbb{T}}, U_{\mathbb{X}}, U_{\mathbb{Y}}]^T$ as well as coefficient functions $\mathbf{X} = [k_0, k_1, k_2]^T$ we can express the dynamical system in compact notation

$$\dot{\mathbf{X}}(t) + \dot{d}(t)\mathbf{S} \cdot \mathbf{X}(t) = \frac{f(t)}{\rho}\mathbf{B} - \frac{\gamma}{\rho}\mathbf{X}(t) \quad (4.21)$$

$$\dot{d}(t) = \mathbf{X}(t) \cdot \mathbf{U}(d) \quad (4.22)$$

Before turning to the stationary points of this dynamical system we review the properties of the matrices \mathbf{S} and \mathbf{B} . Recalling the fundamental shapes of the cortical flow modes, see figure 4.5-C, we observe \mathbb{F} to be orthogonal to \mathbb{T} and \mathbb{Y} . Combined with the strong correlation of \mathbb{F} and \mathbb{X} we yield $B_1 > 0$ and $B_i = 0$ otherwise.

Furthermore, we use the property of wave number $W(\mathbb{Z}_i)$ doubling across mode pairs to estimate the magnitude of \mathbf{S} entries. Clearly, any derivative of \mathbb{T} yields 0 and the magnitude of $\partial_x \mathbb{Z}_i$ can be estimated by $\mathcal{O}(W(\mathbb{Z}_i)/L)$. Recalling the L^2 norm definition (4.6) and the normalized modes we estimate the entries of \mathbf{S} by $\mathcal{O}(10^{-2})$ for the truncated mode expansion. Compared to the magnitude of $B_1 \approx \mathcal{O}(1)$ and mass matrices equivalent to the unity matrix we observe a very weak coupling between the low order modes.

With these considerations at hand, we now turn to the determination of stationary points. For sake of simplicity we neglect the weak mode cross couplings by assuming $\mathbf{S} \approx 0$ and restrict our considerations to a constant forcing $f(t) \equiv f$. For such autonomous ODE system we obtain following conditions for the stationary points $[\bar{\mathbf{X}}, \bar{d}]$

$$f\mathbf{B} - \gamma\bar{\mathbf{X}} = 0, \quad \bar{\mathbf{X}} \cdot \mathbf{U}(\bar{d}) = 0 \quad (4.23)$$

Thereby yielding $\bar{k}_0 = \bar{k}_2 = 0$ and $\bar{k}_1 = f/\gamma B_1$. Assuming a forcing $f > 0$, this implies $U_{\mathbb{X}}(\bar{d}) = 0$

as a necessary condition for a stationary point.

Reviewing the shape of the transport functions in figure 4.6-B, we observe the condition to met for all positions d in the circular domain. In the case of an ellipse geometry only the poles of long and short body axis $d \in \{-L/2, 0, L/2, L\}$ suffice this condition.

To investigate the stability of the stationary points, we calculate the Jacobian J of the right hand side in (4.21) and yield

$$J = \begin{bmatrix} -\frac{\gamma}{\rho}\mathbb{I}_3 & 0 \\ \mathbf{U}(\bar{d})^T & \partial_d U_{\mathbb{X}}(\bar{d})\bar{k}_1 \end{bmatrix}. \quad (4.24)$$

Immediately we observe the eigenvalues of J to be either negative $-\gamma/\rho$ or to be defined by the slope of $U_{\mathbb{X}}$ in the stationary point. In the case of short body axis stationary points $\bar{d} \in \{-L/2, L/2\}$ the slope is positive making the stationary point meta stable, while for $d \in \{0, L\}$ at the long body/AP axis the stationary points are attractive, see figure 4.3-B.

4.2.3 Systematic Considerations

In the previous sections we have discussed a mechanical feedback loop, facilitating the alignment of a misplaced nucleus with the AP axis in the *C. elegans* embryo. There, we observed a strong impact of geometric effects on the fundamental properties of the feedback loop.

We found the basic flow mode, excited by the Myosin activity, to induce cytoplasmic flows and subsequent nucleus transport to be highly sensitive to the overall eccentricity of the embryo as well as instantaneous position of the nucleus. We observed that this sensitivity is key to enable the existence of localized stationary points, in the overall mechanical feedback loop, as well as it is decisive for the stability of these stationary points.

Furthermore, we have found in the experimental data additional flow modes orthogonal to the basic fountain mode \mathbb{X} . These additional modes \mathbb{T} , \mathbb{Y} , which also induce cytoplasmic modes and subsequent nucleus transport, are drastically less sensitive to geometric properties. Remarkably, we observed these modes to account for a major part of nucleus transport in the alignment process. By the orthogonality of these flow modes to the fountain mode and the forcing created by Myosin activity we conclude that a relevant effect, exciting these modes, is missing in the used model.

As in chapter 2 we recall the three dimensional nature of the *C. elegans* embryo - so far we have considered only experimental data observing the process in a slice of the embryo. Reviewing the experimental data under the notion that the embryo is a three dimension object we point out that the observations did not specify an exact slice, merely requiring the nucleus to be visible. Such indifference in choice of observation slice, indicates some symmetry in the observed phenomena. Regarding the process of Myosin depletion a rotational symmetry w.r.t. the origin of flow seems plausible since the dynamics, see (4.1), are driven by isotropic effects like Myosin (un-)binding or diffusion.

Considering the cortex as a curved thin shell, highlights that we have, so far, treated the cortical velocity as a scalar field w.r.t. a fixed tangential counter clock wise direction. In the three dimensional context we have to treat the vectorial nature of the velocity fields explicitly. Throughout the Chapter 3 we have argued that increased tensorial degree leads to extended coupling between geometry and dynamics, which has been discussed for incompressible fluid dynamics on surfaces by [5, 60]. In these models explicit geometric terms were observed in the momentum balance.

Combining these arguments, we have strong indications for a systematic investigation of the mechanical feedback mechanism in a more detailed geometrical setting, addressing the curved nature of the cortical layer and the volume like nature of the cytoplasmic bulk.

4.3 A Thin Shell Model for Cortical Activity

In this section we aim to derive and discuss a model of the previously defined mechanical feedback loop incorporating the major geometric features of the biological system. Here we consider the cortex as a curved thin shell \mathcal{S}_h enveloping a three dimensional cytoplasmic volume $V \subset \mathbb{R}^3$.

To describe the dynamics of the cortical Myosin and the induced flows we transfer the model presented in [21] to a bounded volume $\mathcal{S}_h \subset \mathbb{R}^3$. With the choice of a set of suitable boundary conditions we use the thin shell limit framework, discussed in chapter 3, to derive an effective surface model for the cortical dynamics. For the cytoplasmic flows in the enclosed volume we use the Stokes flow model analogous to the one presented in chapter 2.

With this model combination, we will investigate the impact of curvature. We use the Helmholtz decomposition to separate cortical flow contribution into active stress and geometry driven parts. In the light of these results we discuss the modeling assumptions and used values for λ of [21]. Furthermore, we propose a modeling including line tension effect due to Myosin gradients and explore it's possible impact on the overall model.

4.3.1 Derivation of an Effective Surface Model

A model of cortical dynamics in flat volume We now will derive a volume model of the cortical activity following the assumptions used in [21]. Furthermore, we consider the coupling mechanisms between Myosin dynamics and cortical flows as given. In this sense we simplify the modeling approach by treating both dynamics separately.

In the case of Myosin dynamics we straight forward obtain following state equations

$$\partial_t n_M + \nabla \cdot (\mathbf{V} n_M) - D_M \nabla \cdot (\nabla n_M) = +k_{on,M} n_M^{cyto} - k_{off,M} n_M + \mathcal{R}_M n_M \quad \text{in } \mathcal{S}_h \quad (4.25)$$

$$\nabla n_M \cdot \boldsymbol{\nu} = 0 \quad \text{on } \partial \mathcal{S}_h \quad (4.26)$$

$$\text{with } \mathcal{R}_M = k_{off,M} \mathbb{K}_M(\mathbf{x}) f_M(t), \quad \mathbb{K}_M(\mathbf{x}) = k_M e^{-(\|\mathbf{x} - \mathbf{x}_0\|/\sigma_M)^2} \quad (4.27)$$

where we have assumed an isotropic depletion signal positioned at \mathbf{x}_0 . As boundary conditions we require no diffusive flux or advective transport of Myosin across the boundary. Later requirement implies $\mathbf{V} \cdot \boldsymbol{\nu} = 0$.

For the momentum balance in \mathcal{S}_h , we assume the cortex as a compressible Newtonian fluid, such that the stress tensor is given by the rate of deformation tensor \mathbf{D} and can be separated in deviatoric and isotropic contributions

$$\mathbf{D} = 1/2 (\nabla \mathbf{V} + \nabla \mathbf{V}^T) \quad (4.28)$$

$$\boldsymbol{\sigma} = \underbrace{\eta \left(2\mathbf{D} - \frac{2}{3} (\nabla \cdot \mathbf{V}) \mathbb{I}_3 \right)}_{=\boldsymbol{\sigma}^d} + \underbrace{P \mathbb{I}_3}_{=\boldsymbol{\sigma}^{iso}} \quad (4.29)$$

Furthermore, we assume Stokes regime, where inertia effects can be neglected, an isotropic friction and use a generalize active stress term analogue to [21]. Requiring purely normal forcing at the boundary we yield following momentum balance

$$-\nabla \cdot \boldsymbol{\sigma} = -\gamma \mathbf{V} + \mathcal{R}_{\mathbf{V}} \nabla \left(\frac{n_M}{n_M + n_M^*} \right) \quad \text{in } \mathcal{S}_h \quad (4.30)$$

$$\Pi[\boldsymbol{\sigma} \cdot \boldsymbol{\nu}] = 0 \quad \text{on } \partial \mathcal{S}_h \quad (4.31)$$

Inserting the stress tensor definition and a linear barotropic approximation for the pressure $P = En_M$ we can rearrange the state equations and yield following state equations for the cortical dynamics.

$$\partial_t n_M + \nabla \cdot (\mathbf{V} n_M) - D_M \nabla \cdot (\nabla n_M) = k_{on,M} n_M^{cyto} - k_{off,M} n_M + \mathcal{R}_M n_M \quad \text{in } \mathcal{S}_h \quad (4.32)$$

$$-\eta \left(\nabla \cdot (\nabla \mathbf{V}) + \frac{1}{3} \nabla (\nabla \cdot \mathbf{V}) \right) + \gamma \mathbf{V} = \mathcal{R}_{\mathbf{V}} \nabla \left(\frac{n_M}{n_M + n_M^*} \right) + E \nabla n_M \quad \text{in } \mathcal{S}_h \quad (4.33)$$

with boundary conditions

$$\nabla n_M \cdot \boldsymbol{\nu} = 0 \quad \text{on } \partial \mathcal{S}_h \quad (4.34)$$

$$\mathbf{V} \cdot \boldsymbol{\nu} = 0 \quad \Pi[\boldsymbol{\sigma} \cdot \boldsymbol{\nu}] = 0 \quad \text{on } \partial \mathcal{S}_h \quad (4.35)$$

Cortex model in curved thin shell yields explicit geometric forcing in momentum balance As next step we consider the volume model in a curved thin shell geometry \mathcal{S}_h as a tubular extension of \mathcal{S} with thickness h . To obtain a compatible model description in curvilinear coordinates we generalize the stress tensor to non trivial thin shell metric \mathbf{G}

$$\boldsymbol{\sigma} = \eta \left(2\mathbf{D} - \frac{2}{3} (\nabla \cdot \mathbf{V}) \mathbf{G} \right) + P \mathbf{G} \quad (4.36)$$

Defining further the tangential, surface bound quantities for the velocity $\mathbf{v} = \Pi[\mathbf{V}|_{\mathcal{S}}]$ and the metric $\mathbf{g} = \Pi[\mathbf{G}|_{\mathcal{S}}]$ we can define the surface bound rate of deformation \mathbf{d} and stress $\boldsymbol{\sigma}_{\mathcal{S}}$ and relate them

to the thin shell quantities as follows

$$\mathbf{D}|_{\mathcal{S}} = \underbrace{\frac{1}{2} (\nabla_{\mathcal{S}} \mathbf{v} + \nabla_{\mathcal{S}} \mathbf{v}^T)}_{=\mathbf{d} \in \mathbb{T}^2 \mathcal{S}} + \mathcal{O}(h) \quad (4.37)$$

$$\boldsymbol{\sigma}|_{\mathcal{S}} = \underbrace{\left(\eta \left[\nabla_{\mathcal{S}} \mathbf{v} + \nabla_{\mathcal{S}} \mathbf{v}^T - \frac{2}{3} \operatorname{div}_{\mathcal{S}} \mathbf{v} \mathbf{g} \right] + P \mathbf{g} \right)}_{=\boldsymbol{\sigma}_{\mathcal{S}} \in \mathbb{T}^2 \mathcal{S}} + P \boldsymbol{\nu} \boldsymbol{\nu} + \mathcal{O}(h) \quad (4.38)$$

With these notions we can straight forward consider the thin shell limit $h \rightarrow 0$ to obtain the surface state equations. For Myosin dynamics, as a scalar valued PDE, we obtain an almost equal formulation

$$\partial_t n_M + \nabla_{\mathcal{S}} \cdot (\mathbf{v} n_M) - D_M \operatorname{div}_{\mathcal{S}} (\nabla_{\mathcal{S}} n_M) = k_{on,M} n_M^{cyto} - k_{off,M} n_M + \mathcal{R}_M n_M \quad \text{in } \mathcal{S} \quad (4.39)$$

Note that by the dimensional reduction of the thin shell limit we have to adjust the notion of distance in $\mathbb{K}_M(\mathbf{x}) = k_M e^{-(d(\mathbf{x}, x_{b0})/\sigma_M)^2}$ to a geodesic one.

For the momentum balance we can insert the stress tensor definition and expand $\operatorname{div}_{\mathcal{S}} \boldsymbol{\sigma}_{\mathcal{S}}$. We yield similar state equation, but with an explicit curvature term (also obtained in the case of incompressible surface bound flows see [5, 60])

$$-\eta \left(\operatorname{div}_{\mathcal{S}} \nabla_{\mathcal{S}} \mathbf{v} + \mathcal{K} \mathbf{v} + \frac{1}{3} \nabla_{\mathcal{S}} \operatorname{div}_{\mathcal{S}} \mathbf{v} \right) + \gamma \mathbf{v} = \mathcal{R}_{\mathbf{v}} \nabla_{\mathcal{S}} \left(\frac{n_M}{n_M + n_M^*} \right) + E \nabla_{\mathcal{S}} n_M \quad \text{in } \mathcal{S} \quad (4.40)$$

The geometric term $\mathcal{K} \mathbf{v}$ has opposing sign compared to friction, we therefore consider this effect rather as a forcing, leading to increased velocities for positive Gaussian curvature.

Geometric forcing excites transport flow mode We will now explore the obtained thin shell model by numerical experiments and compare these results to predictions of the 1D model of [21] and previously discussed *in-vivo* observations. Since the derivation of (4.39) yielded no structural changes in the state equations of n_M we will focus here on the velocity distributions of these models.

To obtain compatible formulations, we recast (4.40) and (4.39) to match the formulation given in [21].

$$\partial_t n_M + \nabla_{\mathcal{S}} \cdot (\mathbf{v} n_M) - D_M \operatorname{div}_{\mathcal{S}} (\nabla_{\mathcal{S}} n_M) = k_{on,M} n_M^{cyto} - k_{off,M} n_M + \mathcal{R}_M n_M \quad \text{in } \mathcal{S} \quad (4.41)$$

$$\lambda^2 \left(\operatorname{div}_{\mathcal{S}} \nabla_{\mathcal{S}} \mathbf{v} + \mathcal{K} \mathbf{v} + \frac{1}{3} \nabla_{\mathcal{S}} \operatorname{div}_{\mathcal{S}} \mathbf{v} \right) - \mathbf{v} = C^* \mathbf{f} \quad \text{in } \mathcal{S} \quad (4.42)$$

For subsequent experiments we use phenomenological parameters λ and C^* in the momentum balance and parameters D_M , $k_{on,M}$, $k_{off,M}$ in the Myosin system as provided in [21]. We evaluate cortical flows and Myosin distributions for several nucleus/origin of flow positions $d \in [0, L/2]$. As domain we use an ellipsoidal shape (major axes $A = 27 [\mu\text{m}]$, $B = 15 [\mu\text{m}]$, $C = 15 [\mu\text{m}]$), approximating *in-vivo* observations. On the temporal axis we consider a constant temporal triggers $f_M(t) = f_v \equiv 1$ (“always on”) and evaluate until a stationary configuration of n_M and \mathbf{v} is reached.

We restrict these solutions to a domain slice (given by the AP axis and the nucleus center/origin of flow on the ellipsoid) and parameterize the slice by a signed distance to the posterior pole. The velocity vectors \mathbf{v} are projected onto a counterclockwise oriented tangential unit vector field to obtain a compatible description v to figure 4.5-D. As second step we project v on the mode basis introduced in 4.5-C.

In the case of Myosin distributions across the ellipsoid slice we observe that the results of the model in [21] are reproduced with good agreement. Under the variation of the origin of flow position d we observe the distributions to be invariant, beside a consistent shift by $-d$. As expected, for scalar valued PDEs and a weak transport, we observe no qualitative or quantitative changes in the model by the change of a flat 1D to the curved thin shell model.

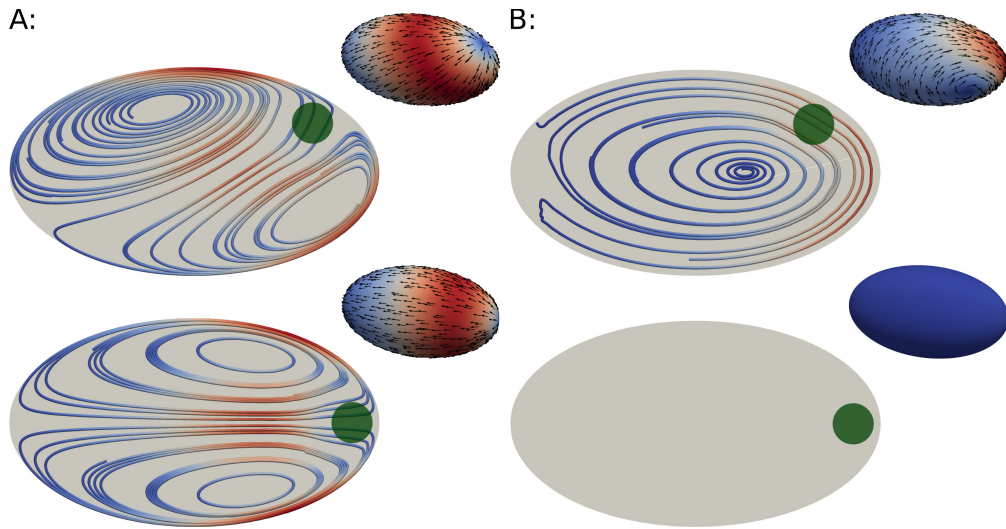


Figure 4.7: **Cortical thin shell model contains transport flow mode in cortex and cytoplasm:** Streamlines of cytoplasmic flows in slice of ellipsoid domain with body axes [$A = 27 [\mu\text{m}]$, $B = 15 [\mu\text{m}]$, $C = 15 [\mu\text{m}]$]. Cortical flow fields (black arrows, colorcoded magnitudes). [A]: Compressible flow contributions for misaligned $d = L/4$ (top) and aligned $d = 0$ (bottom) nucleus (green circle). Compare to fountain mode $\mathbb{V}_{\mathbb{X}}$ flows in 2D case, figure 4.6. [B]: Incompressible flow contributions for misaligned $d = L/4$ (top) and aligned $d = 0$ (bottom) nucleus. Cytoplasmic flows can be considered as superposition of transport $\mathbb{V}_{\mathbb{T}}$ and shift mode $\mathbb{V}_{\mathbb{Y}}$ flows in 2D case, figure 4.6. Incompressible flows cease for aligned nucleus.

Reviewing the evaluated velocity fields we consider the qualitative features of cortical flows. Since we are observing a radial symmetric Myosin forcing \mathbf{f} (w.r.t. to origin of flow and along geodesic distance) we use the Helmholtz decomposition of $\mathbf{v} = \mathbf{a} + \mathbf{b}$ for visualization purpose and refer to them as incompressible ($\mathbf{a} \in \mathbb{TS}$, $\text{div}_{\mathbb{S}}\mathbf{a} = 0$) and compressible ($\mathbf{b} \in \mathbb{TS}$, $\text{rot}_{\mathbb{S}}\mathbf{b} = 0$) contribution. As shown in the icons of figure 4.7 we observe the compressible contribution to match a rotational expansion of the previously observed cortical fountain mode flows. For the incompressible contribution we observe a circular flow, rotating in the plane given by the long body axis poles and the origin of flow. This flow reaches peak velocities at the posterior pole and is oriented from the origin of flow towards the posterior pole. Remarkably this incompressible flow contribution

vanishes for an aligned nucleus $d = 0$ due to the symmetry in the geometric forcing.

To estimate the impact of these two cortical flow contributions on the nucleus transport, we also evaluate the associated cytoplasmic flow modes by a 3D Stokes flow model, analogue to (4.10). Considering now the cytoplasmic flow fields in the slice, see figure 4.7, we observe flow fields similar to the transport mode $\mathbb{V}_{\mathbb{T}}$ (incompressible part) and fountain mode $\mathbb{V}_{\mathbb{X}}$ (compressible part) of the qualitative model, shown in figure 4.6. In the case of vanishing cortical flows for incompressible contribution for aligned nucleus $d = 0$ we also observe no flows in the cytoplasmic bulk.

As final step we compare the cortical velocities of the domain slice with the *in-vivo* observations along the mode coefficients. In figure 4.9-B(top) $\lambda = 11$, we have plotted the coefficients of the dominant modes (\mathbb{T} , \mathbb{X} , \mathbb{Y}) vs. the displacement of the origin of flow. We observe that coefficients of experimentally observed flows are reproduced for small displacements of the nucleus, $|d| < L/16$, while for larger displacements the coefficients of the transport and shift mode are falsely predicted with a factor of ≈ 10 .

Combining these results, we observe three features for the thin shell model describing the cortical activity.

The first feature regards the Myosin dynamics. Here no relevant changes in the model equations and the evaluated behavior are observed. This matches the expectations for a thin shell limit of a scalar valued PDE and underlines the insensitivity of Myosin dynamics to curvature.

In the case of the velocity fields a different behavior is observed. Here, we have identified an additional cortical flow mode which can be related to in-vivo flow patterns, described by the transport and shift mode. This flow mode is not traceable in the 1D flat space model (4.1). Remarkably this additional flow mode is closely coupled to the curvature and its distribution on the surface. Thereby, this mode is sensitive to the geometric symmetries at the origin of flow such that it vanishes for $d \in \{-L/2, 0, L/2, L\}$. Relating this cortical flow mode, via the associated cytoplasmic flow mode, with nucleus transport we observe these points to coincide with the fix points of the mechanical feedback loop predicted by the qualitative model (4.21). The excitation of this additional flow mode can be attributed to the coupling of a vector valued physical field with the curvature of the domain. In the presented form of momentum diffusion $\lambda^2 (\text{div}_{\mathcal{S}} \nabla_{\mathcal{S}} \mathbf{v} + \mathcal{K} \mathbf{v} + \frac{1}{3} \nabla_{\mathcal{S}} \text{div}_{\mathcal{S}} \mathbf{v})$ we observe an explicit geometric forcing which is amplifying existing flows (opposing frictional effects) and scales by the Gaussian curvature of the domain. In the case of the considered ellipsoid geometry the geometric forcing can be estimated by $\lambda^2 \mathcal{K} \in [4.4, 14.5]$.

The third feature concerns the observation that the thin shell model reproduces in-vivo cortical flow fields only for small displacements of the origin of flow. For larger displacement the geometry excited cortical flow mode is too weak to reproduce the experimentally observed flow contributions of transport and shift mode.

4.3.2 Line Tension Induced by Myosin Gradients

The previous section has established a thin shell model of the cortical activity and revealed the existence of a geometry driven flow mode. We observed this flow mode to correlate to the Gaussian curvature \mathcal{K} and coarse grained material parameter hydrodynamic length λ^2 . In the subsequent section we will discuss this material parameter and investigate the sensitivity of the thin shell model w.r.t. λ .

Modeling assumptions in defining the hydrodynamic length In numerical experiments we have used a set of material parameters of the cortex given in [21]. In the case of the hydrodynamic length $\lambda = 11$ we refer to experimental studies [46, 68]. These works use an analogue analytical model and determine the parameters by calibrating towards experimental flows induced by COLA. In both works, two modeling assumption are made. On the one hand, the drag by the neighboring cytoplasm, represented by γ , is constant in time and space. On the other hand, both assume a single driving mechanism to capture the cortical flows (1D contractility in [46] or isotropic active stress in [68]).

Regarding the first assumption, we point out that in several single cell organisms it has been observed [76, 63, 4] that the cytoplasm undergoes several phase transitions between elastic solid to fluid like behavior and back in the course of its cell cycle. Therefore it seems reasonable that such fundamental change in material behavior will correspond to a significant change in cytoplasmic material parameters, like viscosity. As discussed in [72] we know that at an interface of fluids the ratio of viscosities is key for the drag exerted between the fluids. Namely, dragging a fluid with high viscosity consumes more energy than for a low viscosity fluid. So, a significant change in cytoplasmic viscosity, e. g. by a phase transition, will impact the modeled “effective” friction in the cortical model, yielding a different hydrodynamic length. We therefore emphasize the dependency of hydrodynamical length of the cortical layer to the material properties of the cytoplasm, as well as a possible temporal evolution in the ratio of friction and cortical viscosity.

Concerning the second assumption, of a single driving mechanism, we suggest to extend the model by including line tension effects. To clarify what is meant by the notion of line tension, we consider the diffusion of a concentration n on a flat plane. As initial state we assume a circular region at the origin with low concentration and a high concentration in the remaining domain. The diffusive relaxation process of such configuration can be described along the evolution for lines of constant concentration, driven by the chemical potential $\Delta\mu$.

$$\partial_t n = -\Delta\mu \tag{4.43}$$

Furthermore, the normal velocities of this line evolution is proportional to the mean curvature of the line. Reflecting on the contractile nature of these lines of constant concentration, the scaling factor ζ in this relation is called line tension. Coupling the diffusive relaxation to a momentum balance w.r.t. n (not necessarily requiring mass conservation of n) we yield, in the context of Stokes flow, by a Newtonian fluid $\boldsymbol{\sigma} = \eta/2(\nabla\mathbf{V} + \nabla\mathbf{V}^T)$ in contact with another fluid following model

[72, 12, 9]

$$\partial_t n + \nabla \cdot (n \mathbf{V}) = -\Delta \mu \quad (4.44)$$

$$\nabla \cdot \boldsymbol{\sigma} - \gamma \mathbf{V} = -\zeta n \nabla \Delta \mu \quad (4.45)$$

This model includes a forcing term to minimize the length of the contact line between the fluids.

Certainly, the suggested alternative assumptions have to be justified by in-vivo experiments. Nonetheless, in the scope of this work we can not provide such validation.

We therefore consider the alternative assumptions as an extensions of the established models in [46, 68] and use the results of [21] as set up for calibration of material parameters C^* and ζ for a given λ in the case of an aligned nucleus $d = 0$. Such calibrated thin shell models are used subsequently to predict cortical flow patterns for displaced nuclei $d \neq 0$. These predicted flows are then compared to the observed flow patterns in the nucleus alignment process, e.g. figure 4.5-D.

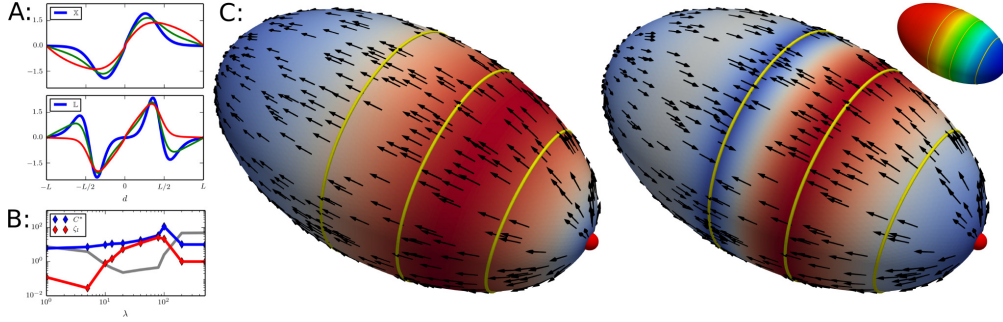


Figure 4.8: **Introducing line tension enables consistent flow reconstruction across one order of magnitude of hydrodynamic length** λ :[A]: Normalized cortical flow modes \mathbb{X} (top) and \mathbb{L} (bottom), w.r.t. to central slice of ellipsoidal geometry, for $\lambda = 5$ (blue), $\lambda = 11$ (green) and $\lambda = 100$ (red).[B]: Calibrated coefficients C^* (blue) and S_l (red) depending on given λ . Light grey line shows L^2 error of cortical flow fields, restricted to central slice, compared to data of 1D model. [C]: Flow fields (fixed size glyphs and color coded magnitude) induced by chemical forcing \mathbf{f}_c (left) and line tension \mathbf{f}_l (right) at $\lambda = 11$. Myosin concentration on ellipsoid (right top). Yellow lines indicate interface by isolines for 10% , 50% and 90% of maximum Myosin concentration.

Line tension effects enable consistent flow field reproduction across a range of hydrodynamic lengths With the previously discussed extended assumptions for modeling cortical activity we yield following thin shell model

$$\partial_t n_M + \nabla_S \cdot (\mathbf{v} n_M) - D_M \text{div}_S (\nabla_S n_M) = k_{on, M} n_M^{cyto} - k_{off, M} n_M + \mathcal{R}_M n_M \quad \text{in } \mathcal{S} \quad (4.46)$$

$$\lambda^2 \left(\text{div}_S \nabla_S \mathbf{v} + \mathcal{K} \mathbf{v} + \frac{1}{3} \nabla_S \text{div}_S \mathbf{v} \right) - \mathbf{v} = C^* \mathbf{f}_{CF} + \zeta_l^2 \mathbf{f}_{LT} \quad \text{in } \mathcal{S} \quad (4.47)$$

As suggested by [12, 60], we have defined the chemical potential of Myosin by $\Delta \mu_M = \text{div}_S \nabla_S n_M$ and yield a line tension force by $\mathbf{f}_{LT} = n_M \nabla \Delta \mu_M$. \mathbf{f}_{CF} denotes the forces exerted by Myosin activity, as defined in [21, 68]. To obtain a compatible formulation with (4.1) we have refactored

line tension coefficient such that $\zeta_l^2 = \zeta/\gamma$.

Utilizing the linearity of the momentum balance w.r.t. source terms we can identify associated cortical flow modes \mathbb{X} , \mathbb{L} and investigate their sensitivity to changes in hydrodynamic length. For the remainder of this paragraph we only consider the aligned nucleus set up ($d = 0$).

Figure 4.8-A shows the normalized flow distribution on a slice of the ellipsoid w.r.t. the signed distance to the posterior pole. Considering flows excited by \mathbf{f}_{CF} and varying the hydrodynamic length we observe for the cortical flow mode \mathbb{X} that the peak velocities are shifted towards the anterior pole eliminating the typical low magnitude flow regime at the anterior pole observed in 1D flat space model. See also figure 4.2.

In the case of flows excited by \mathbf{f}_{LT} we observe a qualitative different behavior. The general shape of \mathbb{L} exhibits three changes in sign inducing posterior pole directed flows in the region of the anterior pole. The peak velocities are correlated with the peak magnitudes of ∇_{SNM} , see figure 4.8-C. Similar to the fountain mode, we observe for increased hydrodynamic length distinct changes in anterior pole region. As shown in figure 4.8-A (bottom) we observe the posterior pole directed flows to cease for sufficient high λ .

With this qualitative understanding of the general sensitivity of the cortical flow modes \mathbb{X} and \mathbb{L} , w.r.t. λ , we can now perform the calibration of C^* and ζ_l for given λ . To do so we consider the minimization of a L^2 distance functional and the steady state cortical flow field v_{1D} obtained by 1D model of [21] as target, i.e.

$$E(v) = \int_{-L}^L \|v - v_{1D}\|^2 dx \quad (4.48)$$

As shown in figure 4.8-B we perform successful calibration for a range of hydrodynamic length scales $\lambda \in [10, 100]$. Off this array the minimization fails to achieve sufficient approximation of the target flow profile yielding significant higher values of $E(v)$. In agreement with the results of [46, 68] we yield in the case of $\lambda \approx 10$ good approximations for weak surface tension contributions $\zeta_l \approx 10^{-2}$ and strong forcing by Myosin activity $C^* \approx 10$. Increasing λ leads to combinations of (C^*, ζ_l) with moderately increased C^* and strong increase in ζ_l . Due to the quadratic influence of ζ_l in the momentum balance we expect the line tension effects to dominate in situations of $\lambda \approx 100$, where $\zeta_l \approx 25$ and $C^* \approx 45$.

Combination of increased hydrodynamic length and line tension effect is key to recover cortical flow profiles for misaligned nuclei After establishing and calibrating the thin shell model, including line tension effects, we consider now a parameter set up for a large hydrodynamic length $\lambda = 80$ and strong line tension $C^* = 45$, $\zeta_l = 25$. As for the set up $\lambda = 11$, $C^* = 10$, $\zeta_l = 0$ used in section 4.3.1, we evaluate the steady states of (4.46) across various nucleus/origin of flow positions $d \in [0, L/2]$ and review the obtained velocity magnitudes v of a slice of the ellipsoidal domain, see figure 4.9-A.

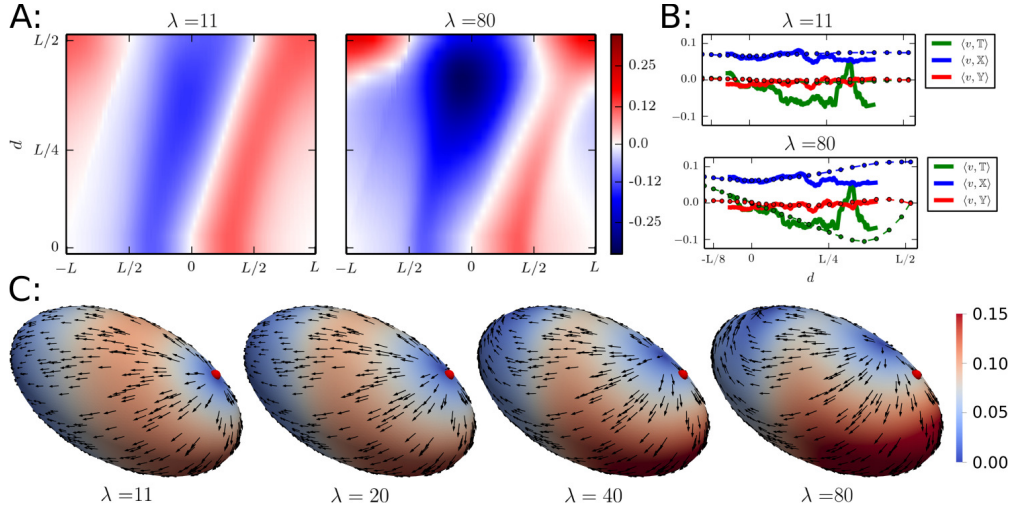


Figure 4.9: **Combination of increased hydrodynamic length and line tension effects amplifies geometric forcing:**[A]: Magnitudes of cortical flows on central domain slice depending on origin of flow position for $\lambda = 11$ (left) and $\lambda = 80$ (right). X axis denotes distance to posterior pole, y axis origin of flow position d by distance to posterior pole. [B]: Mode coefficients of cortical flow fields versus origin of flow position for $\lambda = 11$ (top) and $\lambda = 80$ (bottom). Experimental data (solid lines), smoothed by sliding mean of $1.25\%L$ width, and model predictions (dashed lines) are shown for dominant modes \mathbb{T} (green), \mathbb{X} (blue) and \mathbb{Y} (red). [C]: Cortical flow fields for origin of flow at $d = L/4$ (red sphere) for several values of $\lambda = 11, 20, 40, 80$ illustrating the increasing curvature effects.

It comes to no surprise that we observe coinciding velocities, across the two parameter set ups, for small displacements $d < L/16$. For larger displacements d we observe strong deviation between the set ups. While for $\lambda = 11$ only mild changes (beside a shift of the magnitudes) are observed, $\lambda = 80$ exhibits qualitative changed behavior. Most remarkably, for $d > L/4$ the magnitudes of flows pointing from origin of flow towards the posterior pole are significantly amplified (up to factor 2.5) while flows in opposing direction are suppressed. At higher values of $d \in [3/8L, 1/2L]$ this asymmetry softens such that for $d = L/2$ a symmetric flow profile (w.r.t. to origin of flow d) is obtained. For comparison with experimental data we project the obtained cortical flows onto the mode basis, see figure 4.5-C. In figure 4.9-B we plot the mode coefficients obtained in each set up $\lambda = 11$ (top) and $\lambda = 80$ (bottom) w.r.t. d and compare it to the coefficients of the projected experimental cortical flow fields. Here we observe that the coefficients predicted by the model with $\lambda = 80$ match the experimental data in a domain $d \in [0, L/4]$. For larger displacements the prediction and data start to deviate. As observed in figure 4.4-A, for strong displacements only significantly less measurements are available such that single measurement errors might impair the overall quality of the data.

To complete this investigation we present in figure 4.9-C a sequence of evaluated cortical flow fields with $d = L/4$ for the hydrodynamic length parameters $\lambda = 11, \lambda = 20$ and $\lambda = 80$. In this sequence we observe how the asymmetry of the flows pointing towards anterior and posterior poles amplifies for increasing λ . Furthermore, we monitor an increasing discrepancy of the center

of Myosin depletion (d origin of flow) and the actual origin of flow. Combining these features it is apparent how a transport mode (a constant shift in flow magnitudes v at the ellipsoid slice) can emerge.

4.4 Geometric Effects Drive and Control the Mechanical Feedback Loop

Throughout this chapter we have established a description of the nucleus and PAR domain alignment process by a mechanical feedback system. Three physical effects engage and form following loop: Myosin gradients coupled to the nucleus position form in the cortical layer. These gradients creates active stress in the cortex and induce cortical flows. Finally interfacial drag yields cytoplasmic flow which displace the nucleus.

We were able to qualitatively validate these modeled mechanism against experimental observation. Here nucleus transport poses an exception as our model predicts significant lower velocities (factor 2 – 5) as observed *in-vivo*. We attribute this misprediction to an inaccurate modeling of cortical flows pressing the nucleus into the cortical layer and its mechanical response. To resolve this issue a systematic investigation of this effects seems necessary which is beyond the scope of this work. In a second step we projected the observed cortical flows to a three dimensional basis of characteristic flow modes. By considering the associated cytoplasmic flows we could identify two modes as main facilitator of nucleus transport as well as a characteristic fountain mode associated with the cortical flows induced by Myosin activity in flat space. Finally we transferred an existing flat 1D model of cortical mechano-chemical activity to a thin shell model of a curved cortical layer to identify the driving effect of the flow modes driving the nucleus transport.

Through these steps we were able to analyze the fundamental properties of the feedback loop. Via stability analysis we showed how geometry defines the location of fix points and their stability behavior. We observe in the case of an ellipse shaped cortical layer and enclosed cytoplasm, only long poles of AP axis are attractive fix points while short body axis pole are metastable. Here the distinct sensitivity to the eccentricity of the geometry of cytoplasmic flows associated with the fountain mode is the key element in defining the fix points and their stability. This analysis provides a strong statement towards an explanation of the observations made by [18] as well as the FLUCS induced inverted cell division, see figure 2.10.

Furthermore the thin shell model of the cortical activity revealed that curvature anisotropies induce a forcing which modulates cortical flows generated by fountain mode. Thereby the symmetry of sole fountain mode flows is broken and the asymmetric contribution can be related to the nucleus transporting modes. Due to the tight coupling to the local curvatures we observed in numerical experiments, with ellipsoidal shapes, these modes to induce cytoplasmic flows with a nucleus transport parallel to the direction of Gaussian curvature gradient.

Overall we have found a feedback loop of predominantly linear physical effects restricted to a

nonlinear domain is giving rise to self organizing mechanism, facilitating the alignment of developmental axes defined by nucleus and PAR domains with the long body axis in the *C. elegans* embryo. In detail we could uncover how the geometry contributes to all essential effects in this self organization. This observed mechanism and its analysis are a conclusive example how the geometry of physical domains influences the mechano-chemical morphogenesis and gives rise to surprising features in systems at cellular scale.

CHAPTER 5

CONCLUSION

In the previous chapters we have discussed the interplay of geometry and physical processes in a bounded bulk, a thin shell and a feedback system combining those two entities. The aim of these discussions was to foster the qualitative understanding of morphogenic processes in the model organism *C. elegans* embryo in its single cell state.

Despite the relative simplicity of the model organism compared to a mammal organism, we had to make several strong simplifications to arrive at a system with feasible complexity. First of all, we only considered the time frame in the embryonic development in which cytoplasmic streaming occurs. Furthermore, we focused on mechanochemical processes in this temporal domain and ignored the complex machinery of genetic expression and intra-cellular chemistry. Finally, we neglected the highly heterogeneous molecular structure of the cellular constituents and used a description along hydrodynamic variables. On the basis of these assumptions we have singled out the cellular entities of cytoplasm, cortex and male nucleus for further investigations.

In the course of our investigations we reviewed a particle based model for cytoplasmic streaming and established a complementary description by hydrodynamic variables. The model confirmed the notion of cytoplasmic streaming as Stokes flow driven by cortical flows. Systematic considerations regarding geometry yielded a secondary, quantitative impact of model dimensionality. Apart from this, only a weak impact of boundary curvature was observed such that major features of cytoplasmic streaming were also reproduced in cell shapes approximated by ellipsoids.

Quite contrary results were obtained by considerations regarding the thin shell-like cortex. In the case of a sufficiently thin geometry, $h\|\mathcal{B}\| < 1$, we derived effective surface models, reproducing thin shell dynamics up to an error of $\mathcal{O}(h^2)$. Using the limit $h \rightarrow 0$ framework we yielded a wide range of coupling mechanisms between geometry and dynamics of hydrodynamic variables. We observed the chosen boundary conditions in normal direction of the thin shell and the tensorial degree of the considered variables as key factors in determining the couplings. Furthermore we performed geometric variations for thin shell systems of polar and nematic order where we observed a strong

impact of the geometry. We yielded a local magnetic like forcing on defect positions as well as an impact on a systematic level such that equilibrium states and their stability were decisively influenced.

Combining the effects of cytoplasmic and cortical streaming with the transport of the male nucleus we defined a feedback mechanism. In the coupling of such fundamentally different flow phenomena (incompressible-compressible, volume-surface) we observed geometric properties of the flow domains to heavily impact the feedback mechanism. Breaking the symmetry of the flow domain by an elongated/ellipsoidal shape gave rise to the bistable behavior as observed in the experiments of [18, 48]. By linear stability analysis we observed the two anterior and posterior poles of the cell body as attractive fix points. The equator at the short body axis posed a meta-stable manifold marking the threshold between those two attractive points.

The application of this array of analytical methods was enabled by the strong reduction of model complexity. Nonetheless, the obtained models were capable of reproduce *in-vivo* observation of intracellular dynamics in the sense of flow fields and particle densities.

In the case of cytoplasmic streaming we obtained a parameter free model, accurately predicting the flows by Stokes equations on a qualitative and quantitative level without the use of a fitting parameter.

For the mechanochemical dynamics of cortical flows and evolving Myosin distributions, we were able to reproduce the *in-vivo* observations for aligned nuclei along an established parameter set. As a second step, we explored the model sensitivities with regard to the parameter of hydrodynamic length. By including the additional physical effect of line tensions due to Myosin gradients, we significantly expanded the predictive capacities of the cortical model. This expanded model reproduced the experimental data in the case of an aligned nucleus and the *in-vivo* observations concerning the self organizing process of axis alignment in the advent of initial cell division of the *C. elegans* embryo.

Very remarkably, the obtained parameter set yielded a model prone to the previously discussed geometric effects. Furthermore, these effects lead to the excitation of additional modes of cytoplasmic streaming which have been observed as a driving mechanical feature in the process of axis alignment. Combined with the specification of fix points along the symmetry properties of the cell body shape we consider geometric effects as decisive for driving and controlling this process.

With these examples of a successful interplay of *in-vivo* observations and model predictions we contributed to expanding the qualitative understanding of the intracellular dynamics of the *C. elegans* embryo. We established a theoretical model for a process of spatial self-organisation in the context of asymmetric cell division and identified the geometric effects as vital contributors in this morphogenic process.

BIBLIOGRAPHY

- [1] R. ABRAHAM, J. E. MARSDEN, AND T. RATIU, *Manifolds, tensor analysis, and applications*, vol. 75, Springer Science & Business Media, 2012.
- [2] W. W. AHMED, E. FODOR, M. ALMONACID, M. BUSSONNIER, M.-H. VERLHAC, N. GOV, P. VISCO, F. VAN WIJLAND, AND T. BETZ, *Active mechanics reveal molecular-scale force kinetics in living oocytes*, *Biophysical journal*, 114 (2018), pp. 1667–1679.
- [3] S. ALAND, S. EGERER, J. LOWENGRUB, AND A. VOIGT, *Diffuse interface models of locally inextensible vesicles in a viscous fluid*, *Journal of computational physics*, 277 (2014), pp. 32–47.
- [4] M. ALMONACID, W. W. AHMED, M. BUSSONNIER, P. MAILLY, T. BETZ, R. VOITURIEZ, N. S. GOV, AND M.-H. VERLHAC, *Active diffusion positions the nucleus in mouse oocytes*, *Nature cell biology*, 17 (2015), p. 470.
- [5] M. ARROYO AND A. DESIMONE, *Relaxation dynamics of fluid membranes*, *Physical Review E*, 79 (2009), p. 031915.
- [6] P. W. BAAS, J. S. DEITCH, M. M. BLACK, AND G. A. BANKER, *Polarity orientation of microtubules in hippocampal neurons: uniformity in the axon and nonuniformity in the dendrite*, *Proceedings of the National Academy of Sciences*, 85 (1988), pp. 8335–8339.
- [7] J. M. BALL AND A. MAJUMDAR, *Nematic liquid crystals: From maier-saupe to a continuum theory*, *Molecular Crystals and Liquid Crystals*, 525 (2010), pp. 1–11.
- [8] C. K. BATCHELOR AND G. BATCHELOR, *An introduction to fluid dynamics*, Cambridge university press, 1967.
- [9] D. BOTHE AND J. PRÜSS, *On the two-phase navier–stokes equations with boussinesq–scriven surface fluid*, *Journal of Mathematical Fluid Mechanics*, 12 (2010), pp. 133–150.
- [10] M. J. BOWICK AND L. GIOMI, *Two-dimensional matter: order, curvature and defects*, *Advances in Physics*, 58 (2009), pp. 449–563.
- [11] D. BRAY AND J. WHITE, *Cortical flow in animal cells*, *Science*, 239 (1988), pp. 883–888.

- [12] A. CALLAN-JONES AND R. VOITURIEZ, *Active gel model of amoeboid cell motility*, New Journal of Physics, 15 (2013), p. 025022.
- [13] B. R. DANIELS, B. C. MASI, AND D. WIRTZ, *Probing single-cell micromechanics in vivo: the microrheology of c. elegans developing embryos*, Biophysical journal, 90 (2006), pp. 4712–4719.
- [14] P.-G. DE GENNES AND P.-G. GENNES, *Scaling concepts in polymer physics*, Cornell university press, 1979.
- [15] S. FRANZ, H.-G. ROOS, R. GÄRTNER, AND A. VOIGT, *A note on the convergence analysis of a diffuse-domain approach*, Comput. Methods Appl. Math., 12 (2012), pp. 153–167.
- [16] R. GESSELE, J. HALATEK, AND E. FREY, *Par protein activation-deactivation cycles stabilize long-axis polarization in c. elegans*, bioRxiv, (2018).
- [17] N. W. GOEHRING, P. K. TRONG, J. S. BOIS, D. CHOWDHURY, E. M. NICOLA, A. A. HYMAN, AND S. W. GRILL, *Polarization of par proteins by advective triggering of a pattern-forming system*, Science, 334 (2011), pp. 1137–1141.
- [18] B. GOLDSTEIN AND S. N. HIRD, *Specification of the anteroposterior axis in caenorhabditis elegans*, Development, 122 (1996), pp. 1467–1474.
- [19] R. E. GOLDSTEIN, I. TUVAL, AND J.-W. VAN DE MEENT, *Microfluidics of cytoplasmic streaming and its implications for intracellular transport*, Proceedings of the National Academy of Sciences, 105 (2008), pp. 3663–3667.
- [20] M. GOTTA AND J. AHRINGER, *Axis determination in c. elegans: initiating and transducing-polarity*, Current opinion in genetics & development, 11 (2001), pp. 367–373.
- [21] P. GROSS, K. V. KUMAR, N. W. GOEHRING, J. S. BOIS, C. HOEGE, F. JÜLICHER, AND S. W. GRILL, *Guiding self-organized pattern formation in cell polarity establishment*, Nature Physics, (2018).
- [22] P. GROSS, K. V. KUMAR, AND S. W. GRILL, *How active mechanics and regulatory biochemistry combine to form patterns in development*, Annual review of biophysics, 46 (2017), pp. 337–356.
- [23] M. GUHA, M. ZHOU, AND Y.-L. WANG, *Cortical actin turnover during cytokinesis requires myosin ii*, Current biology, 15 (2005), pp. 732–736.
- [24] M. GUO, A. J. EHRLICHER, M. H. JENSEN, M. RENZ, J. R. MOORE, R. D. GOLDMAN, J. LIPPINCOTT-SCHWARTZ, F. C. MACKINTOSH, AND D. A. WEITZ, *Probing the stochastic, motor-driven properties of the cytoplasm using force spectrum microscopy*, Cell, 158 (2014), pp. 822–832.
- [25] R. J. HAWKINS, R. POINCLOUX, O. BÉNICHOU, M. PIEL, P. CHAVRIER, AND R. VOITURIEZ, *Spontaneous contractility-mediated cortical flow generates cell migration in three-dimensional environments*, Biophysical journal, 101 (2011), pp. 1041–1045.

-
- [26] S. N. HIRD AND J. G. WHITE, *Cortical and cytoplasmic flow polarity in early embryonic cells of caenorhabditis elegans.*, The Journal of cell biology, 121 (1993), pp. 1343–1355.
- [27] C. HOEGE AND A. A. HYMAN, *Principles of par polarity in caenorhabditis elegans embryos*, Nature Reviews Molecular Cell Biology, 14 (2013), p. 315.
- [28] A. R. HONERKAMP-SMITH, F. G. WOODHOUSE, V. KANTSLER, AND R. E. GOLDSTEIN, *Membrane viscosity determined from shear-driven flow in giant vesicles*, Physical review letters, 111 (2013), p. 038103.
- [29] J. HOWARD ET AL., *Mechanics of motor proteins and the cytoskeleton*, (2001).
- [30] J. HOWARD, S. W. GRILL, AND J. S. BOIS, *Turing’s next steps: the mechanochemical basis of morphogenesis*, Nature Reviews Molecular Cell Biology, 12 (2011), p. 392.
- [31] S. A. JENEKHE AND X. L. CHEN, *Self-assembled aggregates of rod-coil block copolymers and their solubilization and encapsulation of fullerenes*, Science, 279 (1998), pp. 1903–1907.
- [32] F. JÜLICHER, A. AJDARI, AND J. PROST, *Modeling molecular motors*, Reviews of Modern Physics, 69 (1997), p. 1269.
- [33] F. JÜLICHER, S. W. GRILL, AND G. SALBREUX, *Hydrodynamic theory of active matter*, Reports on Progress in Physics, 81 (2018).
- [34] L. KAY AND K. JÄNICH, *Vector Analysis*, Undergraduate Texts in Mathematics, Springer New York, 2013.
- [35] F. C. KEBER, E. LOISEAU, T. SANCHEZ, S. J. DECAMP, L. GIOMI, M. J. BOWICK, M. C. MARCHETTI, Z. DOGIC, AND A. R. BAUSCH, *Topology and dynamics of active nematic vesicles*, Science, 345 (2014), pp. 1135–1139.
- [36] S. KOSHIZUKA AND Y. OKA, *Moving-particle semi-implicit method for fragmentation of incompressible fluid*, Nuclear science and engineering, 123 (1996), pp. 421–434.
- [37] S. KRALJ, R. ROSSO, AND E. G. VIRGA, *Curvature control of valence on nematic shells*, Soft Matter, 7 (2011), pp. 670–683.
- [38] K. KRUSE, N. CHIARUTTINI, AND A. ROUX, *Optical control of cytoplasmic flows*, Nature cell biology, 20 (2018), p. 227.
- [39] K. KRUSE, J.-F. JOANNY, F. JÜLICHER, J. PROST, AND K. SEKIMOTO, *Asters, vortices, and rotating spirals in active gels of polar filaments*, Physical review letters, 92 (2004), p. 078101.
- [40] K. KRUSE, J.-F. JOANNY, F. JÜLICHER, J. PROST, AND K. SEKIMOTO, *Generic theory of active polar gels: a paradigm for cytoskeletal dynamics*, The European Physical Journal E, 16 (2005), pp. 5–16.
- [41] X. LI, J. LOWENGRUB, A. RÄTZ, AND A. VOIGT, *Solving pdes in complex geometries: a diffuse domain approach*, Communications in mathematical sciences, 7 (2009), p. 81.

- [42] J. LOWENGRUB, J. ALLARD, AND S. ALAND, *Numerical simulation of endocytosis: Viscous flow driven by membranes with non-uniformly distributed curvature-inducing molecules*, Journal of computational physics, 309 (2016), pp. 112–128.
- [43] K. LUBY-PHELPS, *Cytoarchitecture and physical properties of cytoplasm: volume, viscosity, diffusion, intracellular surface area*, in International review of cytology, vol. 192, Elsevier, 1999, pp. 189–221.
- [44] K. MANDAL, A. ASNACIOS, B. GOUD, AND J.-B. MANNEVILLE, *Mapping intracellular mechanics on micropatterned substrates*, Proceedings of the National Academy of Sciences, 113 (2016), pp. E7159–E7168.
- [45] S. MATHIEU AND J.-B. MANNEVILLE, *Intracellular mechanics: connecting rheology and mechanotransduction*, Current opinion in cell biology, 56 (2019), pp. 34–44.
- [46] M. MAYER, M. DEPKEN, J. S. BOIS, F. JÜLICHER, AND S. W. GRILL, *Anisotropies in cortical tension reveal the physical basis of polarizing cortical flows*, Nature, 467 (2010), p. 617.
- [47] J. W. MILNOR AND D. W. WEAVER, *Topology from the differentiable viewpoint*, Princeton university press, 1997.
- [48] M. MITTASCH, P. GROSS, M. NESTLER, A. W. FRITSCH, C. ISERMAN, M. KAR, M. MUNDER, A. VOIGT, S. ALBERTI, S. W. GRILL, ET AL., *Non-invasive perturbations of intracellular flow reveal physical principles of cell organization*, tech. rep., Nature Publishing Group, 2018.
- [49] D. MIZUNO, C. TARDIN, C. F. SCHMIDT, AND F. C. MACKINTOSH, *Nonequilibrium mechanics of active cytoskeletal networks*, Science, 315 (2007), pp. 370–373.
- [50] N. MORONE, T. FUJIWARA, K. MURASE, R. S. KASAI, H. IKE, S. YUASA, J. USUKURA, AND A. KUSUMI, *Three-dimensional reconstruction of the membrane skeleton at the plasma membrane interface by electron tomography*, J Cell Biol, 174 (2006), pp. 851–862.
- [51] F. MOTEGI AND A. SUGIMOTO, *Sequential functioning of the *ect-2* *rhogef*, *rho-1* and *cdc-42* establishes cell polarity in *caenorhabditis elegans* embryos*, Nature cell biology, 8 (2006), p. 978.
- [52] E. MUNRO, J. NANCE, AND J. R. PRIESS, *Cortical flows powered by asymmetrical contraction transport par proteins to establish and maintain anterior-posterior polarity in the early *c. elegans* embryo*, Developmental cell, 7 (2004), pp. 413–424.
- [53] G. NAPOLI AND L. VERGORI, *Surface free energies for nematic shells*, Phys. Rev. E, 85 (2012), p. 061701.
- [54] M. NESTLER, I. NITSCHKE, S. PRAETORIUS, AND A. VOIGT, *Orientational order on surfaces: The coupling of topology, geometry, and dynamics*, Journal of Nonlinear Science, 28 (2018), pp. 147–191.
- [55] M. NESTLER, I. NITSCHKE, AND A. VOIGT, *A finite element approach for vector- and tensor-valued surface pdes*, Journal of Computational Physics, (2019).

-
- [56] I. NITSCHKE, *Nematic liquid crystals on curved surfaces: a thin film limit*, Poster Session presented at workshop "Mathematics of Thin Structures", Dresden, Germany, (2018, October).
- [57] I. NITSCHKE, M. NESTLER, S. PRAETORIUS, H. LÖWEN, AND A. VOIGT, *Nematic liquid crystals on curved surfaces: a thin film limit*, Proc. R. Soc. A, 474 (2018), p. 20170686.
- [58] I. NITSCHKE, S. REUTHER, AND A. VOIGT, *Discrete exterior calculus (dec) for the surface navier-stokes equation*, in Transport Processes at Fluidic Interfaces, Springer, 2017, pp. 177–197.
- [59] I. NITSCHKE, S. REUTHER, AND A. VOIGT, *Hydrodynamic interactions in polar liquid crystals on evolving surfaces*, ArXiv e-prints, (2018).
- [60] I. NITSCHKE, A. VOIGT, AND J. WENSCH, *A finite element approach to incompressible two-phase flow on manifolds*, Journal of Fluid Mechanics, 708 (2012), pp. 418–438.
- [61] R. NIWAYAMA, H. NAGAO, T. S. KITAJIMA, L. HUFNAGEL, K. SHINOHARA, T. HIGUCHI, T. ISHIKAWA, AND A. KIMURA, *Bayesian inference of forces causing cytoplasmic streaming in caenorhabditis elegans embryos and mouse oocytes*, PloS one, 11 (2016), p. e0159917.
- [62] R. NIWAYAMA, K. SHINOHARA, AND A. KIMURA, *Hydrodynamic property of the cytoplasm is sufficient to mediate cytoplasmic streaming in the caenorhabditis elegans embryo*, Proceedings of the National Academy of Sciences, 108 (2011), pp. 11900–11905.
- [63] B. R. PARRY, I. V. SUROVTSEV, M. T. CABEEN, C. S. O’HERN, E. R. DUFRESNE, AND C. JACOBS-WAGNER, *The bacterial cytoplasm has glass-like properties and is fluidized by metabolic activity*, Cell, 156 (2014), pp. 183–194.
- [64] Z. PETRÁŠEK, C. HOEGE, A. MASHAGHI, T. OHRT, A. A. HYMAN, AND P. SCHWILLE, *Characterization of protein dynamics in asymmetric cell division by scanning fluorescence correlation spectroscopy*, Biophysical journal, 95 (2008), pp. 5476–5486.
- [65] S. REUTHER AND A. VOIGT, *The interplay of curvature and vortices in flow on curved surfaces*, Multiscale Modeling & Simulation, 13 (2015), pp. 632–643.
- [66] —, *Incompressible two-phase flows with an inextensible newtonian fluid interface*, Journal of Computational Physics, 322 (2016), pp. 850–858.
- [67] —, *Solving the incompressible surface navier-stokes equation by surface finite elements*, Physics of Fluids, 30 (2018), p. 012107.
- [68] A. SAHA, M. NISHIKAWA, M. BEHRNDT, C.-P. HEISENBERG, F. JÜLICHER, AND S. W. GRILL, *Determining physical properties of the cell cortex*, Biophysical journal, 110 (2016), pp. 1421–1429.
- [69] G. SALBREUX, G. CHARRAS, AND E. PALUCH, *Actin cortex mechanics and cellular morphogenesis*, Trends in cell biology, 22 (2012), pp. 536–545.

- [70] C. SCHENK, H. BRINGMANN, A. A. HYMAN, AND C. R. COWAN, *Cortical domain correction repositions the polarity boundary to match the cytokinesis furrow in c. elegans embryos*, *Development*, 137 (2010), pp. 1743–1753.
- [71] K. SCHIELE AND S. TRIMPER, *On the elastic constants of a nematic liquid crystal*, *physica status solidi (b)*, 118 (1983), pp. 267–274.
- [72] L. SCRIVEN, *Dynamics of a fluid interface equation of motion for newtonian surface fluids*, *Chemical Engineering Science*, 12 (1960), pp. 98–108.
- [73] I. W. STEWART, *The static and dynamic continuum theory of liquid crystals*, vol. 17, Taylor and Francis, London, 2004.
- [74] K. SVOBODA AND S. M. BLOCK, *Force and velocity measured for single kinesin molecules*, *Cell*, 77 (1994), pp. 773–784.
- [75] H. TANAKA AND T. ARAKI, *Simulation method of colloidal suspensions with hydrodynamic interactions: Fluid particle dynamics*, *Physical review letters*, 85 (2000), p. 1338.
- [76] C. TAYLOR, *The contractile vacuole in euplotes: An example of the sol-gel reversibility of cytoplasm*, *Journal of Experimental Zoology*, 37 (1923), pp. 259–289.
- [77] S. P. THAMPI, R. GOLESTANIAN, AND J. M. YEOMANS, *Instabilities and topological defects in active nematics*, *EPL (Europhysics Letters)*, 105 (2014), p. 18001.
- [78] A. M. TURING, *The chemical basis of morphogenesis*, *Philosophical Transactions of the Royal Society (part B)*, 237 (1953), pp. 37–72.
- [79] E. G. VIRGA, *Variational theories for liquid crystals*, vol. 8, CRC Press, 1995.
- [80] F. M. WEINERT AND D. BRAUN, *Optically driven fluid flow along arbitrary microscale patterns using thermoviscous expansion*, *Journal of applied physics*, 104 (2008), p. 104701.
- [81] F. M. WEINERT, J. A. KRAUS, T. FRANOSCH, AND D. BRAUN, *Microscale fluid flow induced by thermoviscous expansion along a traveling wave*, *Physical review letters*, 100 (2008), p. 164501.
- [82] J. WESTERWEEL, *Fundamentals of digital particle image velocimetry*, *Measurement science and technology*, 8 (1997), p. 1379.
- [83] C. E. WILLERT AND M. GHARIB, *Digital particle image velocimetry*, *Experiments in fluids*, 10 (1991), pp. 181–193.
- [84] P. J. WOJTOWICZ, P. SHENG, AND E. PRIESTLEY, *Introduction to liquid crystals*, Springer, 1975.
- [85] D. ZERROUKI, B. ROTENBERG, S. ABRAMSON, J. BAUDRY, C. GOUBAULT, F. LEAL-CALDERON, D. J. PINE, AND J. BIBETTE, *Preparation of doublet, triangular, and tetrahedral colloidal clusters by controlled emulsification*, *Langmuir*, 22 (2006), pp. 57–62.

Erklärung des Promovierenden zum Antrag auf Eröffnung des Promotionsverfahrens

1. Die folgende Promotionsordnung in ihrer gültigen Fassung erkenne ich an:

Bereich Mathematik und Naturwissenschaften - Promotionsordnung vom 23.02.2011

2. Die Promotion wurde an folgendem Institut/an folgender Professur durchgeführt:

Institut für Wissenschaftliches Rechnen, TU Dresden

3. Folgende Personen haben die Promotion wissenschaftlich betreut und/oder mich bei der Auswahl und Auswertung des Materials sowie bei der Herstellung des Manuskripts unterstützt:

Axel Voigt

4. Ich bestätige, dass für meine Person bisher keine früheren, erfolglosen Promotionsverfahren stattgefunden haben. Andernfalls habe ich diesem Antrag eine Erklärung bzw. Nachweise beigelegt, in dem ersichtlich ist, wo, wann, mit welchem Thema und mit welchem Bescheid diese Promotionsversuche stattgefunden haben

5. Ich versichere weiterhin, dass

(a) ich die vorliegende Arbeit mit dem Titel „Cellular Morphogenic Processes under Geometric Constraints. - Hydrodynamic Modeling and Simulations, exploring the Coupling of active Mechanics and Geometry in the C. elegans embryo.“ ohne unzulässige Hilfe Dritter und ohne Benutzung anderer als der angegebenen Hilfsmittel selbst angefertigt habe. Hilfe Dritter wurde nur in wissenschaftlich vertretbarem und prüfungsrechtlich zulässigem Ausmaß in Anspruch genommen. Es sind keine unzulässigen geldwerten Leistungen, weder unmittelbar noch mittelbar, im Zusammenhang mit dem Inhalt der vorliegenden Dissertation an Dritte erfolgt.

(b) die aus fremden Quellen direkt oder indirekt übernommenen Gedanken als solche kenntlich gemacht sind.

(c) ich die vorliegende Arbeit bisher weder im Inland noch im Ausland in gleicher oder ähnlicher Form einer anderen Prüfungsbehörde zum Zwecke einer Promotion oder eines anderen Prüfungsverfahrens vorgelegt habe.

6. Mir ist bekannt, dass die Nichteinhaltung dieser Erklärung oder unrichtige Angaben zum Verfahrensabbruch oder zum nachträglichen Entzug des Dokortitels führen können.

Dresden, 16.April 2019

Ort, Datum

Unterschrift Antragsteller/in